Corrosion and self-repair studies of metal alloys and alloy coatings for applications in light-weight constructions

Dissertation

zur Erlangung des Grades

„Doktor rerum naturalium“

an der Universität Paderborn

Fakultät für Naturwissenschaften

Department Chemie

von

Markus Wiesener, Geb. 23.12.1981 in Bünde

Paderborn, 2015

Tag der mündlichen Prüfung: 18. September 2015

Erster Referent: Prof. Dr.-Ing. Guido Grundmeier

Zweiter Referent: Prof. Dr.-Ing. Hans-Joachim Warnecke

Für meinen Vater, Rolf Wiesener

&

meine Oma, Edith Wiesener

Erklärung

Hiermit erkläre ich, dass ich die vorliegende Arbeit, sofern nicht anders erwähnt, selbstständig ausgeführt und verfasst,

noch nicht anderweitig für Prüfungszwecke vorgelegt

und keine anderen als die angegebenen Hilfsmittel und Quellen benutzt habe.

Bielefeld, den 04.06.2015

Content

Abstract

Within this thesis various substrates and mechanisms for light-weight construction were demonstrated. The investigated materials were analyzed for their corrosion properties and corrosion protection abilities. For this purpose, advanced combinations of different analytical methods were introduced.

It could be demonstrated that an ultrasonic treatment of the magnesium alloy AZ31 in an aqueous cerium nitrate solution increased the corrosion protection for this alloy slightly, although the generated oxide layer was furrowed by cracks. A significant advantage of the generated oxide layer was the increase of the adhesion of a model epoxy adhesive which was a model for later applications with organic coatings.

Different zinc alloys coated on 22MnB5 steel for the hot-forming process showed that, caused by the heat treatment, iron from the steel substrate diffused into the alloy coating. This led to a reduction in the evaporation of the alloy coating under thermal stress but to a slight decrease of the cathodic corrosion protection ability. Nevertheless the cathodic corrosion protection was provided for process conditions common in automotive industry. The alloying of nickel led to an enrichment of nickel on the surface decreasing the zinc dissolution and hence inhibiting the cathodic corrosion protection. Investigations on phosphated zinc alloy coated samples indicated an inhibition of the cathodic corrosion protection as well, until the phosphate layer broke down.

The combination of coulometric dissolution with downstream ICP-OES measurements gave excellent insights into the corrosion protection ability and dissolution behavior of the alloy coatings. In addition to current density – potential curves and OCP line-scans over welding points, the application of coulometric ICP-OES provided valuable information for the interpretation of corrosion and dissolution phenomena.

By combining a uniaxial stretching device with dynamic contact angle measurements it was possible to detect the self-sealing and self-healing effects of organic coatings filled with corrosion inhibitor loaded capsules. It was successfully demonstrated that, the release of

corrosion inhibitors can result in a persistent hydrophobization of a surface containing micro cracks.

Danksagung / Acknowledgment

Herrn Prof. Dr.-Ing. Guido Grundmeier danke ich für die Betreuung dieser Arbeit, welche ich von November 2010 bis Dezember 2014 an seinem Lehrstuhl für „Technische und Makromolekulare Chemie“ durchführen konnte. Die verschiedenen Projekte, in dessen Rahmen die Ergebnisse dieser Arbeit entstanden sind, waren stets interessant, herausfordernd und führten zu vielen neuen Kontakten, insbesondere auf den zahlreichen nationalen und internationalen Konferenzen, auf denen ich die Ergebnisse präsentieren durfte.

Herrn Prof. Dr.-Ing. Hans-Joachim Warnecke danke ich für die Übernahme des Zweitreferendums. Herr Warnecke war bereits zu Beginn meines Studiums im Oktober 2005, im Rahmen des Mentorenprogramms, mein Mentor und hat sich als Dekan stets für die Studierendenschaft eingesetzt. Auch hierfür meinen herzlichsten Dank.

Frau Ulrike Sakowski danke ich für die coulometrischen ICP-OES Messungen. Frau Dipl.-Chem.Ing. Nadine Buitkamp und Herrn Alexander Taube, M.Sc. danke ich für die EDX Messungen, sowie einigen der FE-SEM Bilder. Frau Charlotte Kielar, B.Sc. und Herrn Richard Grothe, B.Sc. danke ich für die Peel Tests.

Bei den Projektpartnern der DECHEMA, BMW AG und SINTEF möchte ich mich sowohl für die fachliche Unterstützung, sowie das zur Verfügung stellen der untersuchten Proben bedanken. Neben den genannten Projektpartnern danke ich allen Projektpartnern und Mitgliedern des Projektbegleitenden Ausschusses, die ich im Laufe meiner Arbeit kennen lernen durfte, für die gute Zusammenarbeit und den stets freundlichen Umgang.

Der AiF im Rahmen des IGF 358 ZN, sowie der BMW AG, München, danke ich für die finanzielle Unterstützung.

Allen aktuellen und ehemaligen Mitarbeitern des Lehrstuhls für „Technische und Makromolekulare Chemie“ danke ich für die Freundschaften, die sich im Laufe der Zeit entwickelt haben und die viele fachliche, aber auch private Unterstützung in allen Lebenslagen.

All meinen Freunden, die mich bis hierher begleitet haben, danke ich ebenso für die schönen, aber auch teilweise schweren Zeiten. Besonders hervorheben möchte ich an dieser Stelle jene, mit denen ich die letzten Jahre viel erleben durfte. Bianca, Bernd, Christoph, Esther und Roman, ich danke euch!

Vielen Dank an Bianca, Özlem und Roman für das Korrekturlesen meiner Dissertationsschrift.

Ohne die Menschen, die ich zu meiner Familie zähle, wäre ich jedoch nie so weit gekommen. Meinen Eltern Sigrid und Rolf Wiesener, meinem Bruder Thomas Wiesener, seiner Freundin Nadine Müller und meiner Oma Edith Wiesener danke ich von ganzem Herzen. Ebenso meiner neu hinzugewonnenen Familie; der meiner Freundin.

Und natürlich danke ich dir, Bianca, für deine Liebe und all die Kraft, die du mir gibst! Wir haben es beide zusammen geschafft bis hier hin zu kommen und alles erreicht, was wir uns vorgenommen haben. Sturmfest und erdverwachsen!

1. General introduction

1.1. Light-weight construction

In the age of globalization, mobility is of increasing importance. Since the fossil fuel sources are depleting and the need of reduction of environmental pollution is of highest interest the reduction of fuel consumption and therefore greenhouse gas emissions are points of intensive research [1]. At the international 1992 Earth Summit several industry countries agreed to hold the CO_2 emission at the value of 1990 until the year 2000 which forced them to reduce the CO_2 emission in the face of the increasing number of vehicles [2].

As early as in the Bronze Age engineers combined the use of lightweight construction materials, bronze, with an effective manufacturing process and a stabilizing design [1].

Weight reduction is always the central point, as all drags like resistance of roll, ascents and acceleration include the mass. Depending on the test (MNEFZ (Europe), FTP75 (USA), JP10-15 (Japan)) and adjustment of the car, the fuel consumption is reduced by 0.07 – 0.4 L/100km [1].

Reducing the mass of the body in white (BIW) can lead to reduction of the motorization and chassis whereby the fuel tank can be build smaller keeping the same cruising range [1].

The most common way to reduce mass is replacing heavy metals like steel with lightweight materials like magnesium or aluminum alloys or fiber-reinforced plastics. In so doing the economical aspect has to be taken into account, as well as the retention of the functionality like crash test properties. Higher costs for the materials or their processing as well as varying problems in recycling led to the arising of lightweight economy, where weight reduction is compared with the expenditure. Furthermore, varying tests for the comparability of the different materials with respect to mechanical properties became urgently required [1].

By use of new manufacturing processes like hot-forming, direct or indirect, new design principles are possible. New forms lead to a significant reduction of required material and therefore reduction in the mass. The challenge of changing the construction forms is on one hand the stability of crash test relevant and car body construction parts. On the other hand the

space requirement of the new forms may be in contradiction to the limited installation space [1]. One possibility to avoid the problem of needed space is the use of foam cores for primary structures, built by the use of varying manufacturing processes [2].

1.2. Magnesium

In addition to aluminum and its alloys, magnesium and its alloys received great scientific and technical interest in recent decades [3]. With a density of 1.738 g/cm^3 [3, 4] it is about 35 % lighter than aluminum which has a density of 2.699 g/cm^3 [4] and is thereby the lightest of all lightweight construction materials.

Depending on the purity, grain size, alloy composition etc. magnesium and its alloys can have valuable dampening characteristics to noise and vibrations and it has adequate heat and electrical conductivity [3]. Furthermore its specific strength surpasses the height of aluminum alloys and steels. Its castability, bending and milling at high speed and good weldability under controlled atmosphere completing the advantages of magnesium and its alloys [5].

The wide spread prevalence of magnesium in sea water, as dolomite ($CaMg(CO_3)_2$), magnesite ($MgCO_3$), olivine ($(Mg,Fe)_2[SiO_4]$), serpentine ($Mg_3(OH)_4[Si_2O_5]$), talc ($Mg_3(OH_2)[Si_4O_{10}]$), kieserite ($MgSO_4 * H_2O$), carnallite ($KMgCl_3 * 6H_2O$), bischofite ($MgCl_2 * 6H_2O$) and many more makes magnesium available in a large amounts [3, 4, 6].

The most important disadvantages of magnesium are its high reactivity and poor corrosion resistance in humid environments with a pH of less than 11 or in chloride containing environment. With its standard potential of -2.37 V (SHE) it is highly reactive and susceptible for bimetallic corrosion [3, 6–9]. As well as in automotive industry as for biomedical applications the hydrogen evolution is critical.

The corrosion reaction of magnesium is [8, 9]:

$Mg \rightarrow Mg^{2+} + 2e^-$ (anodic reaction) (Eq. 1 [9])

$2H_2O + 2e^- \rightarrow H_2 + 2OH^-$ (cathodic reaction) (Eq. 2 [9])

$Mg^{2+} + 2OH^- \rightarrow Mg(OH)_2$ (product formation) (Eq. 3 [9])

$Mg + 2H_2O \rightarrow H_2 + Mg(OH)_2$ (overall corrosion reaction) (Eq. 4 [9])

Therefore an effective corrosion protection is from utmost pertinence.

1.3. Corrosion protection of magnesium

1.3.1. Magnesium alloys

One way for a better corrosion protection was the development of ultra-pure magnesium alloys without corrosion catalysts like iron, nickel or copper. But the development of new alloys was not only of utmost interest for corrosion protection. With the alloying of aluminum the strength can be improved. A small amount of calcium improves the rollability of sheets. Lithium increases the ductility and decreases the density of magnesium alloys. Addition of manganese decreases the solubility of iron and increases the salt water resistance of MgAlZn alloys by improving the usability of such alloys for biomedical applications. Rare earth elements are alloyed to increase the high temperature strength and creep resistance. The most common alloying element is zinc in combination with aluminum to improve the tolerance for impurities. Further alloying elements like silicon, silver, thorium, yttrium and zirconium complete the alloying elements which may have a positive effect to the properties of magnesium and its alloys if they are added in the correct amount [3, 9].

1.3.2. Organic coatings

Organic coatings are economically the most efficient way to protect metals against corrosion and wear and give the ability to modify the surface properties like optical appearance, conductivity, self-cleaning effect etc. [10, 11].

The addition of active anti-corrosion pigments like zinc oxide, zinc phosphate or zinc dust increases the corrosion protection properties of organic coatings as well as passive anti-corrosion pigments like clays which increase the diffusion paths for corrosive species [10, 11].

Currently, additives which are able to passivate the surface, hydrophobize it or even close small defects in the organic coating are under research to provide a self-healing effect [10, 11].

The disadvantages of organic coatings are on one hand that more than one layer has to be coated to achieve more dense and thus protecting coatings and on the other hand the use of organic solvents is still prevailing in technical systems, which may be harmful and hazardous to the environment [10, 11].

1.3.3. Inorganic coatings

1.3.3.1. Plating

In plating, a metal is deposited on the magnesium alloy surface to protect the substrate against corrosion by isolating it from the environment. Furthermore specific properties can be adjusted like abrasion resistance, optical appearance, electrical conductivity and mechanical properties. A significant problem in the case of plating is that the deposited layer must be completely dense, uncontaminated and defect free. Otherwise, galvanic corrosion will occur, leading to the degradation of the deposited layer. The vapor deposition of ultra-pure magnesium on the magnesium alloy AZ31 accompanied by hot pressing and hot isostatic pressing, shown by Fukumoto et al. [12], increased the corrosion resistance in salt solution and the pure magnesium coating acted as sacrificial anode in the case of defect formation [3, 9, 13].

Jin et al. [14] developed a new method for the electroless plating of nickel-phosphor coatings on rare earth magnesium alloys. However, the use of Cr(VI) containing pretreatment is necessary to result in corrosion resistant, good adhering and dense layers [3, 14].

1.3.3.2. Conversion layers

The most established inorganic coatings are conversion layers. Conversion coatings are time and cost effective as the dipping process is low in energy consumption and the conversion chemicals are mostly available. Adjustment of the conversion bath enables the control of the surface properties of the end product. With the help of conversion solutions the metal surface is converted to material with a higher corrosion and wear resistance [3, 15]. For magnesium and its alloys first a hydrated oxide layer $MgO_x(OH)_y$ is built followed by anodic dissolution and a porous layer evolves. After the exchange of ions and charges, the conversion layer is formed as a semi-crystalline protective layer when the components of the pre-treatment, the conversion electrolyte and the alloy are integrated into the $MgO_x(OH)_y$ layer [3]. Depending on the conversion electrolyte, containing chromic acid, hydrofluoric acid, acetic acid / sodium nitrate, chromic acid / sodium nitrate, nitric acid or sulfuric acid, the properties and appearance of the conversion layer can be adjusted [3]. Typically the thickness of the conversion layer is about 1 to 5 µm and consists of oxides and hydroxides [3, 16]. Conversion layers consist of cylindrical cell colonies with pore diameters of about 5 nm surrounding a “mother pore” with a diameter of about 50 nm. The single colonies are combined by a barrier layer with about 5 nm thickness [3]. Immersing well cleaned, chromated magnesium parts into pure water, hexavalent chromium can be detected which is eluted from the cylindrical cell colonies. This amount of free Cr(VI) causes a so-called self-healing effect [3], which will be discussed in following sections.

The formation of a chromium conversion layer on magnesium alloys relies on the diffusion of the Cr(VI) ions through the conversion layer. This layer consists of a dense layer of $Mg(OH)_2$ and $Cr(OH)_3$ with a porous $Cr(OH)_3$ layer on top, built by the dissolution of $Mg(OH)_2$ from the dense layer. Adding copper ions to the conversion bath increases the deposition rate of the conversion layer as copper is inerter with respect to magnesium but provides a local cathode to chromium which is reduced from Cr(VI) to Cr(III) and

precipitates as $Cr(OH)_3$ faster. Although these conversion layers decrease the corrosion rate of magnesium alloys in salt spray tests, the layers are thin and a further coating is required [3, 17].

Due to the hazardous, environmentally dangerous and carcinogenic character of chromium, substitutes are of utmost research. The challenging here is the preservation of the self-healing effect, which is one of the most important advantages of the corrosion protection by chromium conversion layers. Neighboring atoms were investigated first as they form salts with a similar variation of oxidizing numbers like chromium. From the investigated elements manganese, vanadium, molybdenum and tungsten, the use of phosphate-permanganate is one of the most promising candidates. By use of a conversion bath containing $KMnO_4$ and Na_3PO_4 a homogeneous, uniform and non-powdery corrosion protection layer could be formed which is comparable in its corrosion protection ability to that of a chromate conversion layer [17]. Additionally to the corrosion protection performance phosphate-permanganate coatings provide excellent adhesion of organic coatings [17]. Using a mixture of $KMnO_4$ and HF as conversion bath led to an amorphous, thin layer containing magnesium fluorides, magnesium hydroxides and manganese oxides. Changing the hydrofluoric acid with HNO_3 a thicker conversion layer containing crystalline manganese oxide with corrosion protection properties like those of the chromate conversion layers was achieved [17]. Arnott et al. [18] first investigated $CeCl_3$ for the corrosion protection of aluminum alloys. They could show that a small amount of $CeCl_3$ of 100-1000 ppm in an aqueous NaCl solution decreases the corrosion rate significantly. By means of XPS and Auger spectroscopy it was established that cerium oxide films consisting of CeO_2, $Ce(OH)_4$ and $Ce(OH)_3$ could be generated on top of the aluminum alloy in a pH range between 4.5-8.0 which were stable for at least 10-20 days [18]. Rudd et al. [19] could show that immersing magnesium alloys into aqueous solutions of $Ce(NO)_3$, $La(NO)_3$ or $Pr(NO)_3$ decreased the corrosion rate of the magnesium alloys in a chloride free borate buffer solution at pH 8.5 for at least 10 h although the generated coatings decayed. Gray and Luan [17] reviewed that a mixture of $CeCl_3$ and H_2O_2 at pH 2.5 generated a conversion layer on aluminum alloys which increased the corrosion resistance significantly. This effect was enhanced by adding organic brighteners to the solution.

A further advantage of using rare earth compounds for corrosion protection was shown by Varanasi et al. [20]. They demonstrated for the series of rare earth metals, that ceramics, generated from rare earth oxides, with hydrophobic surfaces, with advancing contact angles between about 100° - 115°, were achieved. The polar component of the surface energy was close to 0 mJ/m^2 for every ceramic. Additionally the cerium ceramic showed a Vickers hardness twice as the stainless steel SS-316 and a similar wear resistance [20].
Nevertheless, all conversion coatings showed high porosity. Due to the porosity of those layers they have to be sealed subsequently [3]. Y. Li et al. [21] showed a feasibility using a hydrophobic decanoate conversion layer which is made by cyclic voltammetry of a sodium sulfate / sodium decanoate solution to avoid chromate coatings. An aqueous solution of 8 mmol/L sodium decanoate with 200 mmol/L sodium sulfate was used as electrolyte for the cyclic voltammetry from -1.6 V_{SCE} to -1.1 V_{SCE} with a scan rate of 10 mV/s at 40 °C. By means of SEM, EDX, XRD, FTIR and contact angle measurements the generated conversion coatings were investigated. A thick, homogeneous and dense conversion layer consisting of amorphous $(CH_3(CH_2)_8COO)_2Mg$ and crystalline $Mg(OH)_2$ with a contact angle of about 120° was achieved. This layer showed good corrosion protection abilities evidenced by potentiodynamic studies and electrochemical impedance spectroscopy.

1.3.3.3. Anodization

Another way to synthesize inorganic coatings to reduce the corrosion rate of a metallic component is to anodize the metal substrate. At an anodic potential, metal cations dissolve from the substrate, react with the electrolyte and precipitate as passivating protection layer, most commonly consisting of oxides and hydroxides, on the substrate surface. Anodizing layers can be much thicker than conversion layers. A layer thickness of more than 200 µm is possible [22]. Concerning its porosity, anodizing layers has to be sealed as well [3, 9, 22]. Furthermore the anodization technique is way more costly than conversion layers described above. More time and electrical energy are necessary to generate anodizing layers [3].
Nowadays two different mechanisms are in common use to build anodizing layers [3, 13, 22].

The classical anodic oxidation techniques use voltages of less than 100 V. In an aqueous electrolyte the magnesium substrate is the anodic electrode. A magnesium oxide layer is generated on top of the magnesium substrate. Similar to the conversion layers described above, cell colonies with diameters of about 15 nm (for the DOW-17 process) are build. In presence of alloying elements like aluminum they can be oxidized as well, leading to a spinel $MgAl_2O_4$. The DOW-17 process, established by the Dow Chemical company, uses a mixture of ammonium fluoride (NH_4HF_2), sodium dichromate ($Na_2Cr_2O_7$ x H_2O) and phosphoric acid (H_3PO_4). An alternating current of 0.5-5 A/dm^2 at a bath temperature between 70 °C and 80 °C. The most important role for the layer thickness is the time and therefore, caused by the increasing impedance, the end voltage. A treatment time of 4-5 min and an end voltage of 60-75 V leads to thin layers, as a treatment time of 25 min with an end voltage of 90-100 V leads to thick layers. The post-treatment with silicates at high temperatures seals the porous layers [3].

As an alternative to the acidic DOW-17 process the alkaline HAE process was developed by Harry A.Evangelides at Pitman-Dunn Laboratories, Frankfort Arsenal, Phil. USA. For the electrolyte, an aqueous solution containing potassium fluoride (KF), sodium phosphate (Na_3PO_4 x 12 H_2O), potassium hydroxide (KOH), aluminum hydroxide ($Al(OH)_3$) and potassium manganate (K_2MnO_4) at about 27 °C is used. At an alternating current of 1.5-2.5 A/dm^2 and a treatment time of 7-10 min with an end voltage of 65-70 V thin layers and with a treatment time of 60-90 min and an end voltage of 80-90 V thick layers can be achieved. The sealing is prepared in a solution of sodium dichromate ($Na_2Cr_2O_7$) and ammonium difluoride (NH_4HF_2) at 20-30 °C with a subsequent storage at 80 °C for 7-15 h. The resulting layer consists of spinels containing Mg, Al and Mn, mixed oxides and MgF_2. After sealing the HAE, layers are more corrosion resistant than DOW-17 layers and show the best behavior in abrasion tests [3].

Innovative plasma-electrolytic oxidation processes need voltages of several hundred of Volt. The energy released during this process locally melts the surface. Solidifying the melt leads to semi-crystalline, ceramic layers. These layers persuade with their increased corrosion and abrasion resistance in comparison to the classical anodic oxidation layers [3, 22].

Plasma-electric processes like the MAGOXID-COAT process was compared to the classical anodic oxidation processes DOW-17 and HAE showed a significant increased corrosion

resistance according to DIN50918 (current density – potential curves) and an increased abrasion resistance according to Taber-abrasion test [3, 22]. However this performance comes together with a significant increased energy demand. For the MAGOXID-COAT the surface must be activated with hydrofluoric acid (H_2F_2) before the anodic plasma-chemical treatment. The anodic plasma-chemical treatment uses a neutral, aqueous solution of hydrofluoric acid (H_2F_2), phosphoric acid (H_3PO_4), boric acid (H_3BO_3) and hexamethylene-tetramine at room temperature. The pH value of 7-7.2 is adjusted with ammonia. A direct current of 1-2 A/dm^2 and a voltage of about 400 V is used to generate either a thin layer (about 5 µm) or a thick layer (about 30 µm) with a formation rate of about 1.5 µm/min. Subsequent sealing is performed in either silicate or Sol-Gel solutions at high temperatures [3].

The major disadvantage of all anodizing processes is their poor economy. More time and energy are necessary to form the anodizing layers, which has to be sealed subsequently [3, 22].

The most important disadvantage, besides the high cost consumption, is the usage of additives, which are hazardous to environment and health. The DOW-17 process uses dichromate and ammonium hydrogen difluoride, the HAE process uses potassium fluoride and the plasma-electric processes MAGOXID-COAT and TAGNITE are using hydrofluoric acid, ammonium fluoride and potassium fluoride [3, 9, 13, 22].

H.S. Ryu et al. [23] investigated a fast, simple and environmentally uncritical sealing for plasma-electrolytic oxidation layers by aerosol deposition of titanium dioxide particles. By aerosol deposition TiO_2 particles with a diameter of approximately 2.2 µm in dried air as carrier gas, were deposited in an evacuated deposition chamber to a PEO treated magnesium alloy sample in a distance of 5 mm from a nozzle were the aerated TiO_2 particles flew through with a flow rate of 30 L/min at room-temperature. The PEO was performed in an aqueous solution containing potassium fluoride (KF) and sodium aluminate ($NaAlO_2$) as electrolyte at 15 °C for 30 min with a direct current of 5 A/cm^2. Plasma-electrolytic oxidation resulted in a macro-porous $MgAl_2O_4$ spinel surface without detection of MgO, intermetallic phases or MgF by means of XRD. Aerosol deposition of the TiO_2 particles filled the micro-pores on the surface and led to a dense TiO_2 layer increasing the corrosion resistance as shown by EIS measurements.

Y.I. Choi et al. [24] immersed a conventional anodizing layer into a di-sodium tin oxide solution to form a corrosion inhibiting tin oxide layer. The anodization was performed in a 2 M sodium hydroxide (NaOH) solution at 30 °C for 10 min with a constant voltage of 10 $V_{Ag/AgCl}$. Sealing the resulting anodization layer was performed by immersing the sample for 2-60 min in a stirred 0.4 M sodium stannate (Na_2SnO_3 x 3 H_2O) solution at 77 °C. A SnO_2 layer of about 0.4 µm thickness was achieved with a plateau for the pitting and the corrosion potential after 10 min treatment time. These layers show significantly higher pore resistance in EIS measurements for 4 h immersion to a 0.1 M NaCl solution and still higher pore resistance after 24 h immersion to a 0.1 M NaCl solution in comparison to the non-sealed anodizing layer.

El Mahallawy et al. [25] used different, environmentally friendly electrolytes for their studies of new anodizing electrolytes. After activation with hydrofluoric acid (H_2F_2) they used either an aqueous electrolyte containing sodium silicate (Na_2SiO_2) at 30-40 °C with a direct current density of 16-31 mA/cm^2 for 1.5-11 min, an aqueous solution containing sodium hydroxide (NaOH), boric acid (H_3BO_3) and sodium tetraborate ($Na_2B_4O_7$ x 10 H_2O) at 30-40 °C with a direct current density of 16-20 mA/cm^2 for 1.5-9 min or an aqueous solution containing sodium silicate (Na_2SiO_2), potassium hydroxide (KOH), sodium carbonate (Na_2CO_3) and sodium tetraborate ($Na_2B_4O_7$) at 30-40 °C with a direct current density of 16-31 mA/cm^2 for 1.5-9 min. Smooth layers consisting of MgO with small amounts of SiO_2, B_2O_3 and Mg_2SiO_4 with high corrosion resistance and adhesion to the substrates were achieved. Best results could be obtained for the third electrolyte with a layer thickness of 30 µm in comparison to the second electrolyte with a layer thickness of 30 µm and the first electrolyte with a layer thickness of 50 µm.

1.3.3.4. Self-healing inorganic coatings

Until the beginning of the 20th century self-healing, inorganic layers were realized by chromate containing treatments. Usually trigger-controlled Cr(VI) is set free from the conversion layer and is reduced to Cr(III) by the blank metal substrate. This redox reaction leads to a local increase of the pH and the Cr(III) precipitates as passivating $Cr(OH)_3$ what is designated as self-healing effect [26–28].

$$CrO_4^{2-} + 3H_2O + 3e^- \rightarrow Cr(OH)_3 + 5OH^- \qquad \text{(Eq. 5 [29])}$$

Although in the 1950's many studies were published showing the correlation of chromates with varying types of cancer [30–32] chromates were used as corrosion protecting layer for decades. The disadvantage of chromium containing conversion layers is the use of hexavalent chromium which is extremely harmful and causes cancer [28]. Since the year 2000 the EU decided to forbid the use of hexavalent chromium for new vehicles.

Nowadays two mechanisms are in main focus of research. One is the solid-state self-healing and the other is a self-healing supported by fluids [33].

1.3.3.4.1. Solid-state self-healing

Although the diffusion of atoms in a solid is hindered, grain boundaries, free surfaces and imperfections may deal as diffusion paths [33].

The precipitation of dissolved metal atoms in micro cracks is the mechanism for the solid-state self-healing. Similar to the hot-forming or hardening, the metal is heated up and quickly cooled down. The result is a oversaturated microstructure, where the dissolved metal atoms are able to diffuse at an elevated temperature via the mentioned pathways to precipitate in imperfections, triple points and defects, used as crystal nucleus [33].

Van der Zwaag et al. [34, 35] reviewed that Lumley et al. investigated the self-healing effect of underaged aluminum alloys. This effect could be adjusted by solution treatment of age-hardenable aluminum alloys at high temperatures, followed by quenching and a short time annealing step at elevated temperature. The resulting underaged microstructure contained an amount of solved atoms in the solid phase, which could diffuse to the nanocracks by a further annealing step or by deformation at elevated temperature. For Al-Cu-Mg-Ag alloys, the movement of disordered atoms, promoted the nucleation for a rapid precipitation in the defects, which illustrated the strong self-healing effect of this alloy.

1.3.3.4.2. Fluid supported self-healing

In the case of organic coatings, the self-healing mechanism is under development, using inhibitor filled containers, which enable a trigger-controlled release of inhibitors, reactive monomers, ionomers etc. when a defect occurs. This mechanism is possible for metals when metal particles with lower melting temperature are incorporated into the metal substrate, plates or alloys. Treatment at an elevated temperature leads to melting of the particles which may close the defect. Since the particles remain in the metal part, this self-healing mechanism is feasible for the life time of the metal part. The disadvantage of this mechanism in a solid is the need of capillary forces to provide the fluid phase. For larger defects these capillary forces are not high enough for a complete self-healing. Using more or larger particles may decrease the mechanical properties of the work piece [33].

An approach for larger defects is the additional incorporation of shape memory alloy fibers. In the case of a defect the elevated temperature leads to reversion of the fibers which minimizes the defects in that way that the capillary forces are high enough that the fluid particles can close the micro cracks [33].

Other approaches for the self-healing in solids were investigated by Laha, Kyono and Shinya [36, 37] for stainless steels. By alloying boron, cerium and/or titanium and/or copper to type 347 or 304 stainless steel Ce_2O_2S or $Ti_4C_2S_2$ was formed, reducing the sulfur content and therefore the sulfur precipitation in the steel which enabled the formation of boron nitride (BN). Boron nitride and/or copper precipitated in cracks formed by creep, closed the defects and thus showed a self-healing effect in case of creep rupture.

For Ti_3AlC_2 ceramics Song et al. [38] could show that cracks, created by tensile stress, with a diameter of less than 1 µm could be completely healed by heat treatment at 1100 °C for 2 h in air. Caused by the high temperature in presence of oxygen, α-Al_2O_3 and a small amount of TiO_2 were built by oxidation of the ceramics compounds.

Other compounds which are forming oxidation products at high temperatures in an oxidative environment and are used for gas turbine engines, heating equipment, automotive converters etc. are Al_2O_3, SiO_2 or Cr_2O_3 [39] as well as SiC or Si_3N_4 which form SiO_2 [34].

1.3.3.5. Ultrasonic treatment

Möhwald et al. [40–47] investigated the application of ultrasonic treatment on metals to form sponge-like, porous metal oxide films on the bulk material.

By use of directed ultrasonic shockwaves cavitation vesicles arise. When burst locally more than 5000 K and a pressure of several hundreds of bar occur. Under these conditions the surface deforms and a rough, porous and sponge-like metal layer, associated with the bulk phase is build. In the surrounding, aqueous medium oxygen radicals are generated, leading to an oxidation of the metal layer. This layer increases the corrosion protection properties further [42].

The porous structure gives the possibility of loading the layer with corrosion inhibitors, antibiotics, antiseptics etc. subsequently by immersion. Furthermore, the loading of the oxide layer is already possible during the ultrasonic treatment process by using an aqueous solution of the corrosion inhibitors for the ultrasonication [40–42, 44–46]. Additionally the enlarged surface increases the adhesion of conventional corrosion protection layers by mechanical interlock, physical and chemical bondings [46].

Varying the ultrasonic parameters like time, power, distance between the substrate and the sonotrode as well as the variation of different additives to the aqueous solution lead to adjustable layers with respect to thickness, porosity and composition [42].

Möhwald et al. could show for aluminum that layer thicknesses up to 200 nm are possible. Within 60 minutes surfaces of 80 m^2/g were generated. After 10 minutes pores could be detected, which had a diameter of about 4 nm after 60 minutes. Ultrasonic treatment of more than 60 minutes led to a degradation of the layer. For magnesium a similar behavior could be identified but the buildup of the layer was much faster due to the lower melting temperature of magnesium [42].

Birer et al. [48] reported a precipitation of SiO_2 particles on a titanium surface with a layer thickness of more than 200 nm.

For the aluminum alloy AA2024 Möhwald et al. [40] verified via ATR-FTIR, XPS, XRD, FE-SEM and SVET the mounting of cerium oxide, the generating of a Ce/Al-oxide-network

and an accompanied, significant increase of the corrosion protection properties in chloride containing electrolytes.

1.4. Hot-forming

As mentioned before (in chapter 1.1) another way reducing the weight of an automobile is the investigation of new manufacturing processes for structural components [1, 2].

A common manufacturing process is the hot-forming process. Typically the steel 22MnB5 is heated, formed and fast but controlled cooled down leading to a transformation to a martensitic microstructure which increases the tensile strength up to 1500 MPa [49–56].

Furthermore the spring-back phenomenon which occurs for cold-formed steel parts, is reduced significantly [49–56].

To reduce oxide scales and decarburization, an Al-Si coating is commonly used. This layer leads to a barrier effect, however is incapable of a proper cathodic corrosion protection. To achieve cathodic corrosion protection, Zn alloy based coatings are under investigation [50, 51, 54, 56]. Nowadays two different mechanisms for the hot-forming process are appropriated.

1.4.1. Indirect hot-forming process

In the case of the indirect hot-forming process, the zinc alloy coated steel parts are cold formed and cut, before heated and rapidly quenched under high pressure. In Figure 1 the mechanism of the indirect hot-forming process is schematically shown.

Figure 1: schematic illustration of the indirect hot-forming process [49]

One disadvantage of this process is an unavoidable and undesired process step which decreases the productivity. A second disadvantage is that the steel parts used for the indirect hot-forming process must not be coated, since due to the cold forming the coating would break, leading to a decrease in corrosion protection at the oxidizing oven atmosphere. Nevertheless, the process still is wide spread because some parts can only be produced by means of the indirect hot-forming process. The reason is that the cooling during the quenching is so rapid that in the case of the direct hot-forming process, which is described in the next section, cracks in the steel parts would occur during the forming [49].

1.4.2. Direct hot-forming process

The direct hot-forming process combines hot stamping with quenching after the zinc alloy coated steel parts were heated as shown in Figure 2.

Figure 2: schematic illustration of the direct hot-forming process [49]

After hot stamping and quenching, which occurs rapidly caused by the cold stamping tool, the steel parts are cut. The advantage of this process is the merging of two process steps which makes the direct hot-forming more economic than the indirect hot-forming process [49].

In addition to the disadvantage that the cooling during the quenching step occurs so rapid that caused by the stamping process step cracks might arise [49], another disadvantage of the direct hot-forming process is liquid metal induced embrittlement (LMIE) which is described below [55, 57].

1.5.Liquid metal induced embrittlement

When hot dipped galvanized steel is heated during the hot-forming process the Fe-Zn intermetallic interface is converted into a liquid Zn-rich phase due to the lower melting temperature of the zinc. Caused by the wetting of the matrix grain boundaries by the liquefied zinc embrittlement occurs. The grain boundaries diverge. In combination with tensile stress large cracks in the surface arise. The liquefied zinc diffuses into the fissures into the austenite grain boundaries in the subsurface region. The interconnection of the high-temperature austenite grain boundaries in decreased and proliferation of the cracks into the bulk phase takes place [55].

The incidence of LMIE is prejudiced by several factors. The fracture propagation rate is influenced by the inflicted stress and the composition of the liquid and solid metal. Caused by the deformation during the hot-forming, the stress increases. The fissure of the solid metal leads to a decrease of the stress. The chemical compositions of the liquefied metal and the solid metal influences LMIE as the surface energy of the liquid metal influences the wetting and the alloying of the solid metal might increase the LMIE by increasing the crack formation possibility. As the grain boundaries are the initial spots for LMIE, the microstructure of the solid metal is a further factor. Finally the surface energy difference between the liquid and the solid metal as well as the surface energy of the grain boundaries influences the wettability [57].

Varying solutions for the problem of LMIE are under investigation. According the hot-forming process conditions, temperature controls the LMIE kinetics. The deformation rate and the composition of the liquefied and the solid metal influence the stress and therefore the speed of fracture formation and propagation [57].

Galvanizing the steel parts with an Al/Si alloy hinders not only the decarburization and oxide scales but reduces LMIE, since the formed Fe/Al alloys, caused by high temperatures, show high melting points [55].

To increase the cathodic corrosion protection properties while avoiding LMIE Zn and Zn-alloy coatings are under utmost investigation. The alloying of nickel to the zinc coating reduces the evaporation and increases the melting temperature of the alloy coating. If iron

was alloyed to the zinc coating and the temperature during hot-forming was below the melting temperature of the Zn/Fe alloy, LMIE is inhibited as no liquid phase is build. Decreasing the temperature below the melting temperature of the intermetallic phase would avoid LMIE as well, but the transformation to martensitic steel and hence the strength of the structural component would decrease too [55].

Nonetheless, the high temperatures both in the direct and the indirect hot-forming process lead to an increased mobility of the metal atoms in the intermetallic phase. An alloying of iron into the Zn, Zn-alloy or Al/Si-alloy coatings takes place [54].

1.6.Analytical methods for self-healing studies

As mentioned before (in chapter 1.3.2) self-healing of organic coatings used for corrosion protection on metal substrates is under utmost research. The aim is to prolong the life-time of an organic coating as long as the life-time of the protected building component, which is covered by the coating [58].

The process of self-healing can be classified by intrinsic or extrinsic self-healing depending on whether polymer coating heals itself or encapsuled healing agents are set free to heal the cracks, respectively [59].

Intrinsic self-healing can be categorized in two different phenomena [59].

Crack healing by physical interactions is determined by surface rearrangement, surface approach, wetting, diffusion and randomization [59–62]. To induce intrinsic self-healing by physical interaction the polymer is heated up to or slightly above the glass transition temperature. Jud and Kausch [63, 64] could show for poly(methyl methacrylate) (PMMA) and poly(methyl methacrylate-co-methyl ethylacrylate) (MMA-co-MEA) with different molecular weights and degrees of polymerization, that a heat treatment of above the glass transition temperature, under slight pressure, led to full restoration of the fracture toughness by interdiffusion and entanglement of the polymer chains. Jud et al. [64] found that the restoration of the fracture toughness at thermal treatment above the glass transition temperature is time dependent with $t^{1/4}$.

Since the crack healing occurs only at temperatures at or above the glass transition temperature, the dropping of the glass transition temperature would be interesting. Lin et al. [65] and Wang et al. [66] showed for PMMA that the treatment with methanol or ethanol decreased the glass transition temperature to a range between 40-60 °C. Furthermore they found that the quality of the self-healing depended on the wetting and the increase of the diffusion.

For copolymers of poly(ethylene-co-methacrylic acid) (EMAA) Kalista et al. [67] could show thermomechanical healing. In a temperature range of the environment from -30 °C to 25 °C they observed healing by use of high energy mechanical impacts like ballistic puncture or sawing. The polymer was heated to its viscoelastic melt by storing the impact energy and resealed the defects. This effect requires high energy impacts. For low-speed fractures the energy was not high enough and thermomechanical healing was not active.

Additionally intrinsic self-healing can be induced by chemical interactions [59]. Takeda et al. [68] investigated the self-healing properties of polycarbonate (PC) by use of sodium carbonate (Na_2CO_3). First the polymer was treated in a steam chamber at 120 °C to model the deterioration. To investigate the self-healing effect the polymer was then dried and treated at 130 °C in nitrogen atmosphere under reduced pressure. They supposed the healing mechanism in the way that the first step was a hydrolysis of the carbonate bond of a polymer chain, leading to a high concentration of phenoxy groups. Subsequently a substitution of a proton with a sodium ion occurred. The sodium phenoxide group attacked the carbonate bond of another polymer chain which led to a recombination of the two chains and an elimination of a sodium phenoxide.

The addition of a copper/amine complex as catalyst to poly(phenylene ether) (PPE) was investigated by Imaizumi et al. [69]. Radicals, built by the deterioration of the polymer chain, were stabilized by a proton donor. Initiated by the copper/amine complex the chains combined by eliminating the two protons, whereas copper was reduced from Cu(II) to Cu(I). By diffusion of oxygen, copper was oxidized from Cu(I) to Cu(II) and the resulting oxygen ion reacted with the protons and left the system as water.

To avoid the addition of further catalysts, monomers or surface treatments, Wudl et al. [70] investigated the use of Diels-Alder reactions to synthesize a highly cross-linked polymeric material consisting of multi-furan and multi-maleimide. A retro-Diels-Alder reaction occurred at temperatures above 120 °C and the cross-linked bonds were destroyed. Cooling down the system led to a Diels-Alder reaction again and the cross-linking was fully reversible.

Continued development was done by Liu and Hsieh [71]. Using epoxy compounds as precursors for the multi-furan and multi-maleimide compounds they combined the healing ability with the resistance of epoxy resins.

Additionally Liu and Chen [72] prepared cross-linked polyamides by combining maleimide containing polyamides via Michael addition with furfuryl amine. The resulting furan containing polyamides were mixed with maleimide containing polyamides to build the cross-linked film via Diels-Alder reaction which had the healing properties described above.

For extrinsic self-healing one of the most common used concepts is the incorporation of microcapsules or nanocontainers, filled with healing agents, into the organic coatings [59, 73]. During the last years varying capsules (e.g. PU capsules), containers (e.g. LDH) and ion-exchange extenders (e.g. LDH, halloysites, zeolites) were investigated and filled with varying anticorrosive (e.g. MBT, 8-HQ) or water-repellent additives (e.g. phosphonic acids, carboxylic acids, alkoxysilanes) or monomers which are able to form a passive polymer layer (e.g. alkoxysilanes, acrylates) by polymerization, polycondensation or polyaddition [4, 58, 74–77].

An important challenge is the release of the additives from the containers at the right time. A continuous release or the direct incorporation of the additives into the organic coating would lead to a continuous reduction of the additives and failure of the anticorrosive effect in the moment of crack formation. If the release was time-delayed after the crack formation occurred, corrosion would take place irreversibly. Therefore the release of the inhibitors from the capsules must be triggered e.g. by change of the pH-value of the environment, mechanical impact etc. [58].

Huang and Yang [78] for example described the encapsulation of hexamethylene diisocyanate (HDI) into polyurethane capsules by an interfacial polymerization reaction. In an aqueous solution of gum arabic as surfactant a mixture of methylene diphenyl diisocyanate (MDI) and hexamethylene diisocyanate was added. After heating an *1,4*-butanediol solution was added dropwisely into the oil-in-water emulsion. The resulting capsules were with diameters of 5 µm to 350 µm andshell thicknesses of 1 µm to 15 µm.

Garcia et al. [79] presented an anticorrosive organic coating with self-healing effect based on water reactive silyl ester. They synthesized octyldimethylsilyloleate and encapsulated this silyl ester by an in-situ poly(urea-formaldehyde) micro-encapsulation described by Brown et al. [80]. The silyl ester hydrolyses in present of moisture into the two components, the silanol and the oleic acid, both forming a hydrophobic layer on the metal substrate. Via crosslinking of the silanols, the layer becomes denser protecting the metal substrate against the aggressive environment.

Using a mixture of different alkoxysilanes with varying hydrocarbon tails encapsulated in polyurethane capsules leads to hydrophobic and dense barrier films by the crosslinking of the siloxane bonds with adjustable properties, depending on the alkyl chain. The release of the alkoxysilanes from the PU capsules is triggered by mechanical impact which leads to an immediate hydrophobization of the defected organic coating [81].

The longer the alkyl chain is, the more hydrophobic is the resulting layer and hence the anticorrosion property [82]. In contrast to this advantage long alkyl chains may cause a phase separation as the solubility of long alkyl chains in the reaction media is decreased [81].

Latnikova et al. [81] could show that a mixture of a long chain alkoxysilane (trimethoxy(octadecyl)silane (MTODS)) and an alkoxysilane with a shorter hydrocarbon chain (trimethoxy(octyl)silane (MTOS)) leads to both, the hydrophobization by MTODS and an adequate solubility of the mixture with the aqueous environment by MTOS. After the release, the alkoxysilanes hydrolyse when they come in contact with the surrounding aqueous environment:

$$R - Si(OMe)_3 + 3H_2O \rightarrow R - Si(OH)_3 + 3MeOH \qquad \text{(Eq. 6 [81])}$$

With respect to the environmental pH value and temperature, the concentration of the silanes, the presence of water and the configuration of the functional groups the hydrolysed silanol groups polycondensate and crosslink, forming a dense barrier layer with low film thickness which closes the defect and protects the substrate against the aggressive environmental electrolyte [81, 83–86].

Other monomers or oligomers encapsulated were investigated by using styrene monomers, epoxy monomers or dicyclopentadiene (DCPD). In presence of a hardener in the polymer matrix, like an amine or a 2-methylimidazole/CuBr2 complex ($CuBr_2(2\text{-}MeIm)_4$), the epoxy monomers, when set free, cure at elevated temperatures of about 130-180 °C [59].
An approach for the extrinsic self-healing at room temperature was investigated by White et al. [87]. Microencapsulated DCPD was polymerized via ring opening metathesis polymerization in presence of a Grubbs catalyst in the polymer matrix. In later works it was evidenced that the self-healing effect was only effective, when the crack was completely filled with the healing agent and therefore the particle size is an important factor [88, 89]. By use of ultrasonic techniques very small capsules of about 220 nm in diameter were available [89].
Instead of capsules the use of hollow glass tubes or fibers was investigated by Dry et al. [90] and Bleay et al. [91]. One system was single-part adhesive where the fibers were filled with one kind of resin. Another system used was two-part adhesive when the healing agent and the hardener are placed in two neighboring fibers. The last described system was a two-part adhesive where the fibers were filled with one component and the other component was encapsulated in capsules. By mechanical impact the fibers broke and the healing agent came into contact with the hardener, closing the defects.
A disadvantage of using capsules or hollow glass fibers is that they ensure the self-healing effect only once. More effective would be a network like the blood circuit in human bodies. To realize this three-dimensional microvascular networks were examined by Toohey et al. [92]. They printed a three-dimensional microvascular network with volatile ink consisting of Vaseline/microcrystalline wax (60/40 by weight) like described by Therriault et al. [93]. The network was filled with epoxy resin which was hardened before the ink was removed and the resulting epoxy network was filled with healing agent. As healing agent DCPD was used. This reacted in a ring opening metathesis polymerization with Grubbs catalyst, present in the

matrix, after a crack of the network occurred. The optimal network configuration was investigated by Bejan et al. [94] showing that the time to fill the cracks is only half by using the same diameter size for all channels in the network grid.

2. Fundamentals of analytical methods

2.1. Field-emission scanning electron microscopy (FE-SEM)

As early as 1927 a German patent was submitted by Stintzing for the investigation of particles too small for optical microscopy. But with the investigation of an electron beam scanner which was able to detect the secondary electrons (SE) by Knoll in 1935 it was first time possible to generate a magnified image [95]. Further pioneers in the development of SEM were von Ardenne in 1938 and Zworykin in 1942 [95–97]. A great amount of research was devoted until todays scanning electron microscopes are in the position to create varying images, like SE images, BSE images or topography images, show an excellent spatial resolution, a user-friendly handling as well as high throughput of samples caused by faster scanning rates, easier sample preparation needed and automation [95–97]. Figure 3 shows a schematic of a FE-SEM.

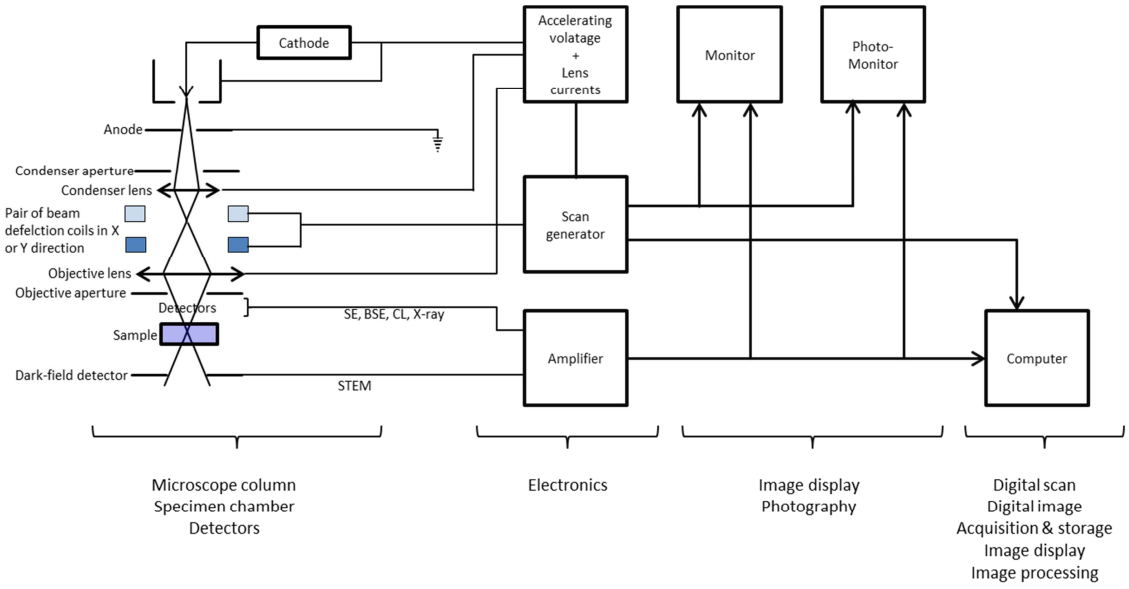

Figure 3: schematic build-up of a FE-SEM, with SE: secondary electrons, BSE: backscattered electrons, CL: cathodoluminescence, X-ray: X-ray signal, STEM: scanning transmission electron microscope signal [95]

The emission of electrons used for SEM is induced by either a tungsten filament, a LaB_6 or Schottky emitter or a tungsten field-emission tip. Condenser lenses and finally the objective

lens, in combination with a field-emission gun, form an incident electron beam with a diameter of 0.5-1 nm for the excellent spatial resolution [95, 97].

SEM images can be detected by two different types of electrons. After the primary electrons enter the bulk phase of the sample elastically (electrostatic interaction with the nuclei of the bulk atoms) and inelastically (interaction with the electrons of the bulk atoms) scattering is induced. Most of the electrons penetrate deeper into the bulk, but some, the backscattered electrons (BSE), are elastically backscattered, still having a high kinetic energy. The kinetic energy of inelastically scattered electrons can decrease that much that they are absorbed by the bulk. The penetration depth and interaction volume describe the depth and the volume at which most of the electrons are absorbed to the bulk. As the beam spreads horizontally caused by the scattering, the interaction volume has a pear-like cross-cut shape. Because the kinetic energy of the BSE must be high enough to leave the bulk phase, the information, gathered by a BSE image, comes from about half the penetration depth, which means several magnitudes of nanometer. By detecting BSE the material contrast of a sample as well as the different crystal orientation of a polycrystalline sample can be evaluated [97].

If the primary electrons were inelastically scattered by interaction with the bulk atom electrons, their kinetic energy is transferred to the bulk atom electrons. For valence electrons and if the energy is high enough, it is possible that a part of the transferred energy is used as work function and the rest as kinetic energy for the removed electron. These secondary electrons (SE) might be scattered as well, so that their kinetic energy decreases. The large difference of the kinetic energy of SE and BSE makes it possible to discriminate them. Only few SE from the very near surface region are transmitted to the vacuum and can be detected. Therefore the gathered information by a SE image comes from about 2 nm depth, giving a good topography contrast which enables the possibility of three-dimensional topography images of the investigated samples surface [97].

The appearance of a topography image depends on the arrangement of the detector. Whereas side-mounted detectors give a more contrasted 3D image due to the fact that areas which are facing the detector have a higher feasibility that the electrons are gathered by the detector, for in-lens detectors the amount of gathered electrons is higher [97].

A significant problem at the investigation of semi-conductive or non-conductive samples, discovered first by Knoll 1941 during the SEM investigation of a piece of mica, is the charging effect. Since the SE have a very low kinetic energy of about 5-50 eV the collection of the secondary electrons by the SE signal detector may be disturbed by local charging of the sample. To avoid charging the energy of the primary beam can be decreased at the expense of magnification. Another solution is the sputtering of the samples with metals like gold, palladium, silver, platinum or aluminum or with carbon. Typical layer thicknesses are 10-20 nm. Therefore the information gathered by SE imaging no longer come from the sample itself but the precipitated coating layer [97, 98].

2.2. Energy dispersive X-ray spectroscopy (EDX)

When electrons of the primary beam are inelastically scattered by an inner-shell electron of the bulk phase atoms the possibility is given this electron is emitted leaving a hole in the inner shell. This hole is filled within about 10^{-15} s by an electron from an outer shell leading to the emission of an x-ray photon with characteristic energy for the bulk phase atom. The atomic numbers of the bulk phase atoms and the voltage and current of the primary beam define the size of the pear-like interaction volume of which the samples information are detected from. According to the principle of EDX it becomes clear that elements with an atomic number less than 10 are hard to detect [97, 98].

Combining EDX with SEM gives the possibility of creating a map which shows the distribution of the samples elements. Therefore the energy dispersive spectrometer detects a number of different x-ray photons while the primary beam scans the surface. Overlaying the EDX map with the SEM image indicates both the topography with the element distribution [97, 98].

2.3. Raman spectroscopy

In 1928 Sir C.V. Raman described a light-scattering effect first induced by sunlight and complementary filters, later with a mercury vapor lamp with a Hilger quartz spectrograph afterwards named after him. Especially in India but as well elsewhere a lot of developments and investigations using and enhancing Raman spectroscopy followed [99].

The Raman effect is based on the inelastic light scattering at molecules which show the ability that a dipole moment can be induced. This dipole moment is induced when the molecule interacts with the electric field of the incident light and electrons and nuclei of the molecule are forced into opposite directions. Proportional to the electric field strength and the polarizability α of the molecule is the strength of the dipole moment. Although the Raman effect is based on the inelastic light scattering, elastic light scattering and inelastic radiation of the sample can be detected. The elastic light scattering leads to Rayleigh lines which have the same frequency than the incident light. The inelastic light scattering results in either Stokes or Anti-Stokes lines. Caused by the inelastic light scattering the molecules are excited to a virtual stage. If the incident light transfers energy to the molecule, resulting in molecule characteristic vibrational and rotational states of the molecule, a Stokes shift to lower wavelengths of the scattered light with respect to the incident light is induced. If the molecule was in excited state before the interaction with the incident light, energy can be transferred from the molecule to the scattered light, resulting in a characteristic Anti-Stokes shift to higher wavelengths of the scattered light with respect to the incident light. Because of the low probability of elastic light scattering which happens to about 10^{-4} parts of the incident light, the Raman effect is very weak. The inelastic light scattering is with about 10^{-9} parts even weaker. But as the most of the molecules are in ground state, the Stokes lines are more intensive than the Anti-Stokes lines and are typically used for Raman spectroscopy [100, 101].

A schematic illustration of the Raman effect is shown in Figure 4.

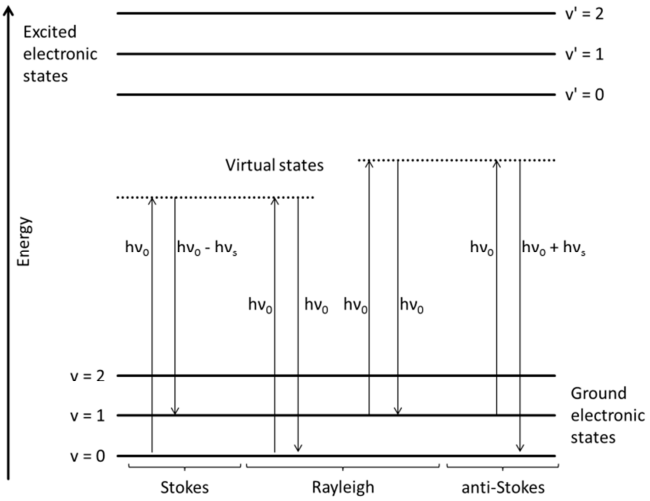

Figure 4: schematic illustration of the Raman effect with indicated Rayleigh, Stokes and anti-Stokes lines [100]

Although a sharp focused laser beam is used for Raman spectroscopy, undesirably scattered light from samples spots which are not in focus of the investigation decrease the resolution.

The use of a confocal microscope, like shown in Figure 5, leads to a significant increase of the spatial resolution.

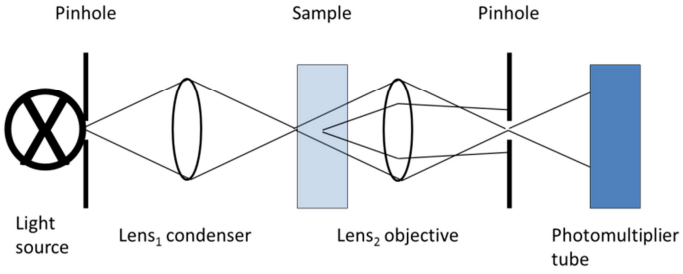

Figure 5: schematic set-up of a confocal microscope [95]

After the light source a pinhole restricts the beam before it is focused via the condenser lens on the sample. Behind the sample a detector lens converges the desired scattered light to a second pinhole and the undesirably scattered light is not detected by the detector as it can be seen in [95].

2.4. Electrochemistry

Electrochemistry is characterized by the conversion of material by shifts of electronic charges which are adjustable by an external electrical stimulus. These oxidation-reduction reactions which can be controlled by the appliance of a current or a voltage include anodization processes or electrophoresis as well as corrosive dissolution, electrolysis etc.

Although Swammerdam observed in the middle of the 17th century an excitation of muscles which were in contact to different metals he could not relate it to electricity. Hence the results published by Galvani in 1791 were the basic for the field of electrochemistry. During the next decades a lot of investigations followed by Volta, Sultzer, Nicholson, Carlisle, Becquerel, Faraday, Kohlrausch, Arrhenius, Nernst, Tafel and many others.

Thermodynamically a potential difference at the interface between the sample and the electrolyte, the so called Galvani potential is build.

$$\Delta\varphi = \varphi^{I} - \varphi^{II} \qquad \text{(Eq. 7 [102, 103])}$$

with: $\Delta\varphi$: potential difference, φ^{I},φ^{II}: potential of phase I and phase II

At the electrochemical equilibrium the electrochemical potentials of a component are equal in both phases.

$$\widetilde{\mu_i^{I}} = \widetilde{\mu_i^{II}} \qquad \text{(Eq. 8 [102, 103])}$$

with: μ: electrochemical potential of component i in phase I and phase II

Since the electrochemical potential for the component i is indicated by its free enthalpy and its electrostatic energy the following applies:

$$\tilde{\mu}_i = \mu_i + z_i F \varphi_i = \mu_i^0 + RT ln a_i + z_i F \varphi_i \qquad \text{(Eq. 9 [102, 103])}$$

with: $\tilde{\mu}_i$: electrochemical potential of the component i, μ_i: chemical potential of the component i, z_i: valence of the component i, F: Faraday constant, φ_i: Galvani potential of the component i, μ_i^0: chemical standard potential of the component i, R: universal gas constant, T: absolute temperature, a_i: activity of the component i

Insertion of Eq. 9 in Eq. 7 results in:

$$\Delta\varphi = \frac{\mu_i^{0\,II} - \mu_i^{0\,I}}{z_i F} + \frac{RT}{z_i F} ln \frac{a_i^{II}}{a_i^{I}} \qquad \text{(Eq. 10 [102, 103])}$$

with: $\Delta\varphi$: potential difference, μ_i^0: chemical standard potential of the component i in phase I or phase II, z_i: valence of the component i, F: Faraday constant, R: universal gas constant, T: absolute temperature, a_i: activity of the component i in phase I or phase II

Since the first term of Eq. 10 is independent of the concentration it is known as the standard potential. Inserting for the activities of component i the oxidized and reduced species the Nernst equation follows for the equilibrium of free enthalpy and electrostatic energy, which means that a reversible reaction, determined by the diffusion of the molecules at the electrode, takes place:

$$E_h = E_i^0 + \frac{RT}{z_i F} ln \frac{a_i^{ox}}{a_i^{red}} \qquad \text{(Eq. 11 [102, 103])}$$

with: E_h: half-cell potential, E_i^0: standard potential of component i, z_i: valence of the component i, F: Faraday constant, R: universal gas constant, T: absolute temperature, a_i^{ox}/a_i^{red}: activity of oxidized/reduced species

From Nernst equation it becomes clear that an absolute potential does not exist as the potential is always summed up to a standard potential. This standard potential is the electric potential difference between component i and a reference electrode as all measured potentials in any experiment are. Per definition the standard hydrogen electrode (SHE) is the common redox couple used in data tables in thermodynamics and electrochemistry. Since the SHE is a theoretical electrode with ideal standard state, the normal hydrogen electrode with a platinum electrode flushed by a hydrogen steam with 1 bar in an aqueous HCl solution with the concentration 1 mol/L is not exactly equal to the SHE but differs at about 6 mV. Nevertheless the NHE is typically used in experiments to figure out the standard potential for half-cell reactions. As the NHE is impractical caused by its set-up, other reference electrodes, which were referred to the NHE and thus to the SHE, are commonly in use. The most widespread reference electrodes are the silver/silver chloride and the calomel electrode [103].

A silver chloride coated silver wire in a potassium chloride typically with the concentration of 3 mol/L leads to a potential of:

$$E_{AgCl/Ag}\left(KCl, 3\,\frac{mol}{L}\right) = +0.21V_{SHE} \qquad \text{(Eq. 12 [103])}$$

The calomel electrode uses mercury in mercury dichloride in a typically saturated solution of potassium chloride. This saturated calomel electrode (SCE) leads to a potential of:

$$E_{Hg_2Cl_2}(SCE) = +0.24V_{SHE} \qquad \text{(Eq. 13 [103])}$$

In the two-electrode set-up which is defined by the two half-cell reactions on the counter electrode and the working electrode only the overall voltage between the two electrodes is detected. A defined application of a potential or a current on one of the electrodes is not controllable. This problem can be solved by using a three-electrode arrangement. Additionally to the counter and the working electrodes a reference electrode is implemented. The potential between the working electrode and the reference electrode can be detected and, if necessary, adjusted and hence the current flow between the working electrode and the

counter electrode. Requirement of the reference electrode is that no current flows through it and it must be inert so that the standard potential of the reference electrode does not shift during the measurement.

To reduce the electrolyte resistance the reference electrode should be as near as possible facing the working electrode. In Figure 6 a simple schematic of a three-electrode arrangement is shown [103].

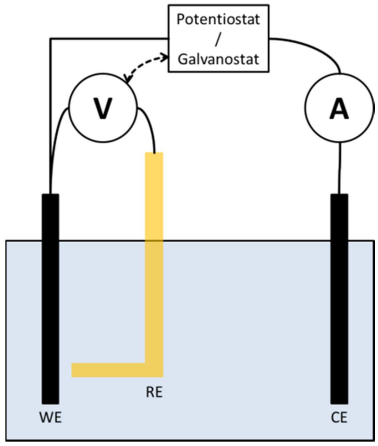

Figure 6: three-electrode set-up with Hager-Luggin capillary as reference electrode [102, 103]

The advantage of the used Hager-Luggin capillary is that it can be located very close to the surface of the working electrode, which significantly reduces the electrolyte resistance.

2.4.1. Open circuit potential (OCP)

At the open circuit potential the anodic (oxidation) and cathodic (reduction) reactions are with the same speed. Therefore on the macroscopic scale no current flow can be observed [103].

Observing only one electrode of the system, no current flow means that the activities of oxidized and reduced species are equal, which leads to the standard potential, according to Nernst equation [103].

In case of corrosion, for example, no detected current flow may be caused by the equal speed of the iron oxidation on one side and the oxygen reduction on the other side. For this redox couple as well as for redox couples with different metals or non-metals the potential is called mixed potential as its value is between the standard potentials of each electrode material [103].

A third possibility why no current flow can be detected in macroscopic view is that the redox reactions are way slower than the measurement time. The OCP shifts as the interface is not in equilibrium. But this shift is so slow that it cannot be detected during the time of the experiment [103].

2.4.2. Potentiodynamic studies

For the measurement of current density – potential curves the current flow between the working electrode and the counter electrode is detected as a function of the varying potential between the working electrode and the reference electrode. This variation must be applied very slowly with typically 2 mV/s or less, so that quasi-steady-state conditions can be assumed. The left side of the potential axes (x-axes) indicates the cathodic reaction (reduction) and the right side the anodic (oxidation). The turning point where the current is I=0, indicate that oxidation and reduction take place equally which is at the OCP. With increasing overpotential to the anodic side metal dissolution takes place faster [103].

The kinetics which can be measured by current density – potential curves consist of two mechanisms. One mechanism is the mass transport kinetic which plays role in electrolytes where one species of the redox couple is not present. Although some ions will stay in the diffusion layer most will diffuse into the bulk phase of the electrolyte therefore no longer be available for the redox reaction. In this case the cathodic branch and the anodic branch of the current density – potential curve must be considered for its own. A limiting current indicated by a turning point on one branch is given by the concentration of the present species. The build species, not present in the electrolyte, will diffuse into the electrolytes bulk. The potential at which this limiting current is detected is called the half-wave potential and is close to the standard potential of the couple [103].

The other mechanism is the redox reaction kinetics. For fast redox reaction kinetics the current changes very fast around the OCP. For slow redox reaction kinetics the cathodic half-wave potential is shifted to a more negative value and the anodic half-wave potential to a more positive value than the standard potential. This difference increases the slower the kinetics is [103].

For analysis of kinetic parameters, the Tafel plot, shown in Figure 7 for a dummy cell (Gamry Instruments) with indicated tangents at the enlargement, is a common tool.

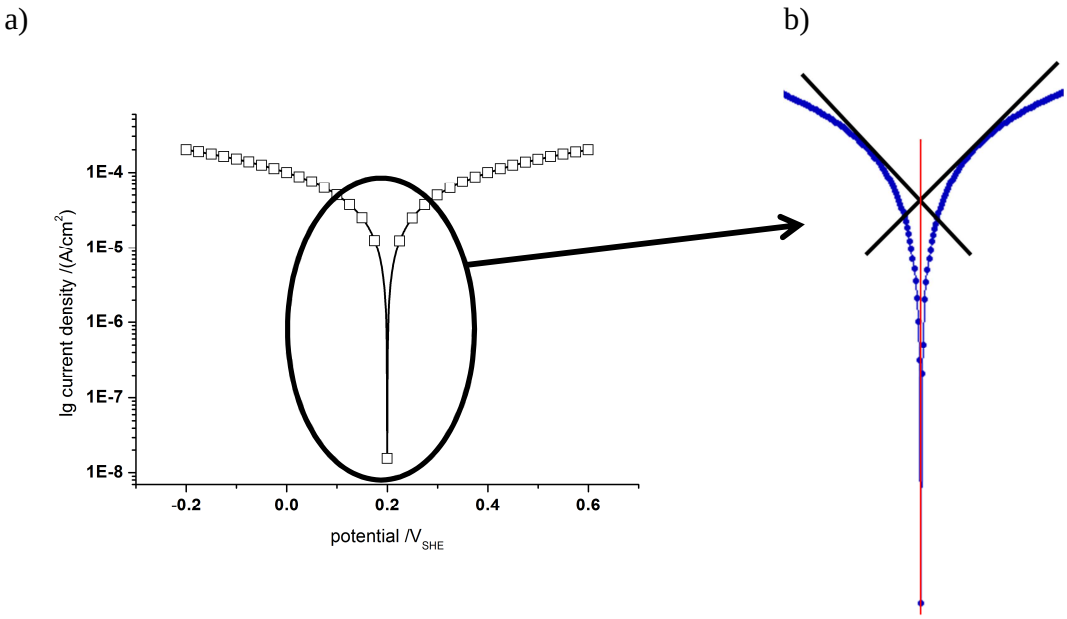

Figure 7: current density – potential curve as Tafel plot (a) with indicated tangents and OCP in the enlargement (b)

The logarithm of the absolute current value is plotted versus the overpotential. Building a triple point between the OCP and tangents, on each the cathodic branch and the anodic branch at a range of 80 mV, leads to the corrosion current density [102, 103].

2.4.3. Electrochemical impedance spectroscopy (EIS)

The most important law to describe electrochemical impedance spectroscopy is Ohm's law:

$$R = \frac{E}{I} \qquad \text{(Eq. 14 [104])}$$

with: R: resistor, E: voltage, I: current

The resistor indicates the resistance of a circuit against current flow. But Ohm's law is only valid for an ideal resistor which is frequency independent, it follows the Ohm's law for every current and voltage and AC current and voltage signal are in phase [104].

Another element of the circuit measured by EIS is the capacitor. The easiest way to describe a capacitor is the two-plate capacitor. Two conductive plates are separated by a non-conductive material in a determined distance. Connected with a power source the capacitor is charged and the amount of the charge a capacitor can be charged with is the capacitance. This charge can be calculated by:

$$q = CV \qquad \text{(Eq. 15 [104])}$$

with: q: amount of charge, C: capacitance, V: voltage

Since the capacitance is determined by the geometry of the capacitor it can be calculated by:

$$C = \frac{\varepsilon \varepsilon_0 A}{d} \qquad \text{(Eq. 16 [104])}$$

with: C: capacitance, A: surface area of the plates, d: distance between the plates, ε_0: dielectric constant in vacuum, ε: dielectric constant of the non-conductive material

When a voltage is applied to a material dipoles are induced which orientate themselves in the direction of the electric field. If the voltage was alternating, the dipoles should rotate with the same frequency. The time delay between the frequency of the AC and the rotation of the

dipoles is called relaxation. In EIS, a small AC voltage of about 10-20 mV with varying frequency is applied to the system and the resulting current is detected as a function of time [105].

As a sinusoidal expressed for the voltage and the current it follows:

$$E_t = E_0 \cdot \sin(\omega t) \qquad \text{(Eq. 17 [104])}$$

with: E_t: potential at time t, E_0: amplitude of the given signal, ω: radial frequency, θ: phase shift

$$I_t = I_0 \cdot \sin(\omega t + \phi) \qquad \text{(Eq. 18 [104])}$$

with: I_t: current at time t, I_0: amplitude of the response signal, ω: radial frequency, ϕ: phase shift

Taking Ohm's law (Eq. 14) into account the impedance can be calculated with the following equation:

$$Z = \frac{E_t}{I_t} = \frac{E_0 \cdot \sin(\omega t)}{I_0 \cdot \sin(\omega t + \phi)} = Z_0 \cdot \frac{\sin(\omega t)}{\sin(\omega t + \phi)} \qquad \text{(Eq. 19 [104])}$$

with: Z: impedance, Z_0: magnitude of impedance, E_t: potential at time t, I_t: current at time t, E_0: amplitude of the given signal, I_0: amplitude of the response signal, ω: radial frequency, ϕ: phase shift

If the impedance is now plotted with the log of the frequency on the X-axis and the absolute values of the impedance $(|Z| - Z_0)$ and the phase shift are each on two Y-axes, a Bode Plot can be constructed, in which the frequency dependent information can be visualized as shown in Figure 8 [105].

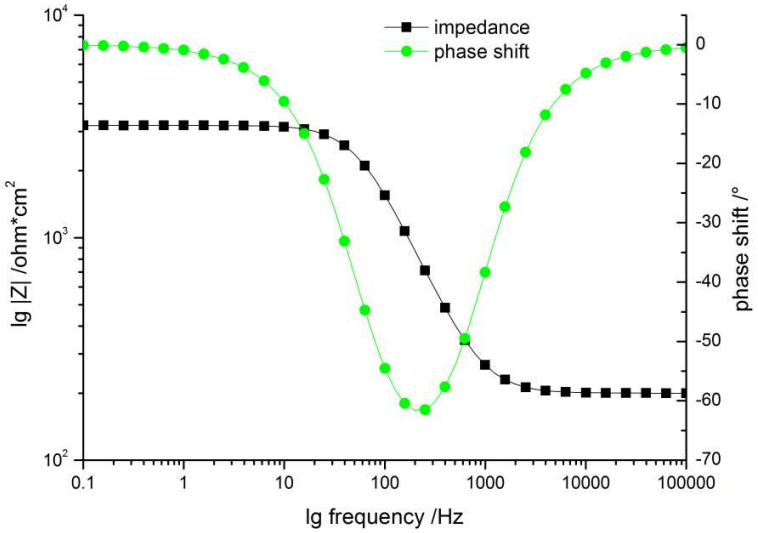

Figure 8: Bode plot of the electrochemical impedance measurement of a dummy cell (Gamry instruments)

For the EIS measurement of an organic coating on a metal substrate, the interpretation of the impedance data is complex. As the coating is in contact with an aqueous electrolyte, pores play a crucial role on the appearance of the Bode plot. The whole system can be described by an equivalent circuit diagram consisting of different resistors and capacitors. The capacitance of the coating, the double-layer capacitance between the metal and the electrolyte, the polarization resistance between the metal and the electrolyte, the pore resistance of the coating and the electrolyte resistance determine the Bode plot [105].

Typically the frequency range for an EIS measurement is from 0.01-10^5 Hz. For small frequencies the three resistors dominate the impedance values, whereas the value of the solution resistance is constant and negligible small with respect to the polarization and the pore resistance, followed by the double-layer capacitor, followed by the pore resistance combined with the electrolyte resistance, followed by the coating capacitance and finally for high frequencies the electrolyte resistance [105].

According to the equation:

$$C = \frac{1}{2\pi f|Z|} \qquad \text{(Eq. 20 [106])}$$

with: C: capacitance, f: frequency, Z: magnitude of the impedance

the capacitance at the frequency where the phase shift is 90° can be calculated.

Using the equation of Brasher and Kingsbury:

$$\varphi = \frac{log\left(\frac{C_p}{C_{p,0}}\right)}{log(\varepsilon_w)} \qquad \text{(Eq. 21 [106])}$$

with: φ: water uptake, C_p: capacitance of the coating after time, $C_{p,0}$: capacitance of the coating at time = 0 (before water uptake), ε_w: dielectric constant of water

the water uptake over time of the organic coating can be calculated and plotted versus time.

2.4.4. Coulometry

By use of coulometry the amount of charge is calculated which leads to a quantitative electro oxidation or electro reduction of a chemical species in a given time. It is calculated by:

$$Q = \int_0^t i dt \qquad \text{(Eq. 22 [101])}$$

with: Q: amount of charge, i: current, t: time

Taking the Faraday's constant into account, which is the amount of charges to produce an equivalent weight of the oxidized or reduced element, the mass of the element produced at the electrode of interest can be calculated:

$$m_k = \frac{M_k}{nF} \int_0^t i_k dt \qquad \text{(Eq. 23 [101])}$$

with: m_k: produced mass of element k, M_k: molar mass of element k, n: number of electrons taking part in the electrode reaction, F: Faraday constant, i_k: applied current, t: time

As long as no side reactions like electrochemical reactions of the solvent, the electrode material, components of the supporting electrolyte or secondary electrode reactions by the reaction products, it can be assumed that 100 % of the charges are used for the desired electrode reaction. To reduce the electrolyte side reaction a potential window is given for each electrolyte where nearly no redox reactions take place. For a typically used aqueous electrolyte this window is between the hydrogen and the oxygen evolution from 0 V_{SHE} to 1.23 V_{SHE} [101].

2.5. Inductively coupled plasma analysis of electrolytes

With the help of inductively coupled plasma – optical emission spectroscopy the qualitative and quantitative investigation of dissolved elements in an electrolyte is possible. The electrolyte is nebulized in a nebulizer chamber by use of the carrier gas which is the same gas as the plasma gas, typically argon. This aerosol is sprayed into the plasma. For this in a torch with three tubes the plasma is generated. Between the outer tube which isolates the plasma from the induction coil and the intermediate tube the auxiliary gas flows which shapes the plasma. The plasma gas flows between the intermediate tube and the sample injector tube and is ignited by a high-frequency field through the surrounding induction coil. Caused by a skin effect, generated by the hf field, a zone with lower viscosity appears in the center of the plasma. This is where the sample aerosol is sprayed in. The center is divided in further zones. Close to the injector tube is the atomization zone followed by the atomic line emission zone and finally close to the head of the plasma the ionic line emission zone. The advantage of

using argon plasma is that argon emits a simple spectrum, is able to excite and ionize most of the elements and, as it is an inert gas, no reaction products are formed between argon and the electrolyte elements [101].

Excited by the argon plasma each element radiates photons with element specific frequency or wavelength when the electrons shift back to a lower or the ground state. This frequency or wavelength can be calculated by:

$$h\nu = h\frac{c}{\lambda} = E_m - E_k \qquad \text{(Eq. 24 [101])}$$

with: h: Planck's constant, ν: frequency, c: speed of light in vacuum, λ: wavelength, E_m: upper energy level, E_k: lower energy level

As detector a photomultiplier tube (PMT) was used for a long time. By use of a photomultiplier instead of a photographic plate larger wavelength coverage was achieved. A photocathode converts the photons into electrons which are amplified by dynodes. Since the photomultiplier is a single detector it was replaced by multichannel detectors like the charge-transfer device (CTD) which is based on charged-coupled devices (CCD). The CCD chips are arranged in a Rowland circle which means that the concave chips are arranged on the outside of a circle which has, on the points of contact between the chips and the circle, the same curvature as the chips have. The advantage of the Rowland circle is that it combines the diffraction of a reflection grating with the imaging of a concave mirror. Therefore the diffracted beams with varying wavelengths are focused on the circle [101].

If a calibration curve was prepared for each element not only qualitatively but as well quantitatively the amount of each element in the electrolyte can be examined by the wavelength and its intensity. Depending on the electrolyte the limit of detection is for liquids between 1 ng/mL and 1000 ng/mL where ionic lines usually are more sensitive than the atomic lines [101].

The detection limit is strongly influenced by the matrix. Phosphor as an example interferes with the element lines of calcium. In the presence of phosphoric acid or sulfuric acid ArP^+ or

ArS^+ species can combine as well as $ArNa^+$, $ArNi^+$, $ArGa^+$ or $ArSe^+$ if these elements are present in the electrolyte [107].

For alkali metals the alkali effect leads to a decrease in the real signal of the other electrolyte elements since, caused by the rapid ionization of alkali metals like Na and K, their atom population increases in the plasma, leading to an increase of the signal intensity of all alkali metals. By use of an ionization buffer like $CsCl_2$ the alkali effect is decreased and realistic values for the non-alkali metal elements of the electrolyte can be detected [108].

2.6. Laser scanning confocal microscopy

Confocal microscopy, as described in chapter 2.3, enables the increase of spatial resolution by filtering undesired scattered light [95].

For a 3D image it is necessary to examine every point of the sample surface which is in focus for its absorption, scattering or emitting of light without overlaying information from points out of focus. Each point must be fully excited and the emitted light from each point must be displayed. One possibility is the radiation for a fixed period of time point by point by scanning the sample. The emission signal of each measurement point is collected in a photomultiplier tube (PMT) and imaged in a 3D map [95].

A further possibility to create a 3D map of a sample is the use of a multipinhole Nipkow spinning disk. In a helical order holes are arranged in the disk, which are each in a different focus of the objective lens. The disk is illuminated by a parallel light beam which leads to excitation of varying focus levels on the sample by rapidly spinning the disk. By use of charge-coupled devices (CCD) the emitted information are gathered. With the help of a step-by-step motor the sample is scanned and a 3D image can be displayed [95].

To increase the resolution in x- and y-direction smaller pinholes can be used which decreases the light intensity and hence the emitted information especially for dark samples. The resolution in z-direction can be modified by the numerical aperture of the objective lens, the wavelength of the light beam, the pinhole size, the refractive index of the components along the light path and the adjustment of the light path [95].

2.7. Adhesion analysis

Phenomenological the adhesion can be described best by the explanation of van der Waals forces between macroscopic solids. There are two ways to consider the van der Waals forces between bulky solids.

2.7.1. Microscopic approach

As the interaction between two molecules is attractive the potential energy of the interaction is negative and can be calculated by:

$$W_{AB}(D) = -\frac{C_{AB}}{D^6} \qquad \text{(Eq. 25 [109])}$$

with: W_{AB}: potential energy of the interaction between molecules A and B, D: distance between molecules A and B, C_{AB}: dipole-dipole interaction between molecules A and B consisting of oriented dipole-dipole interaction (Keesom interaction), induced dipole interaction (Debye interaction) and dispersion interaction (London interaction)

For the calculation of the interaction between two solids, the next step is to expand one molecule to a body with a planar surface consisting of molecules B. Assuming that the density of the molecules B in the solid is constant and using cylindrical coordinates for the calculation of the interaction between molecule A and the surface consisting of molecules B, the potential energy for the interaction can be calculated by:

$$W_{Mol/plane} = -\frac{\pi \rho_B C_{AB}}{6D^3} \qquad \text{(Eq. 26 [109])}$$

with: $W_{Mol/plane}$: potential energy between molecule A and planar surface consisting of molecules B, ρ_B: density of molecules B, C_{AB}: dipole-dipole interaction between molecules A and B consisting of oriented dipole-dipole interaction (Keesom interaction), induced dipole interaction (Debye interaction) and dispersion interaction (London interaction), D: distance between molecule A and planar surface

Expanding molecule A to a planar surface consisting of molecules A integration over all molecules A in the surface and dividing by the surface area leads to the van der Waals energy density:

$$w = \frac{W_{AB}}{A} - \frac{\pi \rho_A \rho_B C_{AB}}{12 D^2} \qquad \text{(Eq. 27 [109])}$$

with: w: energy per unit area, W_{AB}: potential energy between surface consisting of molecules A and surface consisting of molecules B, A: surface area, ρ_A: density of molecules A, ρ_B: density of molecules B, C_{AB}: dipole-dipole interaction between molecules A and B consisting of oriented dipole-dipole interaction (Keesom interaction), induced dipole interaction (Debye interaction) and dispersion interaction (London interaction), D: distance between molecule A and planar surface, D: distance between surface consisting of molecules A and surface consisting of molecules B

Introducing the Hamaker constant which is different for every molecule pair:

$$A_H = \pi^2 C_{AB} \rho_A \rho_B \qquad \text{(Eq. 28 [109])}$$

with: A_H: Hamaker constant, C_{AB}: dipole-dipole interaction between molecules A and B consisting of oriented dipole-dipole interaction (Keesom interaction), induced dipole interaction (Debye interaction) and dispersion interaction (London interaction), ρ_A: density of molecules A, ρ_B: density of molecules B

the energy density simplifies to:

$$w = -\frac{A_H}{12 \pi D^2} \qquad \text{(Eq. 29 [109])}$$

with: w: energy per unit area, A_H: Hamaker constant, D: distance between surface consisting of molecules A and surface consisting of molecules B

For surfaces with different geometries and considering attractive and repulsive interactions the van der Waals energy can be calculated by:

$$W = -\frac{A_H}{6D} \cdot \frac{R_1 R_2}{R_1 + R_2} \qquad \text{(Eq. 30 [109])}$$

with: A_H: Hamaker constant, D: distance between solids A and B, R_1: radius of surface A, R_2: radius of surface B

2.7.2. Macroscopic approach

The Lifshitz theory, used for the macroscopic approach of the interaction between two solids, takes into account the interaction between the molecules in the same solid. By interaction between e.g. two molecules of A the polarizability might change. This is missing in the microscopic approach. Lifshitz introduces bulk properties for each material like dielectric permittivity or the refractive index. Taking these properties into account, the Hamaker constant for two interacting materials with a third material in between is calculated by an integral over many frequencies using the dielectric permittivity constants of the three materials:

$$A_H = \frac{3}{4} k_B T \cdot \left(\frac{\varepsilon_1 - \varepsilon_3}{\varepsilon_1 + \varepsilon_3}\right) \cdot \left(\frac{\varepsilon_2 - \varepsilon_3}{\varepsilon_2 + \varepsilon_3}\right) + \frac{3h}{4\pi} \cdot$$

$$\int_{\nu_1}^{\infty} \left(\frac{\varepsilon_1(i\nu) - \varepsilon_3(i\nu)}{\varepsilon_1(i\nu) + \varepsilon_3(i\nu)}\right) \cdot \left(\frac{\varepsilon_2(i\nu) - \varepsilon_3(i\nu)}{\varepsilon_2(i\nu) + \varepsilon_3(i\nu)}\right) d\nu \qquad \text{(Eq. 31 [109])}$$

with: A_H: Hamaker constant, k_B: Boltzmann constant, T: absolute temperature, ε_1, ε_2, ε_3: dielectric permittivity constants of material 1, 2 and 3, iv: imaginary frequencies, h: Planck constant

With the help of the Hamaker constant, it is possible to determine if the interaction between two solids in the presence of a third medium was either attractive (positive Hamaker constant) or repulsive negative Hamaker constant) [109].

Interactions between similar materials are attractive as well as the interaction in vacuum. In the presence of a condensed phase or a thin, liquid phase van der Waals forces might be repulsive when the interaction between medium 1 and 3 is more attractive than between medium 1 and 2 [109].

For macroscopic investigations the use of a peel test is a common tool to examine the adhesion indirectly with the help of the peel force. Originally the peel test was used for the investigation of flexible laminates used in packaging and electronic industries [110].

The geometry of the peel arm, like the thickness and the width, as well as the environmental temperature, the humidity, the peel rate and the peel angle, affects the peel force immense.

In Figure 9 the peel test is illustrated with indicated width b and thickness h of the adhesive film which is the peel arm and the peel angle θ.

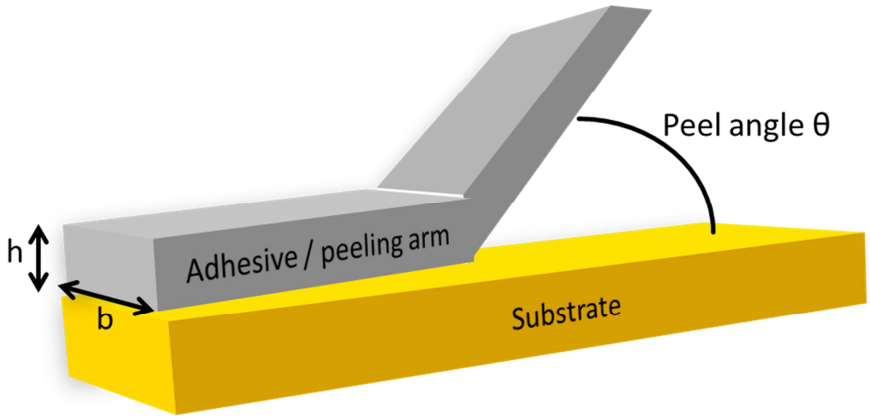

Figure 9: schematic illustration of the peel test [110]

During the peel test the adhesive is subject to tensile deformation which leads to a stored strain-energy in the adhesive and plastic or viscoelastic energy dissipation. Because of this the peel force measured, is incorrect since not only the force for de-adhesion of the adhesive from the substrate is detected but as well the energy dissipation in the plastic or viscoelastic zone at the delamination front [110].

In addition the plastic bending and the ratio between the tensile load and the in-plane shear load, which are affected by the peel angle, make it very difficult to detect a comparable adhesive fracture energy for the same adhesive [110].

Kinloch et al. [110] showed that under consideration of the stored strain energy in the adhesive, the energy used for tensile deformation and the bending energy of the adhesive, a geometry independent and material characteristic value for the adhesive fracture energy can be achieved which only includes the energy for de-adhesion of the adhesive from the substrate and the energy at the delamination front in the plastic or viscoelastic zone.

Williams and Kauzlarich [111] correlated the peel force with the peel angle. They could show that with smaller peel angles aberrations from linear elastic behavior of the adhesive became stronger. With thinner film thickness the bending energy could be neglected. A new model was established to analyze the non-linearity between load and extension and the energy dissipation in the adhesive layer affected by peel rate and peel angle.

For the calculation and evaluation of the temperature between two polymer films during a sealing process, Meka and Stehling [112] used the T-peel test. In this test two peeling arms were peeled at a peel angle of 180 °C. They explained that the maximum of the extension force just before the sample is damaged is the seal strength. Increasing the extension led to either peeling failure at the interface between the two adhesives, or a cohesive failure in one or both of the peeling arms by which the seal strength was higher than the bulk strength of the adhesive or a mixture of both.

These failures can be observed for the fixed-arm peel test, described above, too.

2.8. Contact angle measurement

Contact angle measurement is one of the most common tools to determine the surface tension of a solid surface. The angle between the solid surface and a tangent at the triple point between the solid phase, the liquid phase and the gas phase, determined in the liquid phase, as it can be seen in Figure 10, is called contact angle [109].

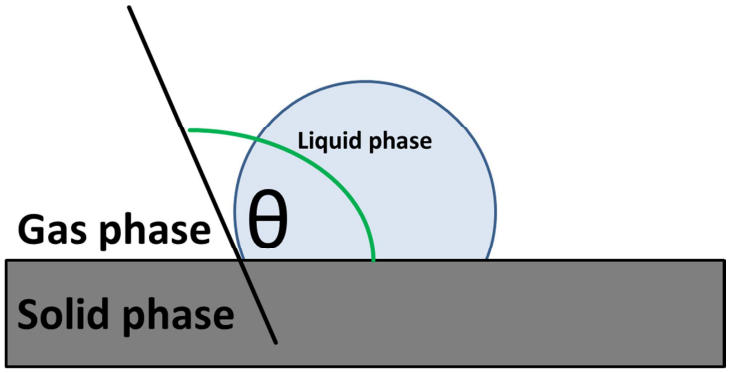

Figure 10: determination of the contact angle [109]

For water as liquid phase, according to Young's equation:

$$\gamma_L cos\theta = \gamma_S - \gamma_{SL} \qquad \text{(Eq. 32 [109])}$$

with: γ_L: interfacial tension of the liquid phase, γ_S: interfacial tension of the solid phase, γ_{SL}: interfacial tension between the liquid and the solid phases, θ: contact angle

a contact angle θ > 90° indicates a hydrophobic surface and a contact angle θ < 90° a hydrophilic surface vice versa.

For a homogeneous surface the contact angle can be calculated by the Young-Laplace equation taking the contour of the droplet into account:

$$\Delta P = \gamma \left(\frac{1}{R_1} + \frac{1}{R_2}\right) \qquad \text{(Eq. 33 [109])}$$

with: ΔP: pressure difference between the liquid and gaseous phases, γ: surface tension of the liquid, R_1 and R_2: radii of curvature of the drop, perpendicular to each other, which means for a drop that $R_1 = R_2$

For inhomogeneous surfaces, the contour of the droplet might be elliptically or even of an indefinable shape. Therefore two tangents are applied one on each side of the droplet and the left and right contact angle are measured individually.

In the case of an inhomogeneous surface, the dynamic contact angle measurement can be used instead of the static to determine the contact angle hysteresis. Increase of the droplet volume during a continuous contact angle measurement leads to an increase of the contact angle at first, until the droplet wets the surface and the contact angle decreases immediately. The contact angle just before the wetted surface increases is the advancing contact angle (θ_{adv}). Microscopically, the liquid is all the time at the same contact angle with the surface. With respect to the contour of an imperfection on the heterogeneous surface on macroscopic point of view the contact angle increases until the imperfection is wetted as it is illustrated in Figure 11. Decreasing the droplets volume reverses this effect. Until a de-wetting occurs, the contact angle decreases. The contact angle just before the wetted surface decreases is the receding contact angle (θ_{rec}) and is typically smaller than the advancing contact angle.

Subtraction of the receding contact angle from the advancing leads to the contact angle hysteresis which indicates the degree of inhomogeneity [109].

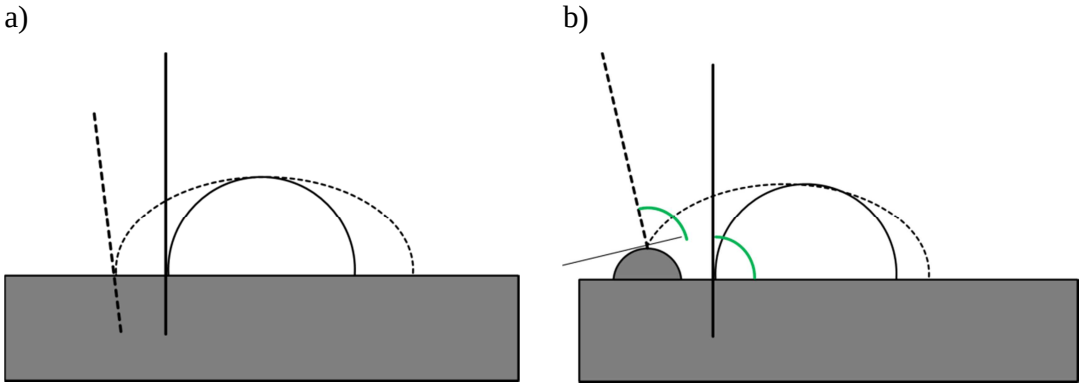

Figure 11: advancing contact angle behavior for a heterogeneous surface a) macroscopic and b) microscopic [109]

3. Experimental procedure

3.1. Investigations of magnesium and its alloys

3.1.1. Sample preparation

3.1.1.1. Cleaning step

The Mg AZ31 samples were received by DECHEMA (DFI, Frankfurt a.M., Germany). They were polished successively with SiC grinding paper P240, P600, P1000, P2500 and P4000 until they had a mirror-like finish. Afterwards they were cleaned with cotton wool soaked with ethanol abs. (p.a., Merck KGaA, Darmstadt, Germany) before they were additionally cleaned in ethanol abs. (p.a., Merck KGaA, Darmstadt, Germany) for 10 min in an ultrasonic bath (Ultrasonic Cleaner, 45 kHz, 120 W, VWR International GmbH, Darmstadt, Germany). After rinsing with ultra-pure water (SG Ultra Clear UV Plus, Evoqua Water Technologies, Günzburg, Germany) the samples were etched in a stirred aqueous solution (528.4 g/L $Al(NO_3)_3$ x $9H_2O$ (p.a. Merck KGaA, Darmstadt, Germany), 54.8 g/L citric acid x H_2O (≥99.5 % Merck KGaA, Darmstadt, Germany), 100 mL/L glycolic acid (70 % aqueous, p.a. Merck KGaA, Darmstadt, Germany)) at room temperature for 30 s and directly rinsed with ultra-pure water (SG Ultra Clear UV Plus, Evoqua Water Technologies, Günzburg, Germany). Then the samples were etched in a stirred aqueous NaOH solution (4 mol/L, p.a. Merck KGaA, Darmstadt, Germany), rinsed with ultra-pure water (SG Ultra Clear UV Plus, Evoqua Water Technologies, Günzburg, Germany) and dried in an air stream.

3.1.1.2. Ultrasonic treatment

The freshly cleaned samples were treated on one hand in ultra-pure water (SG Ultra Clear UV Plus, Evoqua Water Technologies, Günzburg, Germany) and on the other hand in an aqueous $Ce(NO_3)_3$ solution (0.5 mol/L $Ce(NO_3)_3$ x $6H_2O$, 99.5 % Alfa Aesar, Karlsruhe, Germany) for 20 min with UIP 1000 hd (Hielscher Ultrasonics, Teltow, Germany). The distance between the sonotrode and the sample was 3 cm and the power was set to 44 W/cm^2. After the ultrasonic treatment the samples were rinsed with ultra-pure water (SG Ultra Clear

UV Plus, Evoqua Water Technologies, Günzburg, Germany) and dried in an air stream. The ultrasonic process is illustrated in Figure 12.

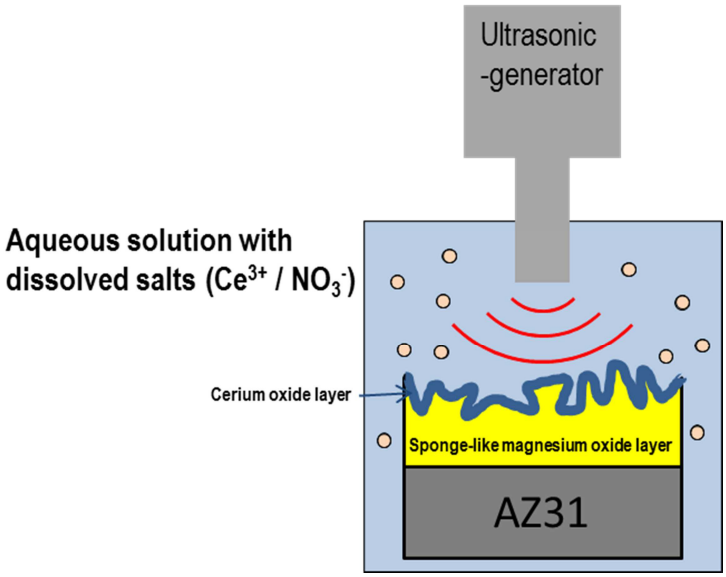

Figure 12: schematic illustration of the ultrasonic process for the formation of sponge-like oxide layers

3.1.1.3. Cross-cuts

For the investigation of cross-cuts of the ultrasonically generated Ce/Mg/O layers the $Ce(NO_3)_3$ treated samples were embedded on edge in Technovit 4002 (Heraeus Kulzer GmbH, Wehrheim, Germany) and cut. The cut edge was polished successively with SiC grinding paper P240, P600, P1000, P2500 and P4000 until they were mirror-like, cleaned with ethanol abs. (p.a., Merck KGaA, Darmstadt, Germany) and dried in an air stream.

3.1.2. Field emission scanning electron microscopy (FE-SEM) and energy dispersive X-ray spectroscopy (EDX)

The FE-SEM images were done with a NEON 40 FE-SEM (Carl Zeiss SMT AG) or with an 8500 FE-SEM (Agilent Technologies).

EDX measurements were done with a NEON 40 (Carl Zeiss SMT AG) or with a XL 40 ESEM (Philips).

3.1.3. Raman spectroscopy

The Raman spectroscopy was done with an In Via Raman Spektroskop and Leica DM 2500 M Mikroskop (Renishaw, Pliezhausen, Germany). An Ar-Laser (633 nm) at 1.75 mW and an N PLAN objective 100x were used. The accumulation was 30 s.

3.1.4. Potentiodynamic studies

Current density – potential curves were measured in a custom-made electrochemical cell with a measurement diameter of 5 mm. As reference electrode an Ag/AgCl (sat. KCl) electrode was used. The potentiostat was a Gamry Ref. 600 (Gamry Instruments). The potential was scanned from -0.6 V to +1.0 V vs. OCP with a scan rate of 5 mV/s. The free corrosion potentials were measured for 120 s before the current density – potential measurements were started. As electrolyte a borate buffer (H_3BO_3 (12.4 g/L, p.a., Merck KGaA, Darmstadt, Germany), Na_2SO_4 (7.1 g/L, p.a., Merck KGaA, Darmstadt, Germany), $Na_2B_4O_7$ x 10 H_2O (19.1 g/L, p.a., Merck KGaA, Darmstadt, Germany), in ultra-pure water (SG Ultra Clear UV Plus, Evoqua Water Technologies, Günzburg), pH = 8.3) containing 0.05 mol/l NaCl (p.a., Merck KGaA, Darmstadt) was used.

3.1.5. Electrochemical impedance spectroscopy (EIS)

EIS measurements were done in a custom-made electrochemical cell with a measurement diameter of 5 mm. As reference electrode an Ag/AgCl (sat. KCl) electrode was used. The potentiostat was a Gamry Ref. 600 (Gamry Instruments). As electrolyte a borate buffer (H_3BO_3 (12.4 g/L, p.a., Merck KGaA, Darmstadt, Germany), Na_2SO_4 (7.1 g/L, p.a., Merck KGaA, Darmstadt, Germany), $Na_2B_4O_7$ x 10 H_2O (19.1 g/L, p.a., Merck KGaA, Darmstadt,

Germany), in ultra-pure water (SG Ultra Clear UV Plus, Evoqua Water Technologies, Günzburg), pH = 8.3) containing 0.05 mol/l NaCl (p.a., Merck KGaA, Darmstadt) was used. Before each EIS measurement the OCP was detected for 60 s. EIS was done from 10000 Hz until 0.1 Hz with 10 points/decade versus OCP and an AC Voltage of 10 mV rms.

3.1.6. Adhesion analysis (Peel test)

To investigate the adhesion properties of the synthesized layers the PEEL-force was measured on a MV-220 Motorized Test Stand with dynamometer model ZP-5 (Imada) at an angle of 90° to the surface in >90 % r.h. A model epoxy primer (Henkel, Düsseldorf, Germany) was coated with 120 µm layer thickness and dried for 75 min at 120 °C. Then the samples were stored for 24 h at 40 °C and 100 % r.h. before the measurement was done. An illustration of the Peel-test set-up is shown in Figure 13.

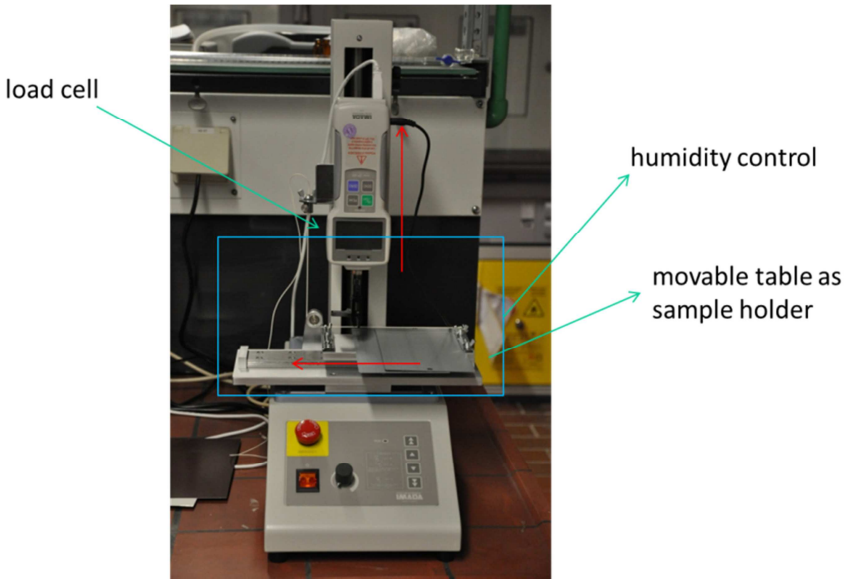

Figure 13: photography of the Peel-test set-up with illustrated box for humidity control

3.2.Investigations of hot-formed zinc alloy coated steel parts

3.2.1. Sample preparation

As substrates, different zinc alloy coated 22MnB5 steel sheets were studied, which are currently investigated by the BMW AG. Hot dipped galvanized zinc sheet, or more specifically 22MnB5 steel coated with Z140, which is also used as base material for the indirect hot-forming process and is comparable to a cold-formable steel coated with Z100, was used as reference with and without annealing. A galvannealed zinc alloy with 8-12 wt.-% Fe and an electroplated Zn-Ni alloy with about 10 wt.-% Ni, both currently studied for the direct hot-forming process, were investigated.

With regard to the hot-forming process and according to the different heat capacitance of the different alloys the oven times and temperatures were chosen so that all samples underwent a comparable heat treatment. The samples and process conditions are shown in Table 1.

Table 1: Investigated alloy coated substrates and hot-forming conditions

	Sample	**process conditions I (Temperature, processing time)**	**process conditions II (Temperature, processing time)**	**process conditions III (Temperature, processing time)**
1)	Z140/Gl70/70 layer thickness ca. 10 µm	-	-	-
2)	Z140/Gl70/70 hot-formed layer thickness after hot-forming ca. 20-30 µm	910 °C, 4 min	910 °C, 5 min 20 s	910 °C, 8 min
3)	Zn/Fe hot-formed (ca. 8-12% Fe) layer thickness after hot-forming ca. 20 µm	910 °C, 4 min	910 °C, 6 min	910 °C, 9 min
4)	Zn/Ni hot-formed (ca. 10% Ni) layer thickness after hot-forming ca. 20 µm	900 °C, 5 min	900 °C, 7 min	900 °C, 11 min

After the hot-forming all heat treated samples, except Al/Si, were treated by shot blasting to remove oxide scales. Before each analytical measurement, the samples were solvent cleaned with tetrahydrofurane (p.a., Merck KGaA, Darmstadt), isopropyl alcohol (p.a., Merck KGaA, Darmstadt) and ethanol abs. (p.a., Merck KGaA, Darmstadt) each for 10 min in an ultrasonic bath (Ultrasonic Cleaner, 45 kHz, 120 W, VWR International GmbH, Darmstadt).

For the investigation of the welding spots, two pieces of each alloy (2x4 cm^2) were welded together with a welding point of 8 mm in diameter. The welding spots were investigated without pulling them apart as line-scan on top of the welding point, which was in contact with the Cu-electrode, like illustrated in Figure 14.

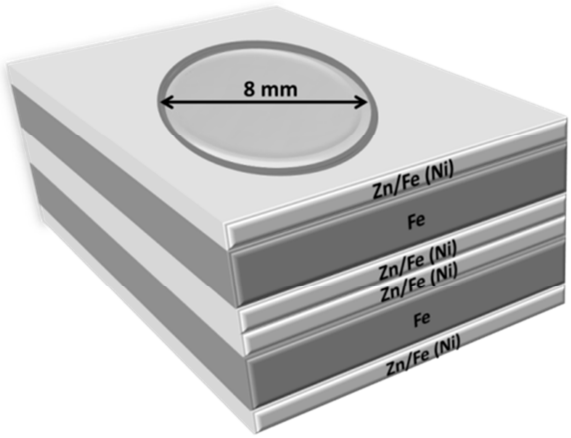

Figure 14: Schematic illustration of the welding spot with an indication of the range of the line-scan

For the investigations of cut edges two samples of each alloy coating were embedded, put for one cycle in a climate change test, derusted and the resulting topography was detected by laser scanning confocal microscopy as described in chapter 2.6.

3.2.2. Field emission scanning electron microscopy (FE-SEM) and energy dispersive X-ray spectroscopy (EDX)

The FE-SEM images were done with a NEON 40 FE-SEM (Carl Zeiss SMT AG) or with an 8500 FE-SEM (Agilent Technologies).

EDX measurements were done with a NEON 40 (Carl Zeiss SMT AG).

3.2.3. Raman spectroscopy

The Raman spectroscopy was done with an In Via Raman Spektroskop and Leica DM 2500 M Mikroskop (Renishaw, Pliezhausen, Germany). An Ar-Laser (633 nm) at 17.5 mW and an N PLAN objective 100x were used. The accumulation was 30 s.

3.2.4. Coulometric inductively coupled plasma – optical emission spectroscopy (ICP-OES)

Electrochemical ICP-OES measurements were done with a Spectro Arcos Edition EOP with horizontal torch box housing for axial plasma observation and cross-flow nebulizer. Plasma power was set to 1400 W, volume flow of cooling gas was at 18.0 L/min, support gas at 1.0 L/min and nebulizer gas at 0.77 L/min. The flow rate of the electrolyte was 2.0276 mL/min. The delay time between in-situ cell and plasma was 25 s. The in-situ cell was an in-house design flow cell with a working electrode area of 0.7 cm^2. As reference electrode an Ag/AgCl (sat. KCl) electrode and as counter electrode a graphite electrode isolated from the working electrode with a membrane were used. As potentiostat a SimPot (custom made at the MPIE, Düsseldorf) with maximum current of 100 mA was used. The electrolyte was a 0.1 mol/L KCl (p.A., Merck KGaA, Darmstadt) solution in ultra-pure water (SG Ultra Clear UV Plus, Evoqua Water Technologies, Günzburg). A current density of 4.29 mA/cm^2 was applied to the substrate and the resulting potential was detected by the potentiostat, while the dissolved metals were detected qualitatively and quantitatively by the ICP-OES.

The coulometric ICP-OES set-up is shown in Figure 15.

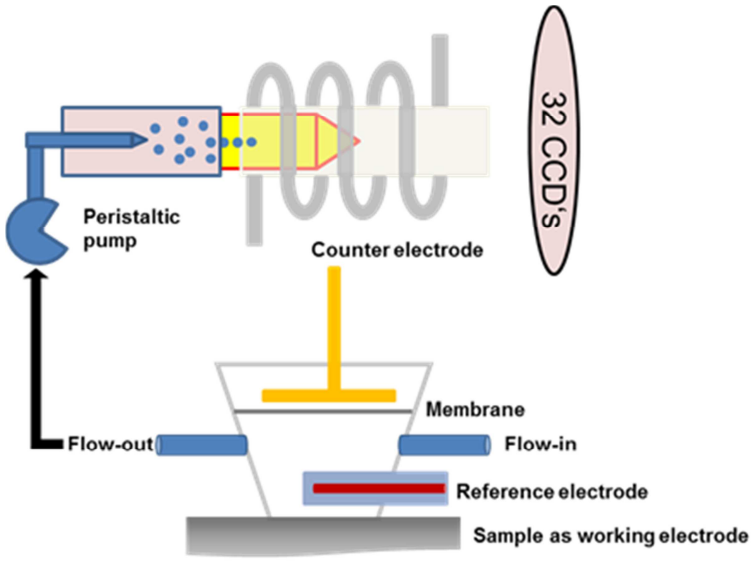

Figure 15: Schematic illustration of the coulometric ICP-OES measurement set-up

3.2.5. Potentiodynamic studies

Current density – potential curves were measured in a custom-made electrochemical cell with a measurement diameter of 5 mm. As reference electrode an Ag/AgCl (sat. KCl) electrode was used. The potentiostat was a Gamry Ref. 600 (Gamry Instruments). The potential was scanned from -0.3 V to +0.3 V vs. OCP with a scan rate of 2 mV/s. The free corrosion potentials were measured for 60 s before the current density – potential measurements were started. As electrolyte, a borate buffer (H_3BO_3 (12.4 g/L, p.a., Merck KGaA, Darmstadt, Germany), Na_2SO_4 (7.1 g/L, p.a., Merck KGaA, Darmstadt, Germany), $Na_2B_4O_7$ x 10 H_2O (19.1 g/L, p.a., Merck KGaA, Darmstadt, Germany), in ultra-pure water (SG Ultra Clear UV Plus, Evoqua Water Technologies, Günzburg), pH = 8.3) containing 0.05 mol/L NaCl (p.a., Merck KGaA, Darmstadt) was used.

3.2.6. Scanning capillary cell studies of welding spots

To investigate the cathodic corrosion protection of welding spots, a line-scan of the free corrosion potential across the welding spots was done with a scanning capillary cell. The capillary diameter was 1 mm. Hence the step-size for the line-scan was 1 mm. At each point the free corrosion potential was measured for 300 s and the final value, after the equilibrium was reached, was plotted. As electrolyte a 0.05 mol/L NaCl (p.a., Merck KGaA, Darmstadt) solution in ultra-pure water (SG Ultra Clear UV Plus, Evoqua Water Technologies, Günzburg) was used. The reference electrode was an Ag/AgCl electrode.

3.2.7. Investigations of cut edges

The embedded samples were put for one cycle in a climate change test. After photographing the samples, the corrosion products were etched with HCl (37 %, p.a., Merck KGaA, Darmstadt), rinsed with ultra-pure water (SG Ultra Clear UV Plus, Evoqua Water Technologies, Günzburg, Germany) and dried in an air stream.

Following this, the interfaces between the embedded samples were investigated by laser scanning confocal microscopy (VK-X210, Keyence, Neu-Isenburg, Germany) leading to a laser microscopic image and a 3D model of the surface.

A schematic figure of the laser scanning confocal microscope used in this thesis is shown in Figure 16.

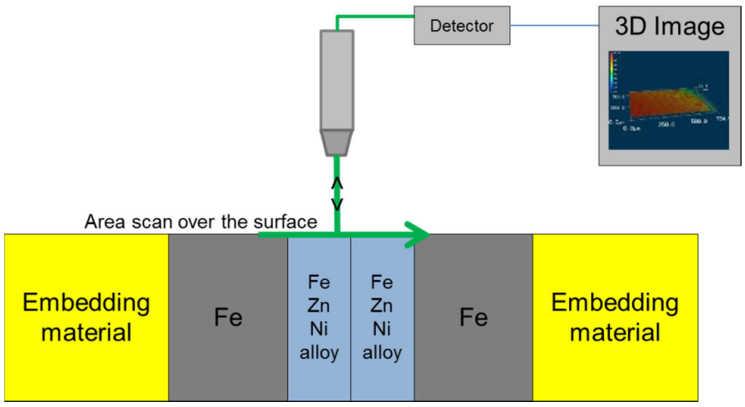

Figure 16: illustration of the laser scanning confocal microscopy of cut edges

3.3.Investigations of self-healing, organic coatings by means of in-situ contact angle measurement and uniaxial deformation

3.3.1. Sample preparation

The samples and the loaded capsules were prepared and synthesized by SINTEF Materials&Chemistry, Forskningsveien 1, N-0373 Oslo, Norway.

3.3.1.1. Cleaning step

HDG steel, delivered by Chemetall GmbH (Frankfurt a.M., Germany) was used as substrate. It was solvent-cleaned (tetrahydrofuran, isopropanol and ethanol (Prolabo)) and alkaline cleaned (Gardoclean / Gardobond, Chemetall (Frankfurt a.M., Germany)) before the coating application. An additional treatment with a conversion additive (Oxilan (Chemetall, Frankfurt a.M., Germany)) should function as an adhesion promoter.

3.3.1.2. Coating materials

The two-pack water-based epoxy resin (for primer and paint formulations) has been received from Mankiewicz Gebr. & Co. (Hamburg, Germany); the two-pack acrylic polyurethane coating components (aliphatic topcoat formulation) have been supplied by Varnish srl (Galliate, Italy).

3.3.1.3. Preparation of modified acrylic polyurethane coating applied on HDG substrates

As topcoat a flexible aliphatic- and acrylic-based polyurethane, generally used for automotive coatings in corrosion protection, has been modified with PU-hybrid containers (loaded with MTES = water-repellent agent). The coating was applied by tape-casting (100 µm wet-film thickness) on HDG samples. The content of microcontainers in the coating layer

was 10 wt.% (calculated to the cured coating). An unmodified topcoat was used in all studies as a control. Modification of topcoat formulation was carried out by mixing the A-component (magnetically stirring at 700 rpm for 15 min) and the solvent based particle dispersion. After adding the B-component the mixture was stirred (15 min) under vacuum to avoid air entrapped in the resin.

3.3.1.4. Preparation of modified epoxy coating applied on HDG substrates

The epoxy coating (model formulation of water-based epoxy resin) was modified with 6 %wt PU-mix microcontainers (loaded with TMODS and TMOS = water repellent agents). The coating was applied by repeated dip-coating on HDG samples resulting in a film thickness of 17 µm. Modification of the epoxy resin was carried out by simply mixing all components.

3.3.2. Uniaxial deformation

For the FE-SEM images the samples were stretched with a custom built linear tensile testing device (Kammrath & Weiß, Dortmund, Germany) up to 15 % elongation.

3.3.3. Field emission scanning electron microscopy (FE-SEM)

The FE-SEM images were done with a NEON 40 FE-SEM (Carl Zeiss SMT AG). To avoid charging effects, it was necessary to sputter the samples with a gold layer of around 1.5 nm (sputter coater Bal-Tec SCD 500).

3.3.4. Experimental set-up for measurement of the contact angle during uniaxial deformation

For the measurements of the contact angle during uniaxial deformation a new experimental set-up was developed consisting of a tensile testing device (Kammrath & Weiß, Dortmund, Germany) and a contact angle system (OCA 15 plus, Dataphysics, Filderstadt, Germany). The samples were cut to stripes of 1.0 cm x 5.0 cm and fixed between the jaws of the stretching machine in the way that a piece of 1.0 cm x 2.2 cm was free for deformation. The stretching machine was placed in an optical bench between the light source and the camera on a height-adjustable table. The height-adjustable syringe was approached to the sample until the needle was in position a few millimeters to the sample. Then a droplet of 4 µL of water was build and hanging on the needle. The sample was approached to the droplet until it was on the sample. The needle then is almost in contact with the sample and is in the center of the droplet. To measure the contact angle hysteresis the droplets baseline was found automatically by the software. Because the needle was in the droplet, its contour was elliptically. Settings for the ARCA measurements were dispensing 5 µL with 0.2 µL/s, waiting 10 s, withdrawing 5 µL with 0.2 µL/s, waiting 10 s, repeating 9 times. The sample was stretched with 20 µm/s until a deformation of about 35%. Simultaneously the measurement of the contact angle hysteresis, the stretching deformation and the ARCA were started.

An illustration of the test set-up is shown in Figure 17.

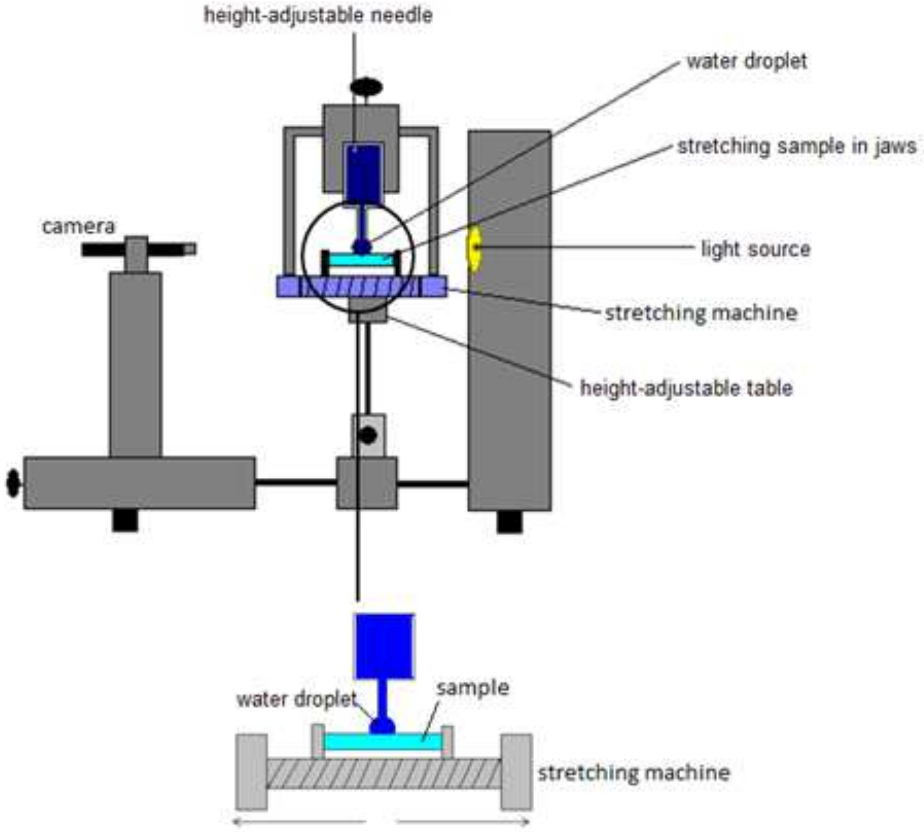

Figure 17: Illustration of the experimental set-up for the measurement of the contact angle during stretch forming with more detailed look on the schematic sample with droplet in the stretching device

4. Results and discussion

4.1. Formation of magnesium oxide layers by ultrasonic treatment

4.1.1. Field emission scanning electron microscopy (FE-SEM)

The SEM images in Figure 18 clearly show the grain boundaries of the alloy, after polishing and etching of the surface. After ultrasonic treatment in pure water the surface was coated with a homogeneous layer and the grain boundaries were covered. In the case of the ultrasonic treatment in 0.5 M cerium nitrate solution a sponge-like structure with 1-2 µm large cracks have been observed. The pathway of the crack formation looked similar to the grain boundaries on the freshly etched sample. Lin et. al showed that the crack formation depends on crystal growth and the layer thickness of the oxide layer. The crack formation and the characterization of the cracks as well as the avoidance of the cracks must be a point for further investigations.

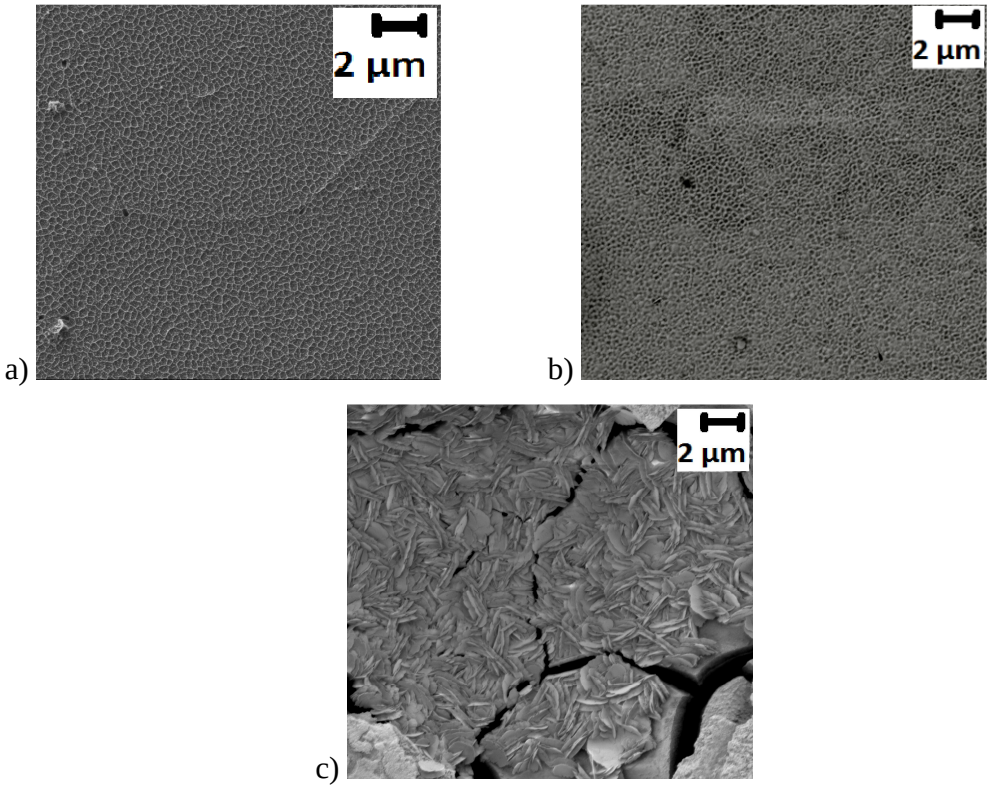

Figure 18: FE-SEM images of the AZ31 surface a) polished and etched b) after ultrasonic treatment in pure water c) after ultrasonic treatment in 0.5 M aqueous $Ce(NO_3)_3$-solution.

4.1.2. Energy dispersive x-ray spectroscopy (EDX)

Figure 19 shows the EDX mappings for the surface distributions of Mg, Ce and O.

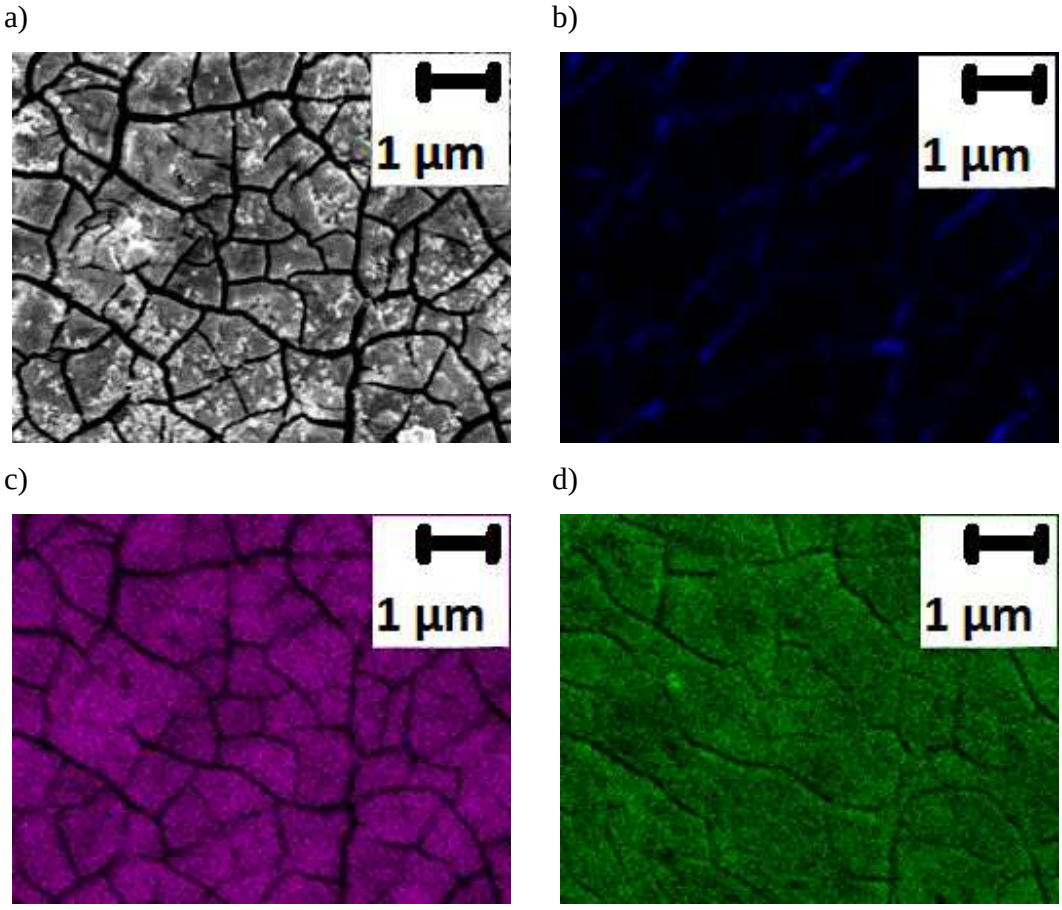

Figure 19: EDX mappings of the in $Ce(NO_3)_3$ solution ultrasonically treated AZ31 surface a) SEM image of the measured area, b) Mg distribution, c) Ce distribution and d) O distribution.

With the help of EDX mappings it could be shown that in the cracks in the oxide layer nearly no cerium species were detected. The magnesium oxide layer was revealed. Nevertheless, to a large extend it was shown that the magnesium oxide layer was covered with a cerium oxide layer, excluding the cracks.

To characterize the composition of the synthesized oxide layer and to investigate if the oxide was a mixed cerium-magnesium-oxide, cross-sections were prepared and analyzed by means of EDX. As seen in Figure 20, the oxide layer thickness was about 50 µm and primarily consisted of magnesium oxide. Only a very small layer of about 2 µm contained cerium oxide and overlaid the magnesium oxide layer. This result reflects the growth mechanism postulated by Qu et. al [113] and Godinho et. al [114] who described the formation of a porous, homogeneous MgO layer with enhanced corrosion protection properties by use of ultrasonic treatment and the formation of a CeO_2 layer from precipitated $Ce(OH)_4$.

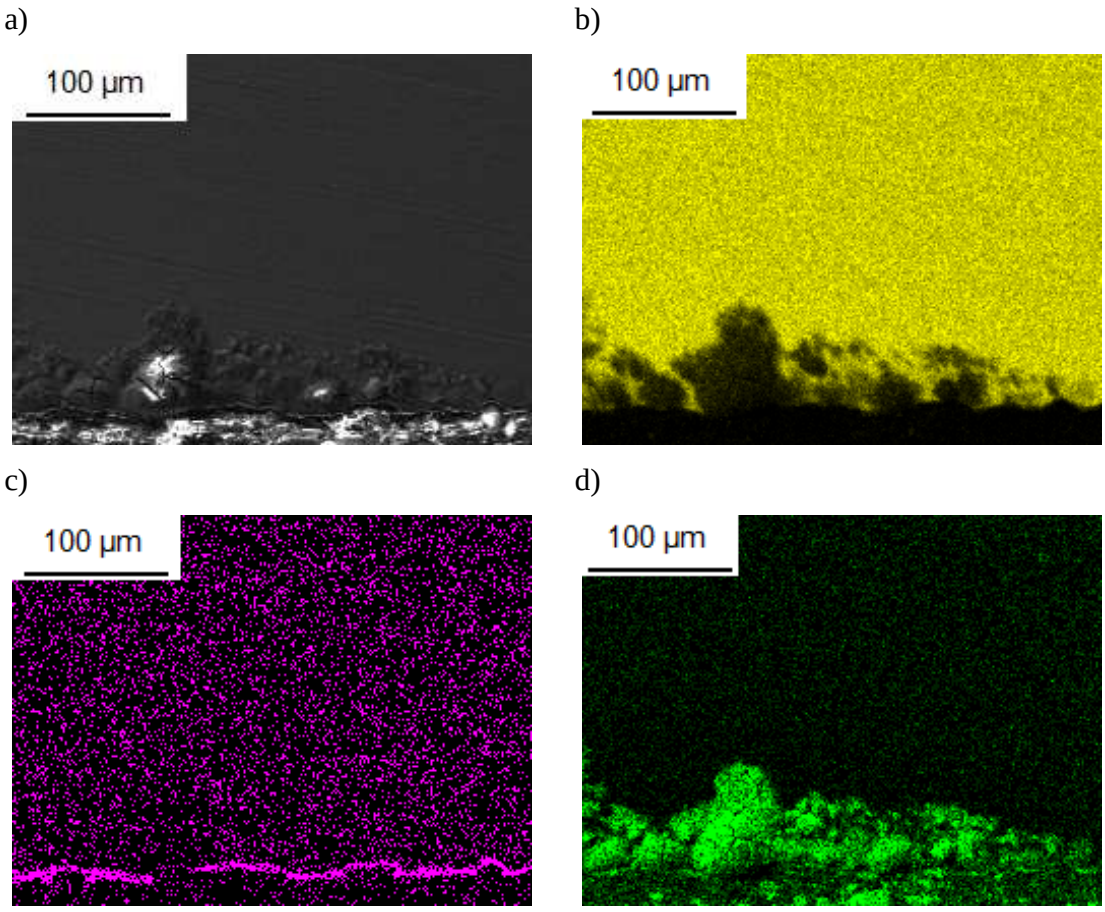

Figure 20: EDX mappings of the cross-section of the in $Ce(NO_3)_3$ solution ultrasonically treated AZ31 surface a) SEM image of the measured area, b) Mg distribution, c) Ce distribution and d) O distribution

4.1.3. Raman spectroscopy

As seen in Figure 21 the pure AZ31 alloy showed no Raman modes, indicating that the cleaning steps removed all contaminations. After ultrasonic treatment in water some typical modes for oxides and hydroxides of metals, treated in water [115], appeared. The Raman spectroscopy measurements of the samples with an ultrasonic treatment in cerium nitrate solution gave an evidence for the built-up of a cerium oxide layer, as the CeO_2 vibration mode at 465 cm^{-1} [116] was clearly visible in the spectrum as well as a small amount of NO_3 at 1048 cm^{-1} [117], which is conforming the EDX results.

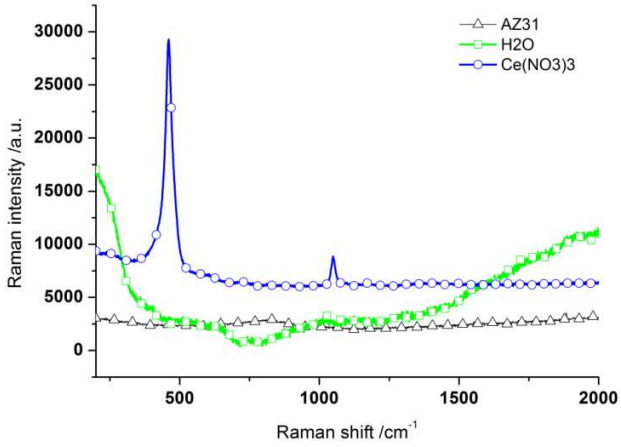

Figure 21: Raman spectrum of ultrasonically generated coatings a) without and b) with incorporation of Ce ions. The CeO2 vibration mode at 465 cm-1 [116] is clearly recognizable. As reference the Raman spectrum of a pure AZ31 surface is given.

4.1.4. Potentiodynamic studies

The current density – potential curves, measured in borate buffer containing 0.05 mol/L NaCl, indicated that in comparison to the pure AZ31 alloy and an in water ultrasonic treated sample, the sample ultrasonically treated in 0.5 M cerium nitrate solution had a potential shift to a more anodic potential as well as a slight reduction of the current density. This reduction was not significant but led to the assumption that the cerium oxide layer will increase the

corrosion protection if it can be synthesized without the cracks seen in the SEM images in Figure 18. Figure 22 shows the current density – potential curves and in Table 2 the corresponding values for the potential and the current density are listed.

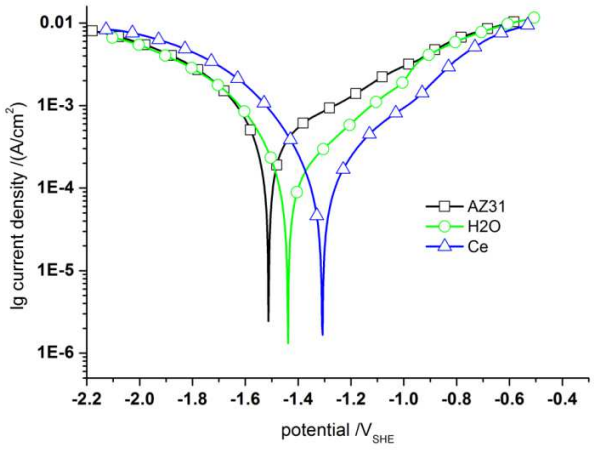

Figure 22: current density – potential curves of AZ31 after different surface treatments.

Table 2: current densities and corrosion potentials as a function of the different surface treatments.

Sample	i (µA/cm²)	E_{OCP} / $V_{(SHE)}$
AZ31 / as-cleaned	22.3	-1.51
AZ31 / US H_2O	12.1	-1.44
AZ31 / US $Ce(NO_3)_3$	9.8	-1.31

The as-cleaned sample showed a mixed potential according to the alloying elements Al and Zn of -1.5 V_{SHE}. After ultrasonic treatment in water the potential shifted to a slightly more anodic value and the current density decreased, indicating that a passive MgO layer, partially sealed by aluminum and zinc oxides and hydroxides, like described by Song and Atrens [9], arose. Ultrasonic treatment in cerium nitrate solution led to a further shift to a more anodic

potential and a slight decrease of the current density, indicating that the influence of the MgO layer still stems from the cracks but a promising effect was detected.

4.1.5. Electrochemical impedance spectroscopy (EIS)

The SEM images in Figure 18 showed that the synthesized oxide layers were traversed by cracks. To evaluate the corrosion protection ability, electrochemical impedance measurements in borate buffer containing 0.05 mol/L NaCl were done. The results are shown in Figure 23.

a) c)

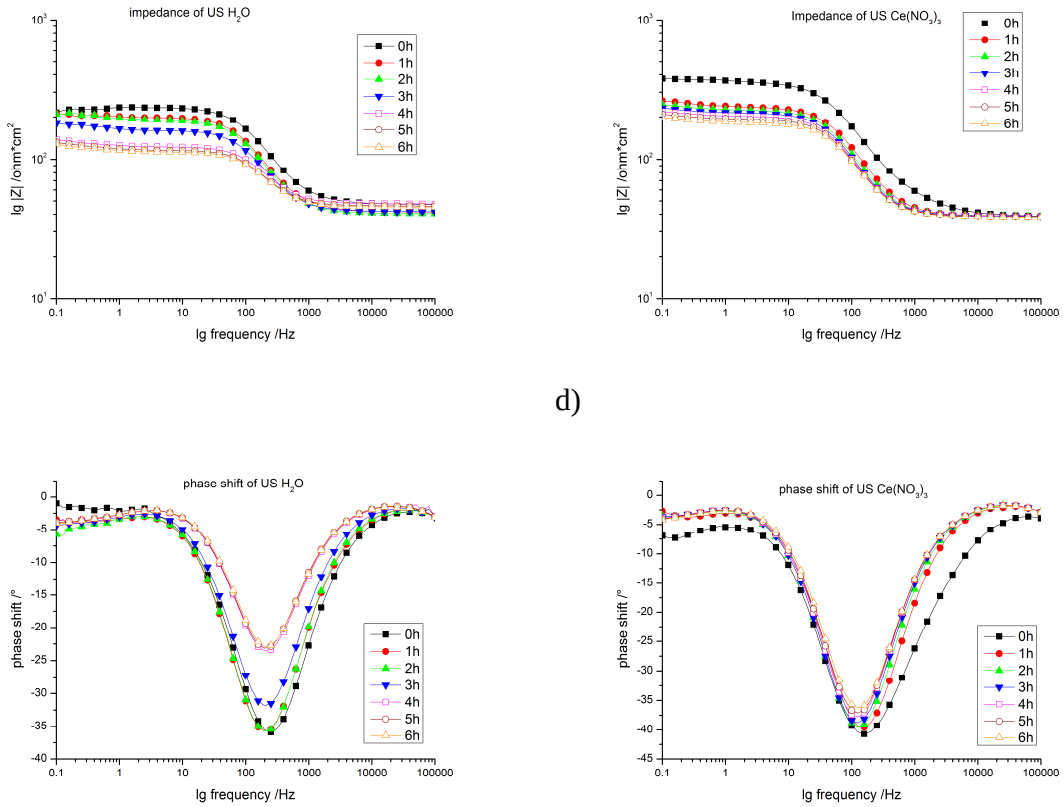

b) d)

Figure 23: EIS measurements of ultrasonically treated Mg AZ31 in pure water a) impedance, b) phase shift and ultrasonically treated Mg AZ31 in 0.5 M $Ce(NO_3)_3$ solution c) impedance, d) phase shift

Caused by the fast hydrogen evolution, the as-cleaned AZ31 sample was not measurable. As it can be seen in Figure 23 the impedance of the samples ultrasonically treated in cerium nitrate solution was as low as the samples ultrasonically treated in pure water. Caused by the cracks in the cerium oxide layer, the film was not isolating. Therefore the cerium nitrate treated sample had nearly the same poor corrosion protection ability than the magnesium oxide layers, synthesized in pure water. This also explains to non-significant decrease in the current density mentioned in Figure 22.

Taking the equivalent circuit shown in Figure 24 into account the electric properties of the synthesized layers can be described in more detail.

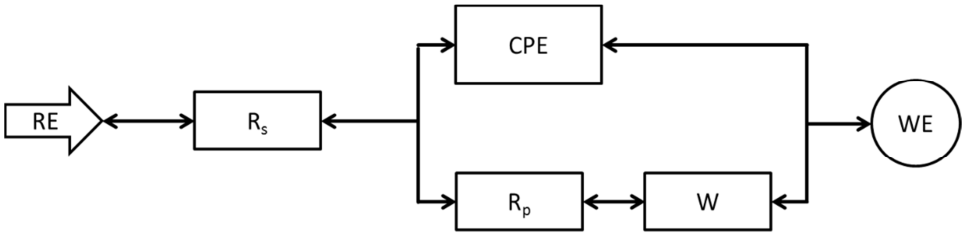

Figure 24: equivalent circuit for the ultrasonically treated magnesium alloy AZ31, with: RE: reference electrode, Rs: solution resistance, Rp: polarization resistance, CPE: constant phase element, W: Warburg impedance, WE: working electrode

For both layers the solution resistance decreased over time, indicating that the electrolyte diffused into the layers. The constant phase element described the double layer capacitance which was an imperfect capacitor since the phase shift was less than 90°. It did not change much for both layers, indicating that the surface and the current distribution did not change significantly during the experiment. The polarization resistance decreased for both layers. For the ultrasonic treatment in cerium nitrate the decrease was stronger than for the ultrasonic treatment in water. Finally the polarization resistance for the cerium oxide layer was still higher than for the magnesium oxide layer without cerium. The Warburg impedance decreased for the layer synthesized in water but increased for the layer synthesized in cerium nitrate. This behavior indicates that the cerium oxide layer hindered the diffusion of the reactants needed for the charge transfer but the dissolving magnesium oxide layer simplified the diffusion.

4.1.6. Adhesion studies (Peel test)

In addition to the corrosion protection and stability abilities of the synthesized layers the adhesion of a model epoxy adhesive was tested by use of a 90° peel test in high humidity to evaluate the possibility of coating for later technical applications. The results were normalized to the peel force on a freshly cleaned pure AZ31 surface and given in Table 3.

Table 3: Results of the 90° PEEL-force measurements of the polished and etched AZ31 surface in comparison to the ultrasonically treated samples

	AZ31 / as-cleaned	AZ31 / H_2O	AZ31 / $Ce(NO_3)_3$
Normalized Peel force / (N/mm)	1	1.6	5.6

The measurements of the peel force under 90° angle in high humidity indicated that the adhesion of the model epoxy adhesive, as equivalent for an adhesive or an organic coating was increased even by the use of ultrasonic treatment in pure water. It can be assumed that the porous, sponge-like layer, led to mechanical interlocking between the surface and the adhesive. The use of the cerium nitrate solution as solution for the ultrasonic treatment led to a further significant increase of the Peel force which may be caused by chemical bonds between the surface and the adhesive. A further explanation could be that, caused by the storage at high humidity the adhesion between the adhesive and the substrate was weaken more for the magnesium oxide layer than for the cerium oxide layer by water molecules. Thissen et al. [118] showed the strong adhesion of water molecules on a MgO single crystal and Varanasi et al. [20] showed the hydrophobicity of rare-earth oxide ceramics. For all samples de-adhesion of the adhesive took place instead of a cohesive break of the adhesive.

4.1.7. Conclusions

Concluding the results of the ultrasonic treatment of the magnesium alloy AZ31 it could be shown that by means of ultrasonically treatment an oxide layer consisting of magnesium

oxide and a thin cerium oxide layer could be deposited on the magnesium alloy AZ31. The ultrasonically treatment of AZ31 in pure water already led to a small decrease in the corrosion current density and an increase in the adhesion force of a model epoxy primer. This indicates an advantage in the corrosion stability by the growth of the magnesium oxide layer. The sponge-like layer with its significantly increased surface area led to a mechanical interlocking of the model epoxy adhesive, which was the reason for the increased adhesion force. The treatment with cerium nitrate enhanced both the corrosion stability, as the corrosion current density is slightly decreased further, and the adhesion. Either the increase of the adhesion force was caused by chemical bonds or by the hydrophobization of the surface, but this must be investigated in more detail. Figure 25 illustrates the model conception for the adhesion of the model epoxy adhesive on cleaned AZ31, AZ31 ultrasonically treated in water and AZ31 ultrasonically treated in cerium nitrate solution, like described before.

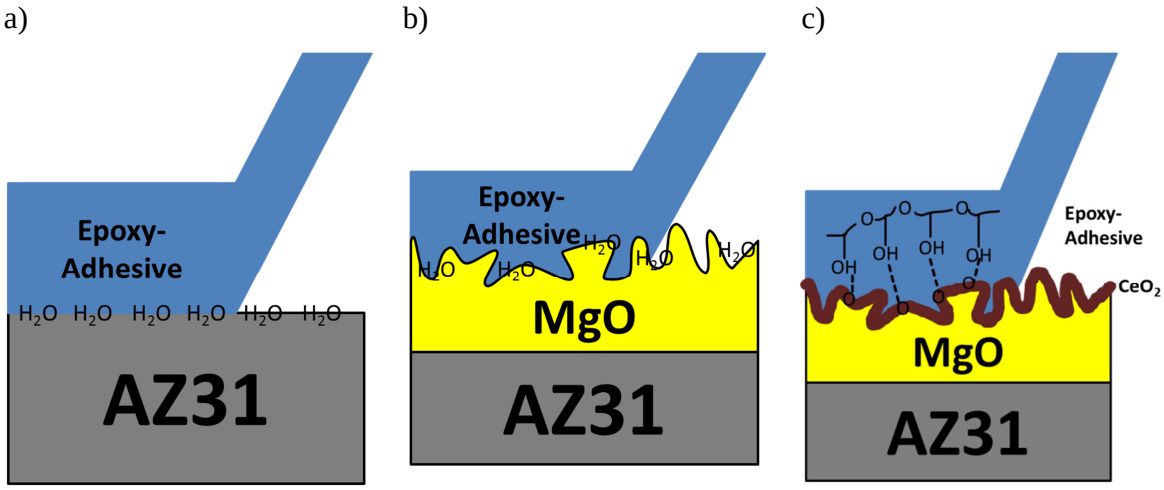

Figure 25: illustration of the adhesion of the model epoxy adhesive at a) clean AZ31, b) AZ31 after ultrasonic treatment in water (mechanical interlock) and c) AZ31 after ultrasonic treatment in cerium nitrate solution (mechanical interlock and chemical bonds)

EDX measurements of the cracks in the surface showed that no cerium could be detected in the cracks. The cracks revealed the magnesium oxide layer. Nevertheless the current density decreased slightly which indicates that the thin cerium oxide layer on top of the magnesium oxide layer may be able to enhance the corrosion protection.

The cracks, their formation and their influence on corrosion protection properties of ultrasonically build sponge-like oxide layers must be a point of further investigations.

4.2. Hot-forming of zinc alloy coated steel parts

To evaluate the influence of hot-forming to the alloy composition of zinc alloys suitable for the direct hot-forming process coated and annealed samples after shot blasting and after phosphating were investigated. For the determination of the cathodic corrosion protection ability the samples were compared to a pure zinc alloy, used for the indirect hot-forming process, as reference with known cathodic corrosion protection. Additionally welding points were investigated for the cathodic corrosion protection ability of the alloy coatings after welding as well as cut edges.

4.2.1. Investigations of the pure zinc coating reference

For the characterization of the surface of the shot blasted sample of the pure zinc coating reference, FE-SEM images in combination with EDX measurements were prepared and shown in Figure 26 and Table 4.

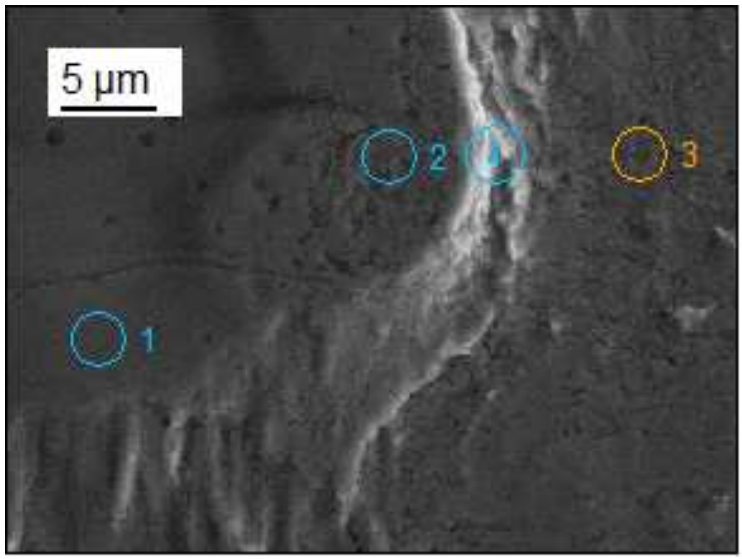

Figure 26: FE-SEM image of the shot blasted Z140 reference sample

Table 4: distribution of the relevant elements of the shot blasted Z140 reference sample in wt%

	C-K	*O-K*	*Al-K*	*Fe-K*	*Zn-K*
Z140-Ref(2)_pt1	1.24	0.87	0.47	0.76	94.58
Z140-Ref(2)_pt2	0.94	4.04	2.30	0.62	90.48
Z140-Ref(2)_pt3	1.00	3.67	2.15	0.78	91.83
Z140-Ref(2)_pt4	3.27	4.03	2.08	0.67	87.82

The EDX measurements indicated a dense zinc layer with less oxide. Close to the crater and inside the aluminum oxide layer, typical for hot-dip galvanized steel, could be detected as well as carbon species. Nevertheless the zinc layer still is very thick, as the measuring depth of EDX is at the µm scale.

To investigate how far the hot-forming process changes the composition of alloy coatings, the samples were coulometrically dissolved and the dissolved elements were detected in a down-stream ICP-OES. With this method the alloy coating composition and the breakdown of the protecting alloy coating could be detected. The results of the coulometry measurements with down-stream ICP-OES for the pure zinc coating reference sample is shown in Figure 27.

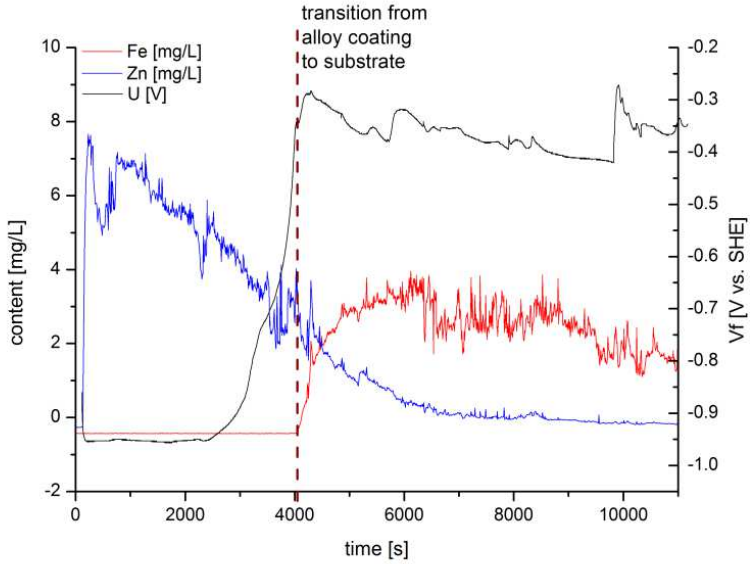

Figure 27: coulometric ICP-OES measurement of the reference sample Z140 with indicated transition from alloy coating dissolution to the dissolution of the substrate

For the not hot-formed pure zinc coating reference sample a long-time dissolution of zinc at a strongly cathodic potential could be detected. No dissolution of an alloy but a parallel dissolution of the zinc coating and the iron substrate could be seen at the breakthrough of the zinc coating. At this moment the potential increased to the potential of the Fe/Fe^{2+}-transition. A good cathodic corrosion protection was provided.

For the application in automotive sector it is of crucial importance that the cathodic corrosion protection is still provided after welding. To examine the potential distribution in the center, in the weld seam and in the surrounding matrix, the OCP in an aqueous 0.05 mol/L NaCl solution was measured as line scan over the welding spot by use of a scanning capillary cell with a local resolution of 1 mm for 5 min at each point.

In addition to the potential distributions the distributions of the alloy coating elements were detected by means of EDX measurements.

In Figure 28 the OCP line scan of the weld seam and a photography image with indicated measurement direction of the pure Z140 reference sample is shown. Accompanying a FE-SEM image with indicated spots for EDX measurement is placed under the line scan. The results of the EDX measurement are shown in Table 5.

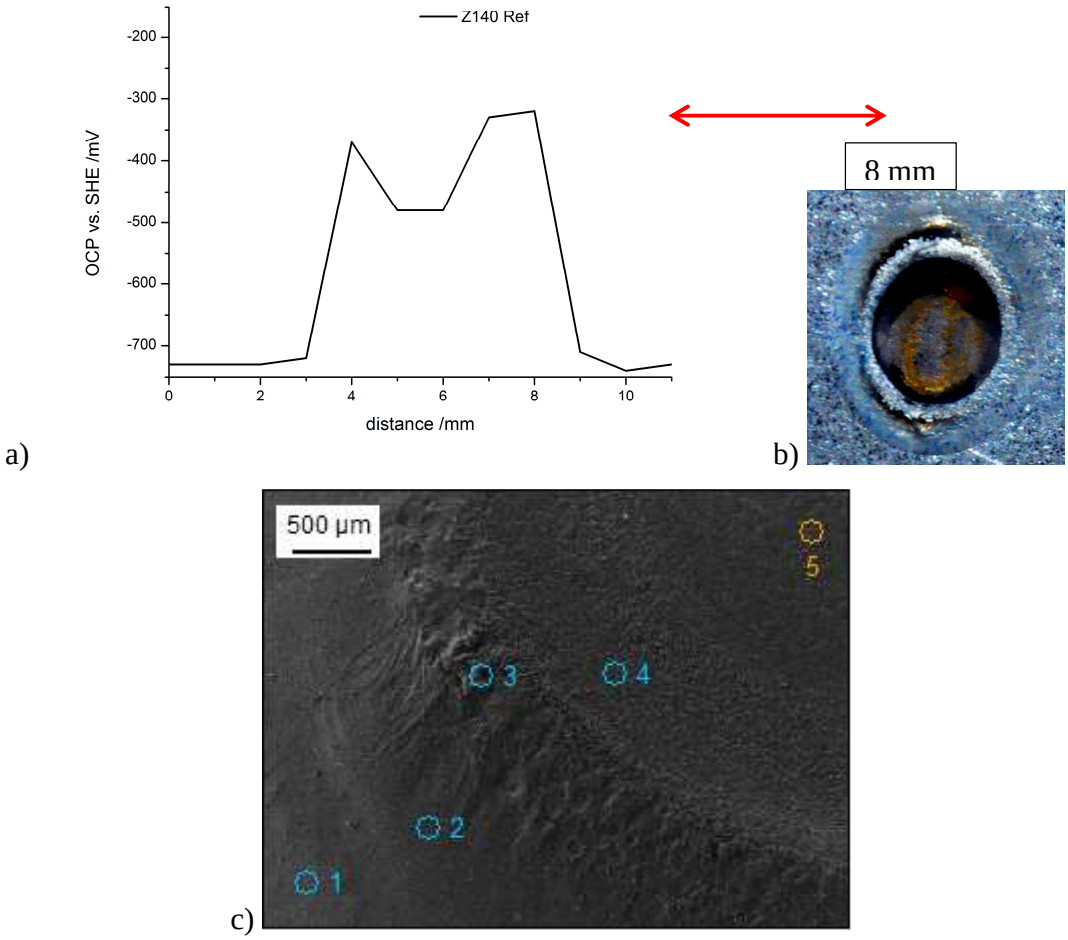

Figure 28: investigations of the welding point on the reference sample Z140 a) OCP line-scan, b) photography of welding point with illustrated line-scan and c) FE-SEM/EDX measurement of an exemplary part of the welding point

Table 5: distribution of the relevant elements of the welding point on the shot blasted Z140 reference sample in at%

	C-K	***O-K***	***Al-K***	***Fe-K***	***Zn-K***
Z140-Ref-(1)_pt1	9.62	10.26	2.24	0.59	67.86
Z140-Ref-(1)_pt2	5.75	19.09	2.29	1.01	57.66
Z140-Ref-(1)_pt3	5.99	13.14	2.39	1.82	76.39
Z140-Ref-(1)_pt4	3.70	22.28	1.57	39.55	31.02
Z140-Ref-(1)_pt5	6.60	5.71	9.27	66.05	7.89

The photography as well as the potential line-scan showed that in the center of the welding point the zinc was evaporated and iron oxide formation occurred. This result was validated by the EDX measurements. The amount of zinc decreased in the direction to the center of the welding point until less than 10 at%. At the weld seam the concentration of oxide was at a maximum, whereas the center of the welding point was outweighed by iron. Since the surrounding zinc matrix was about 0.4 V more cathodic than the weld seam, the assumption can be done that an anodic dissolution of the surrounding matrix led to a cathodic corrosion protection of the welding point.

In the direct hot-forming process the zinc alloy coated steel parts are cut before they are cleaned and used as safety-relevant parts in the automobile. Hence the cathodic corrosion protection of cut edges is of crucial importance likewise. Therefore cut edges were prepared in an embedding material, aged for one cycle in the climate change test, derusted and investigated via laser scanning confocal microscopy.

As reference to the zinc coated steel parts pure, non-coated 22MnB5 steel was investigated likewise to evaluate if the open steel at the cut edge was protected against corrosion by the coatings.

The laser scanning confocal microcopy images as well as the topography images in 3D and photography images of the non-coated steel and the Z140 reference sample are shown in Figure 29 and Figure 30.

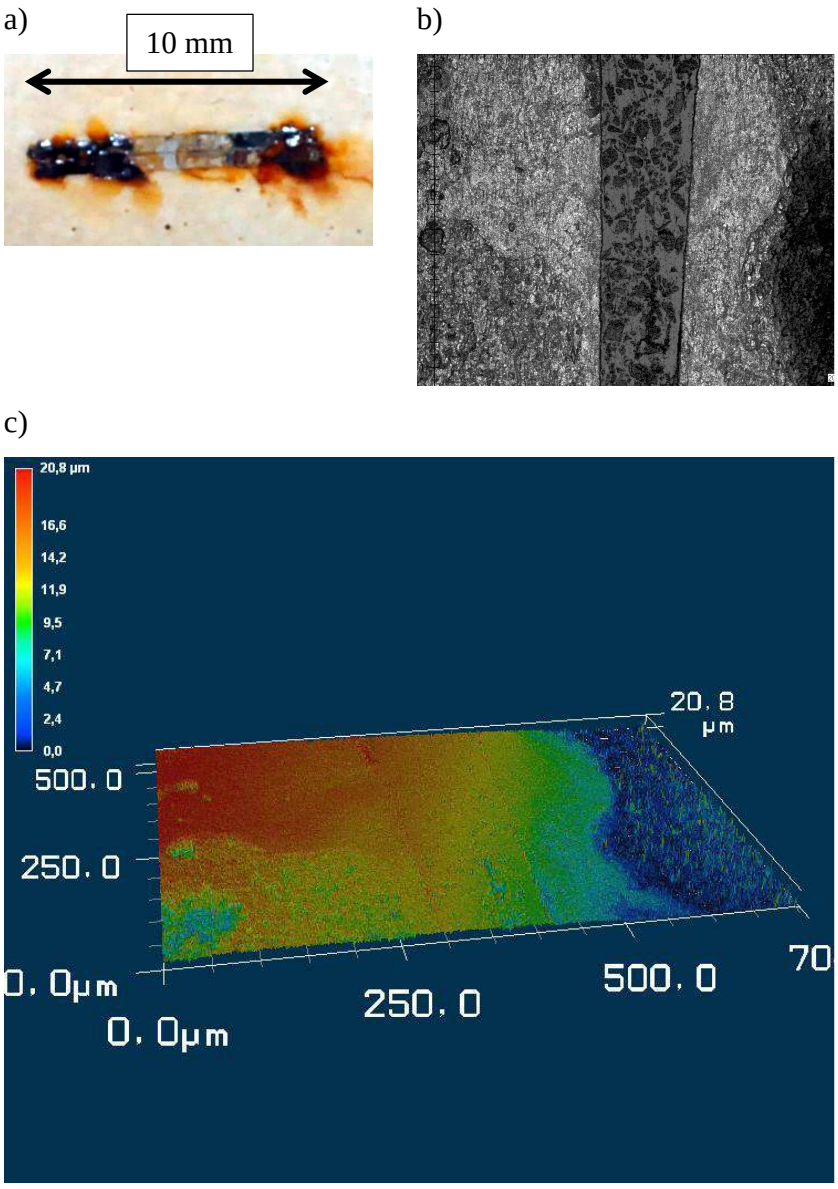

Figure 29: Laser scanning confocal microscopy investigations of embedded cut edges of pure not hot-formed 22MnB5 steel a) photography, b) laser microscopic image and c) 3D topography image

The pure not hot-formed 22MnB5 steel without any protecting zinc alloy coating showed the most intensive corrosive attack after the climate change test. After removing the corrosion

products it was clearly visible, that an inhomogeneous corrosive dissolution took place on the cut edge. The 3D topography investigation showed nearly no height differences across the sample, indicating that the dissolution took place across the whole sample as it could be expected for the unprotected steel.

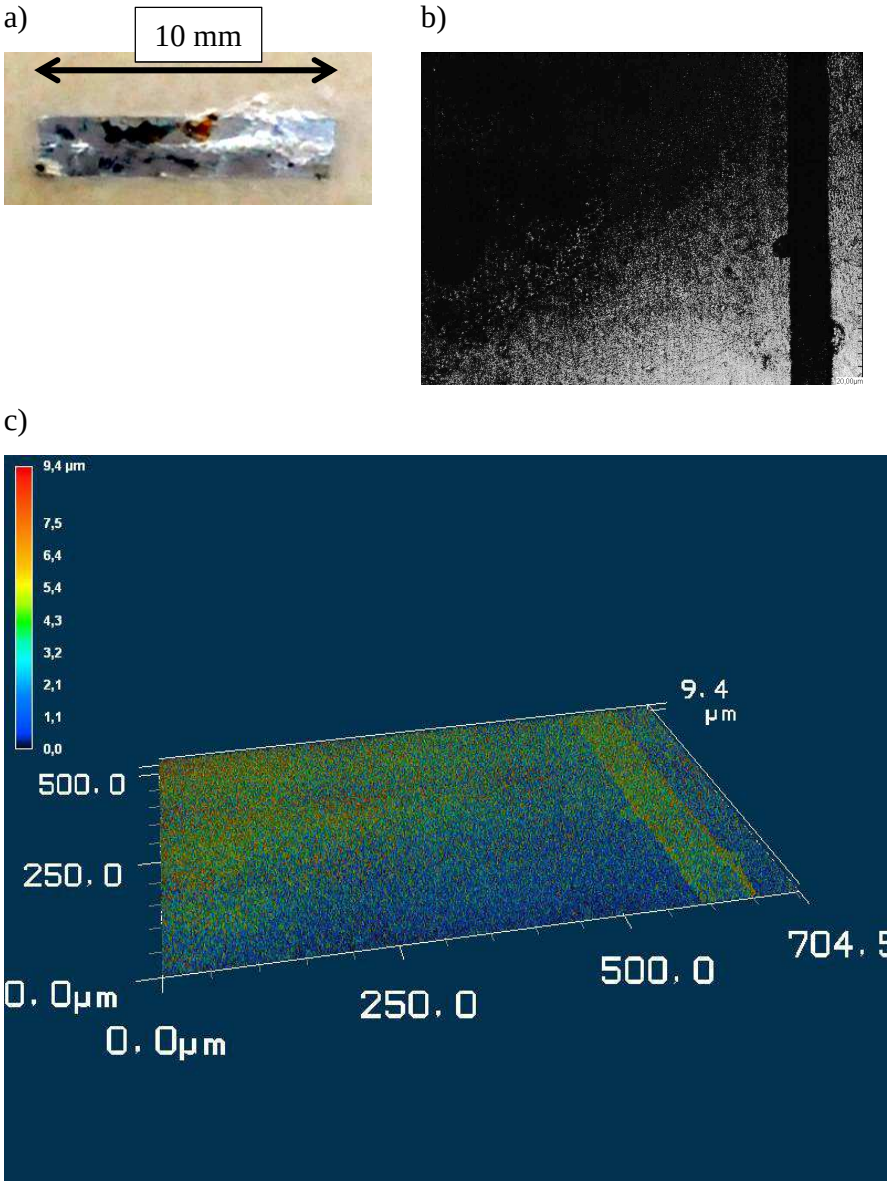

Figure 30: Laser scanning confocal microscopy investigations of embedded cut edges of not hot-formed pure zinc coated Z140 reference sample a) photography, b) laser microscopic image and c) 3D topography image

On the not hot-formed pure zinc coated reference sample after the climate change test, a significant amount of white rust was clearly visible. Removal of the corrosion products revealed the dissolution of the zinc coating as well in the contrast in the microscopic image as in the 3D topography image. The steel substrate was nearly not corroded as the 3D topography showed, indicating the proper corrosion protection ability of the zinc coating.

As it could be expected, the pure zinc coating 140 before heat treatment showed good, long-time cathodic corrosion protection. Although the zinc coating evaporated during welding, the welding point was protected by the surrounding matrix. Cut edges were covered by white rust which protected the underlying steel substrate against corrosion.

4.2.2. Investigations of the pure zinc coating after hot-forming

For the characterization of the surfaces of the shot blasted samples and phosphated samples of the pure zinc coating after hot-forming, FE-SEM images in combination with EDX measurements were prepared and shown for the different process conditions in Figure 31.

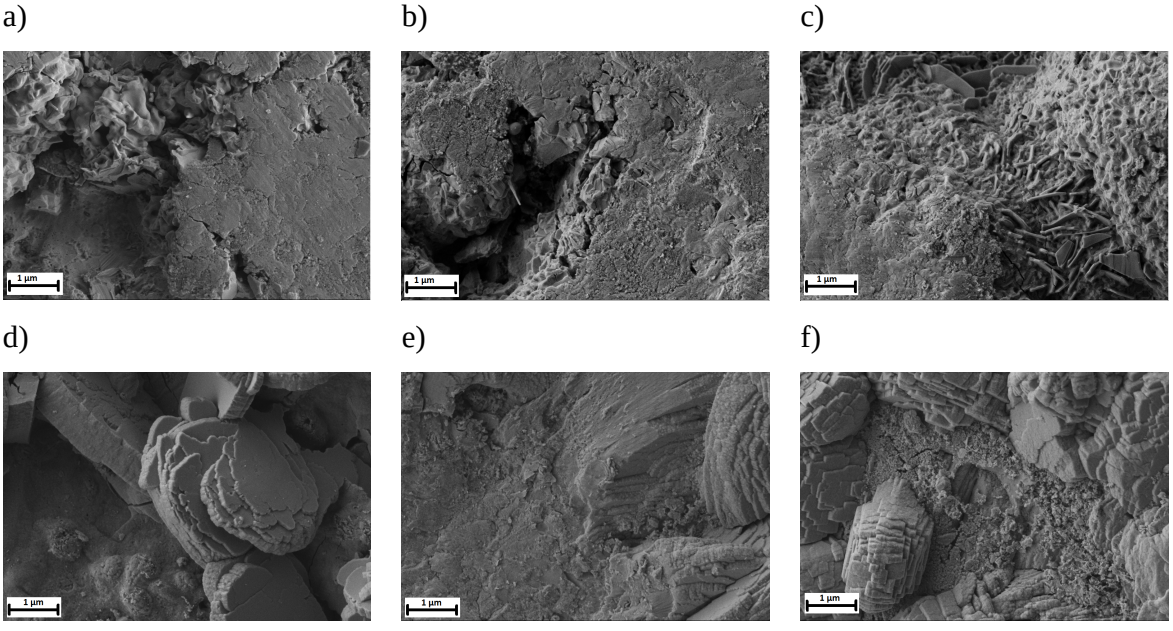

Figure 31: FE-SEM images a) – c) Z140 hot-formed at process conditions I, II & III and d) – f) phosphated Z140 hot-formed at process conditions I, II & III

More and more disc-like formations could be seen with increasing process time at elevated temperature. These disc-like formations indicated the formation of oxides. On the phosphated samples plates on the zinc alloy coatings showed the typical appearance of phosphate layers. The heat-treatment which was done before phosphating the samples did not seem to have any influence on the appearance of the phosphate plates.

For the characterization of the element distribution on the shot-blasted and the element distribution and the crystal size of the phosphating on the phosphated Z140 samples, EDX mappings had been generated. Figure 32 – Figure 34 show the mappings of the shot blasted samples and Figure 35 – Figure 37 show the mappings of the phosphated samples.

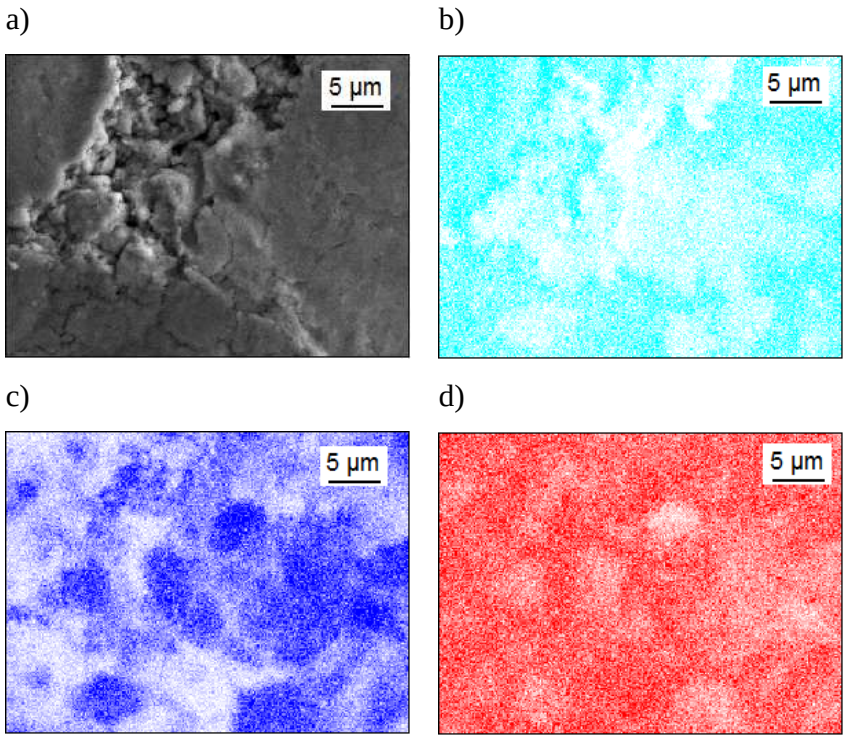

Figure 32: EDX Mappings of Z140 sample after process condition I a) FE-SEM image, b) O distribution, c) Fe distribution and d) Zn distribution

The zinc coating was homogenously distributed over the surface. On the spots where the iron content was increased, the zinc content was decreased slightly as well as the oxygen content. This indicates on one hand that an alloying of iron into the zinc coating layer occurred and on the other hand that the iron substrate was protected by the zinc coating, which was transferred into its oxygen species.

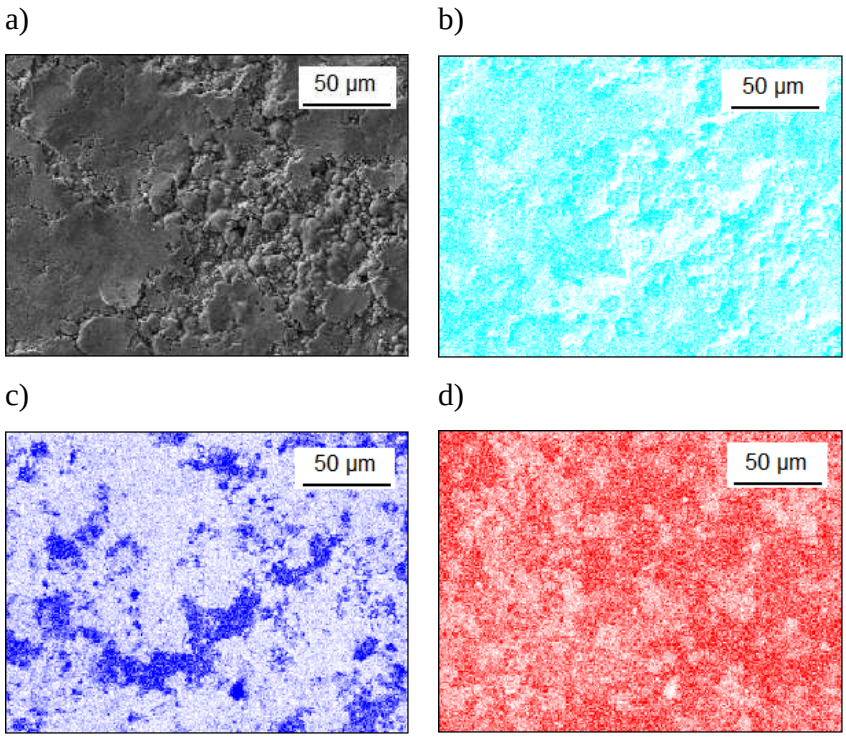

Figure 33: EDX Mappings of Z140 sample after process condition II a) FE-SEM image, b) O distribution, c) Fe distribution and d) Zn distribution

After process condition II the distribution and the contents of the elements was quite similar to that after process condition I. The zinc alloy still protected the iron substrate as its oxide species were built. But the iron contents, presumably caused by the alloying of iron into the zinc coating due to the heat-treatment, were increased and more sharply distributed than after process condition I.

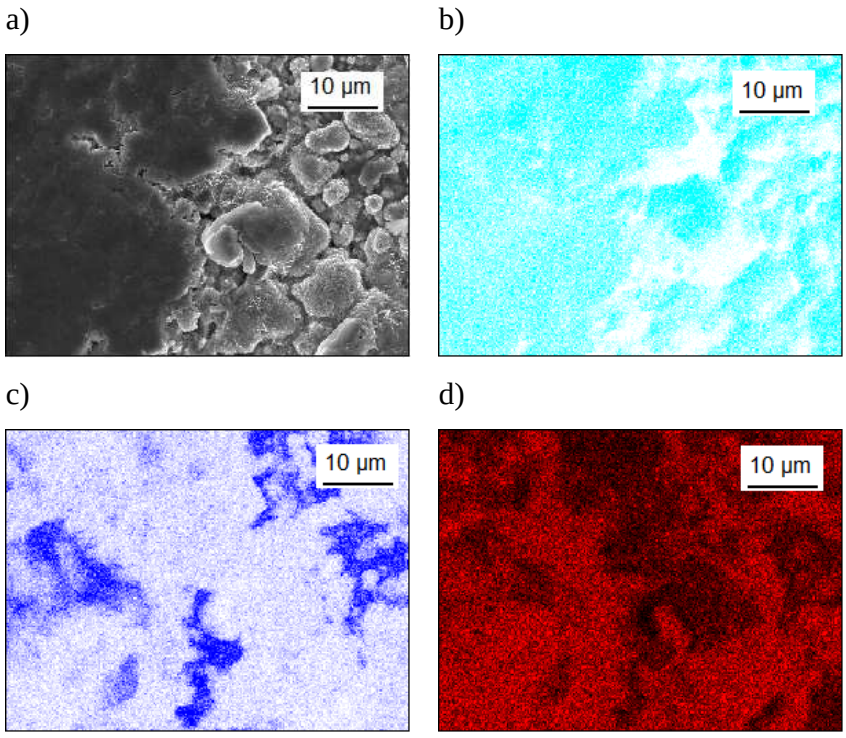

Figure 34: EDX Mappings of Z140 sample after process condition III a) FE-SEM image, b) O distribution, c) Fe distribution and d) Zn distribution

After process condition III the zinc content was decreased on the spots where the iron content was increased but the zinc layer seemed much less dense than after the other process conditions and the oxide distribution was predominantly increased at the zinc layer no more. This indicates that the cathodic corrosion protection was still provided but the alloyed iron in the zinc layer led to a decrease of the cathodic corrosion protection of the zinc after process condition III.

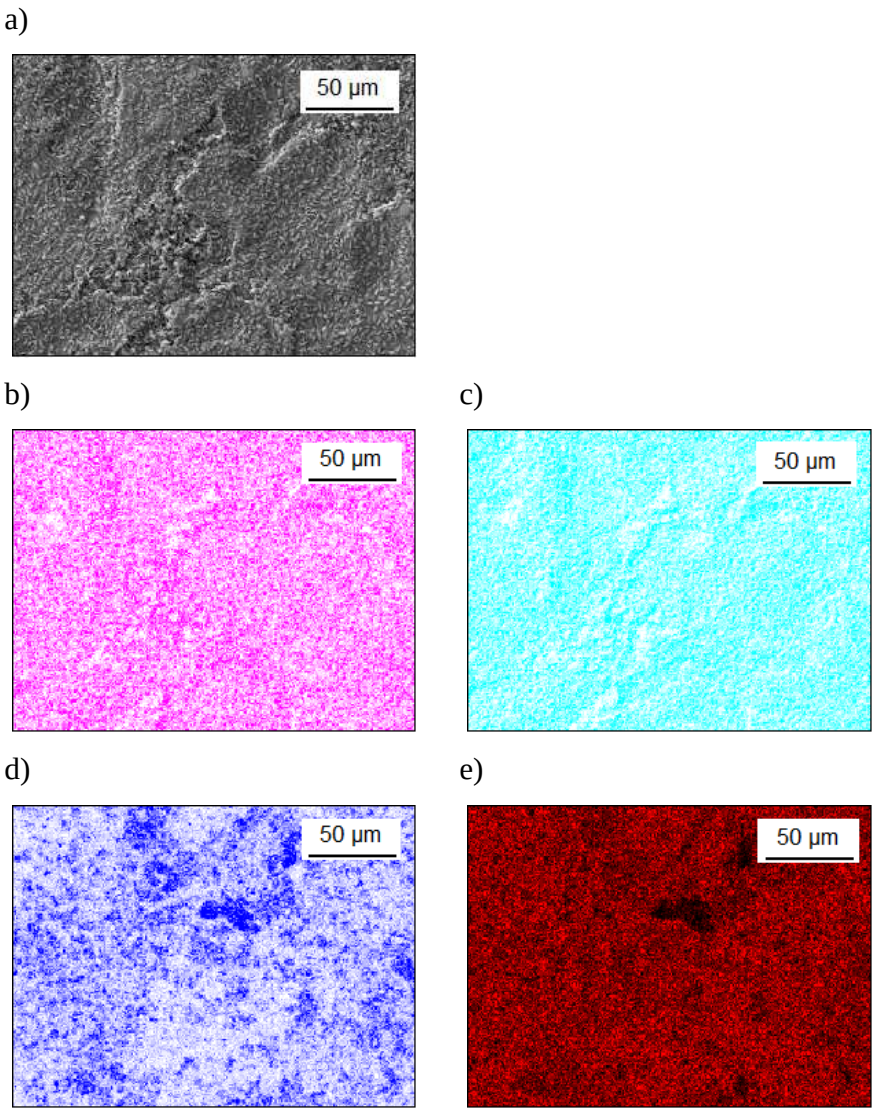

Figure 35: EDX Mappings of phosphated Z140 sample after process condition I a) FE-SEM image, b) P distribution, c) O distribution, d) Fe distribution and e) Zn distribution

The zinc alloy was covered by a dense and homogenous phosphate layer as it could be seen by the oxygen and phosphor distributions. This is in good agreement with the FE-SEM images on which phosphate plates were presumed. Typical for the EDX measurement the zinc layer as well as the iron substrate shone through, indicating that the phosphate layer is only few µm in thickness.

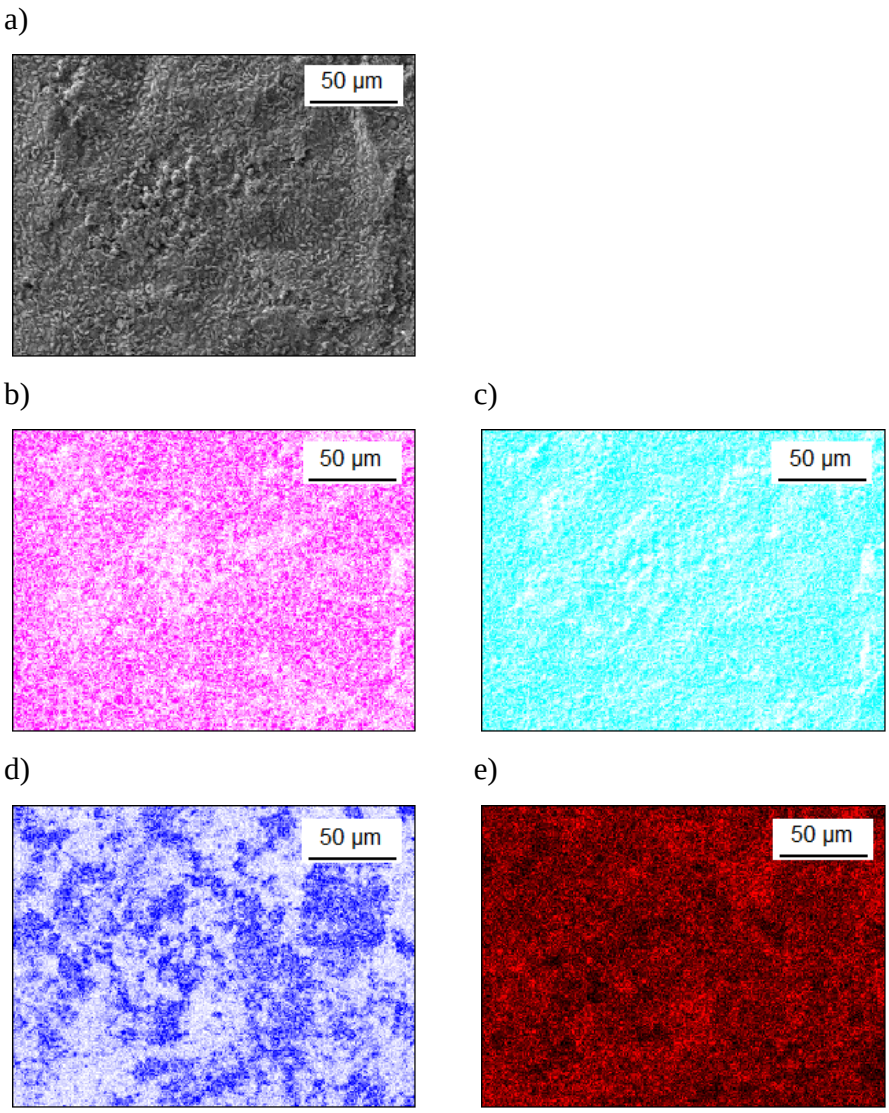

Figure 36: EDX Mappings of phosphated Z140 sample after process condition II a) FE-SEM image, b) P distribution, c) O distribution, d) Fe distribution and e) Zn distribution

The same behavior could be detected for the pure zinc coating after process condition II. Phosphor and oxygen covered the surface and the zinc coating as well as the iron substrate shone through, validating the FE-SEM images where phosphate plates were assumed to be placed on the surface. Since the distributions did not change much, the assumption substantiates that the heat-treatment before phosphating does not influence the phosphate layer.

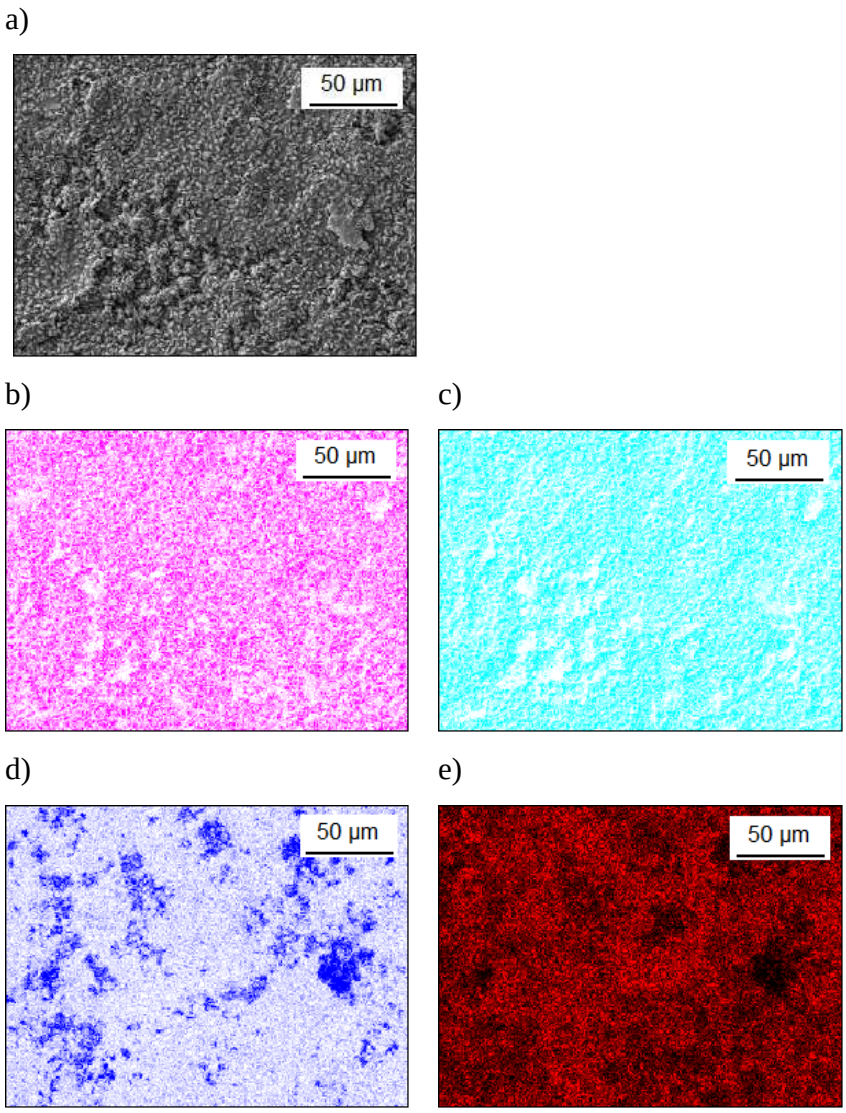

Figure 37: EDX Mappings of phosphated Z140 sample after process condition III a) FE-SEM image, b) P distribution, c) O distribution, d) Fe distribution and e) Zn distribution

To complete the investigations of the phosphating of the hot-formed pure zinc coating after process condition III the surface still was covered by a phosphate layer with apparent zinc coating and iron substrate without a significant change in the distribution.

For the investigation in how far the hot-forming process changes the alloy coatings composition the coulometric ICP-OES measurements were performed in an aqueous 0.1 mol/L KCl solution. The alloy coating composition and the breakdown of the protecting alloy

coating were detected. The results of the coulometry measurements with down-stream ICP-OES for the hot-formed zinc coating Z140 at the different process conditions are shown in Figure 38 – Figure 40.

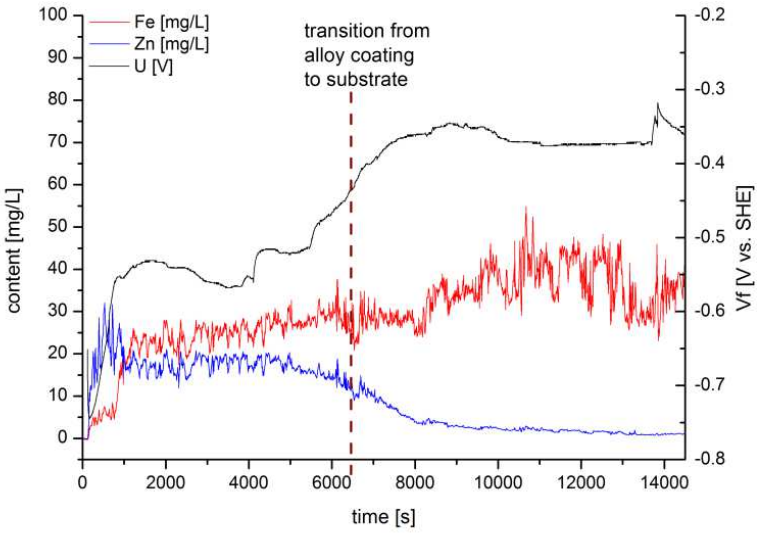

Figure 38: coulometric ICP-OES measurement of the hot-formed sample Z140 at process condition I with indicated transition from alloy coating dissolution to the dissolution of the substrate

An initial dissolution of zinc at the Zn/Zn^{2+} transition potential was followed by the dissolution of a Zn/Fe alloy at a mixed potential of -0.54 V(SHE) until the alloy broke through and the dissolution of the substrate occurred at the Fe/Fe^{2+} transition potential. The cathodic corrosion protection was provided during the alloy dissolution. The early detection of iron substantiates the assumption that iron diffuses into the zinc coating.

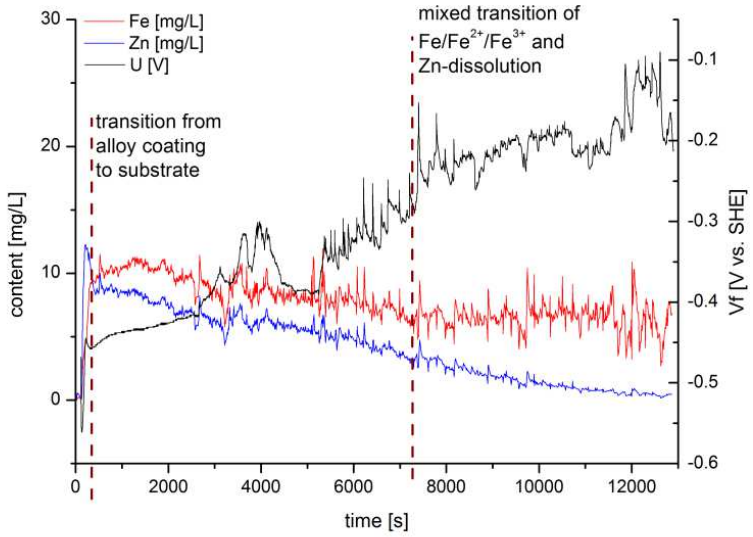

Figure 39: coulometric ICP-OES measurement of the hot-formed sample Z140 at process condition II with indicated transition from alloy coating dissolution to the dissolution of the substrate and the redox-reaction mixed with the dissolution of the alloy coating residue and the substrate

The dissolution of the Zn/Fe alloy indicated by the combination of the dissolved elements and the mixed potential at -0.54 V(SHE) started almost immediately. At the breakthrough of the alloy the potential increased to a mixed potential of $Fe/Fe^{2+}/Fe^{3+}$ dissolution. It can be assumed that the cathodic corrosion protection was limited at this sample as the potential increased all over the measurement time while the zinc dissolution decreased constantly. The appearance of Fe^{3+} species showed that the corrosion protection was not sufficient on this sample.

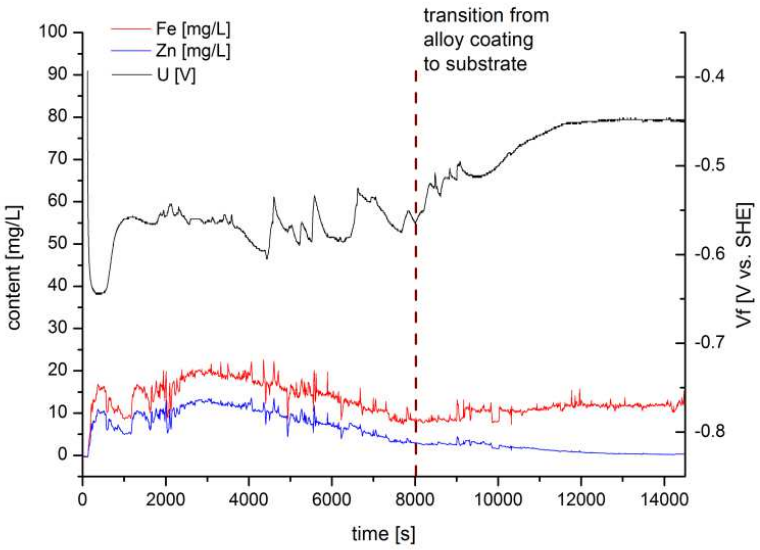

Figure 40: coulometric ICP-OES measurement of the hot-formed sample Z140 at process condition III with indicated transition from alloy coating dissolution to the dissolution of the substrate

An immediate dissolution of the Zn/Fe alloy at a potential of about -0.55 V(SHE) was followed by the dissolution of the substrate after the breakthrough of the alloy. The potential of -0.45 V(SHE) indicated the Fe/Fe^{2+} dissolution. The cathodic corrosion protection was provided by the zinc coating but a further alloying of iron into the zinc coating decreased the corrosion protection ability of the zinc.

To examine the potential distribution in the center, in the weld seam and in the surrounding matrix of a welding point, the OCP in an aqueous 0.05 mol/L NaCl solution was measured as line scan over the welding spot by use of a scanning capillary cell with a local resolution of 1 mm for 5 min at each point.

In addition to the potential distributions, the distributions of the alloy coating elements were investigated by means of EDX measurements.

In Figure 41 – Figure 43 the OCP line scans of the weld seams and photography images with indicated measurement direction of the hot-formed Z140 sample for the different process conditions are shown. Accompanying FE-SEM images with indicated spots for EDX measurements are placed under each line scan. The results of the EDX measurements are shown in Table 6 – Table 8 under Figure 41 – Figure 43, respectively.

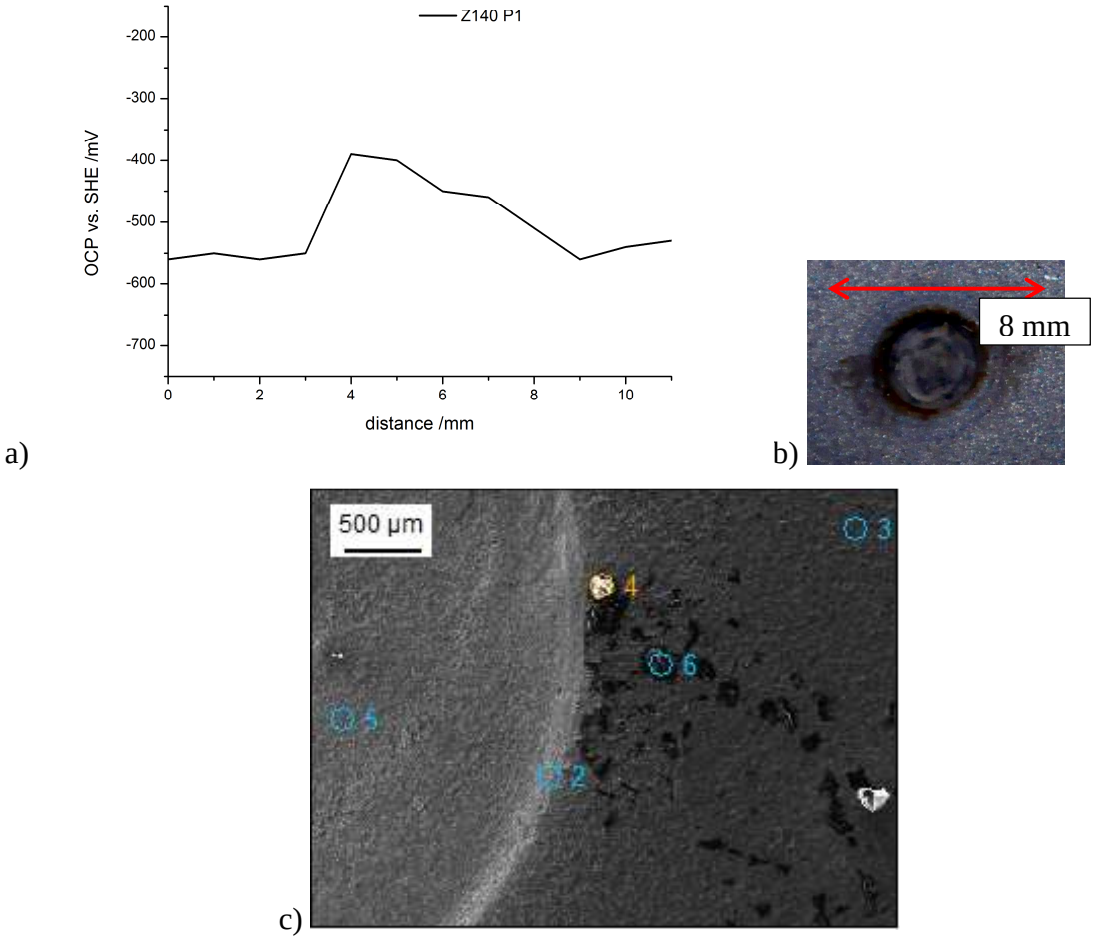

Figure 41: investigations of the welding point on the hot-formed pure zinc coating Z140 after process condition I a) OCP line-scan, b) photography of welding point with illustrated line-scan, c) FE-SEM/EDX measurement of an exemplary part of the welding point

Table 6: distribution of the relevant elements of the welding point on the hot-formed pure zinc coating Z140 after process condition I in at%

	C-K	***O-K***	***Al-K***	***Fe-K***	***Zn-K***
Z140-P1-(1)_pt2	4.85	47.24	0.92	15.43	28.82
Z140-P1-(1)_pt3	12.96	28.09	2.48	17.14	36.97
Z140-P1-(1)_pt4	37.12	40.50	16.88	0.81	3.69
Z140-P1-(1)_pt5	6.95	28.15	6.90	25.31	29.43
Z140-P1-(1)_pt6	96.87			1.39	1.42

In the optical images, nearly no iron oxides could be seen, which was validated by the EDX measurements where in the center and in the surrounding matrix the oxide content was decreased. At the weld seam the amount of oxygen was at nearly 50 at%. The potential line-scan showed that the potential of the welding point is close to the OCP of iron and the surrounding matrix is more anodic than the Zn/Zn^{2+} potential. This line-scan reflected the dissolution behavior evaluated by the coulometric ICP-OES measurements in Figure 38 indicating an alloying of iron into the zinc coating caused by the heat treatment. As the surrounding matrix was way more cathodic than the welding point a cathodic corrosion protection was provided.

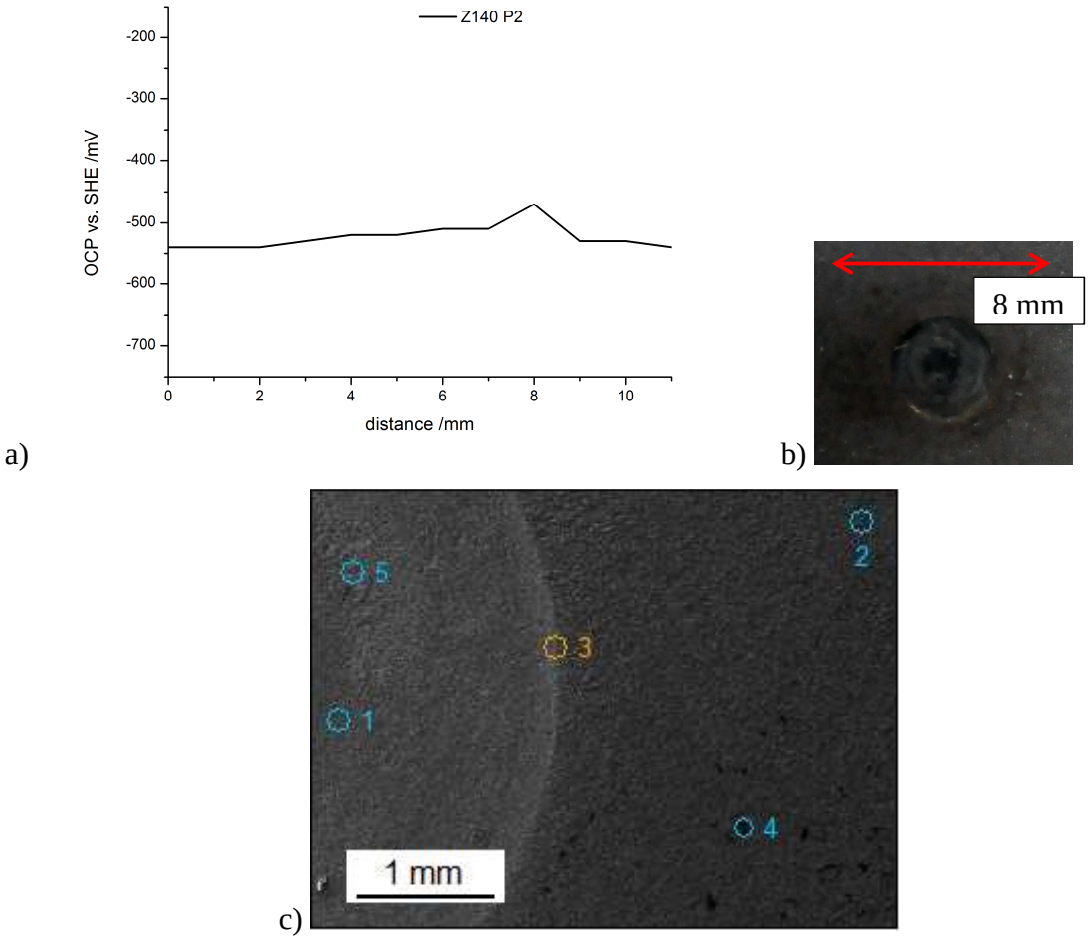

Figure 42: investigations of the welding point on the hot-formed pure zinc coating Z140 after process condition II a) OCP line-scan, b) photography of welding point with illustrated line-scan, c) FE-SEM/EDX measurement of an exemplary part of the welding point

Table 7: distribution of the relevant elements of the welding point on the hot-formed pure zinc coating Z140 after process condition II in at%

	C-K	***O-K***	***Al-K***	***Fe-K***	***Zn-K***
Z140-P2-(1)_pt1	11.00	34.64	3.68	17.66	25.82
Z140-P2-(1)_pt2	6.86	34.39	3.30	14.26	31.23
Z140-P2-(1)_pt3	5.37	44.92	1.20	6.30	36.20
Z140-P2-(1)_pt4	42.74	27.86	2.15	7.94	15.54
Z140-P2-(1)_pt5	8.26	25.61	3.41	31.66	23.90

After process condition II nearly no iron oxides could be seen in the center of the welding point. Additionally the EDX measurements showed that the zinc layer in the center was still intact. The distribution of oxygen was very homogeneous except for the weld seam where the amount of oxygen was increased. The potential line-scan was in good agreement with the coulometric ICP-OES measurement in Figure 39 as the potential all over the welding point and the matrix was more cathodic than the Fe/Fe^{2+} potential but more anodic than the Zn/Zn^{2+} potential. Hence the alloying of iron into the zinc coating increased and the welding did not influence the alloying any further.

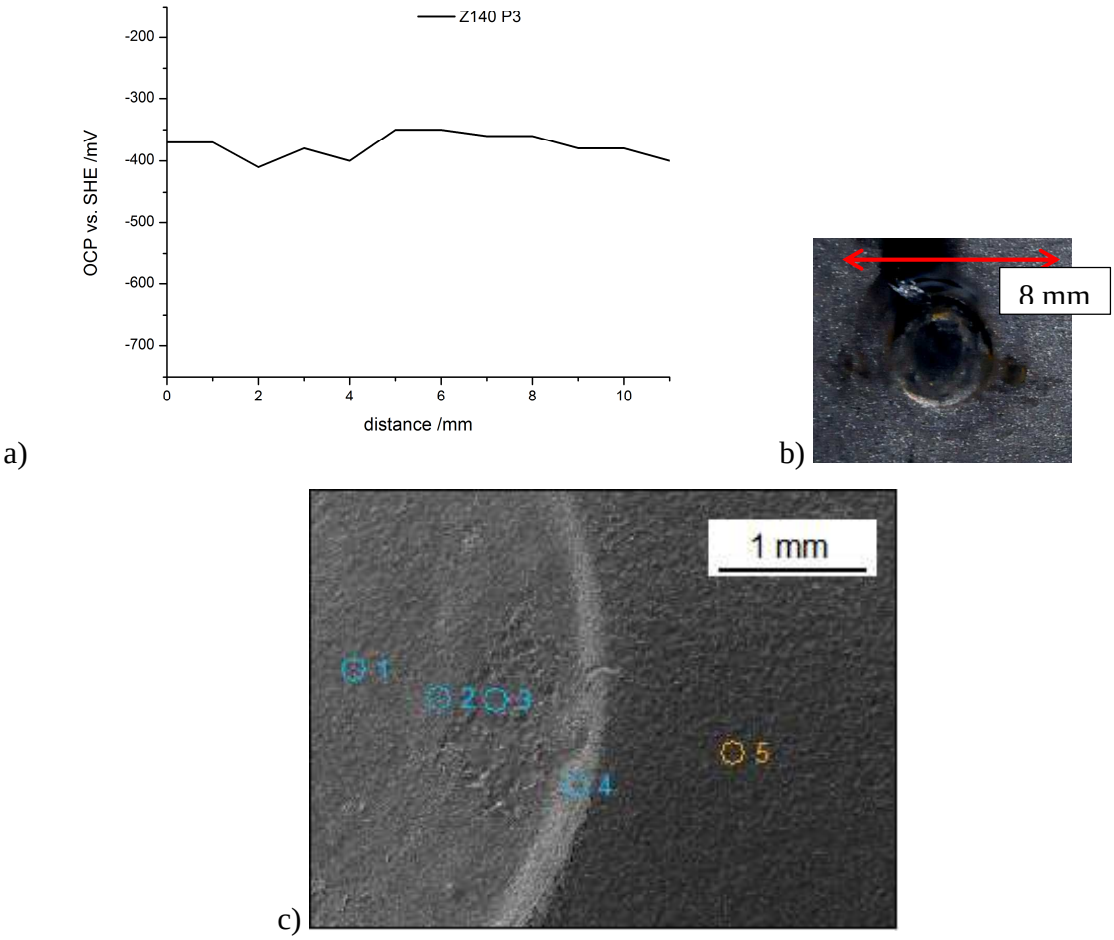

Figure 43: investigations of the welding point on the hot-formed pure zinc coating Z140 after process condition III a) OCP line-scan, b) photography of welding point with illustrated line-scan, c) FE-SEM/EDX measurement of an exemplary part of the welding point

Table 8: distribution of the relevant elements of the welding point on the hot-formed pure zinc coating Z140 after process condition III in at%

	C-K	***O-K***	***Al-K***	***Fe-K***	***Zn-K***
Z140-P3-(1)_pt1	10.04	33.90	2.82	19.61	24.89
Z140-P3-(1)_pt2	5.22	34.53	2.62	19.90	29.17
Z140-P3-(1)_pt3	9.22	33.30	1.33	21.80	23.27
Z140-P3-(1)_pt4	5.13	44.30	0.92	26.26	19.14
Z140-P3-(1)_pt5	12.56	38.56	1.79	16.16	23.96

The potential line-scan showed that after process condition III the center of the welding point and the surrounding matrix were more anodic than the Fe/Fe^{2+} potential and the weld seam was at the Fe/Fe^{2+} potential. Furthermore, according to the photography, the welding point looked thermally stressed. By the EDX measurements the increased iron content and decreased zinc content of the weld seam were approved. The alloying of iron into the zinc coating was increased and it can be assumed that the weld seam could partially dissolve anodically in favor of the center and the surrounding matrix of the welding point.

Cut edges were prepared in an embedding material, aged for one cycle in the climate change test, derusted and investigated via laser scanning confocal microscopy to ensure that the cathodic corrosion protection is provided after cutting the zinc coated steel sheets. Since the resulting part are used as safety-relevant parts in automotive industry the corrosion protection of cut edges is of high interest likewise as the surfaces.

The laser scanning confocal microcopy image as well as the topography image in 3D and a photography image of the hot-formed zinc coating Z140 is shown in Figure 44.

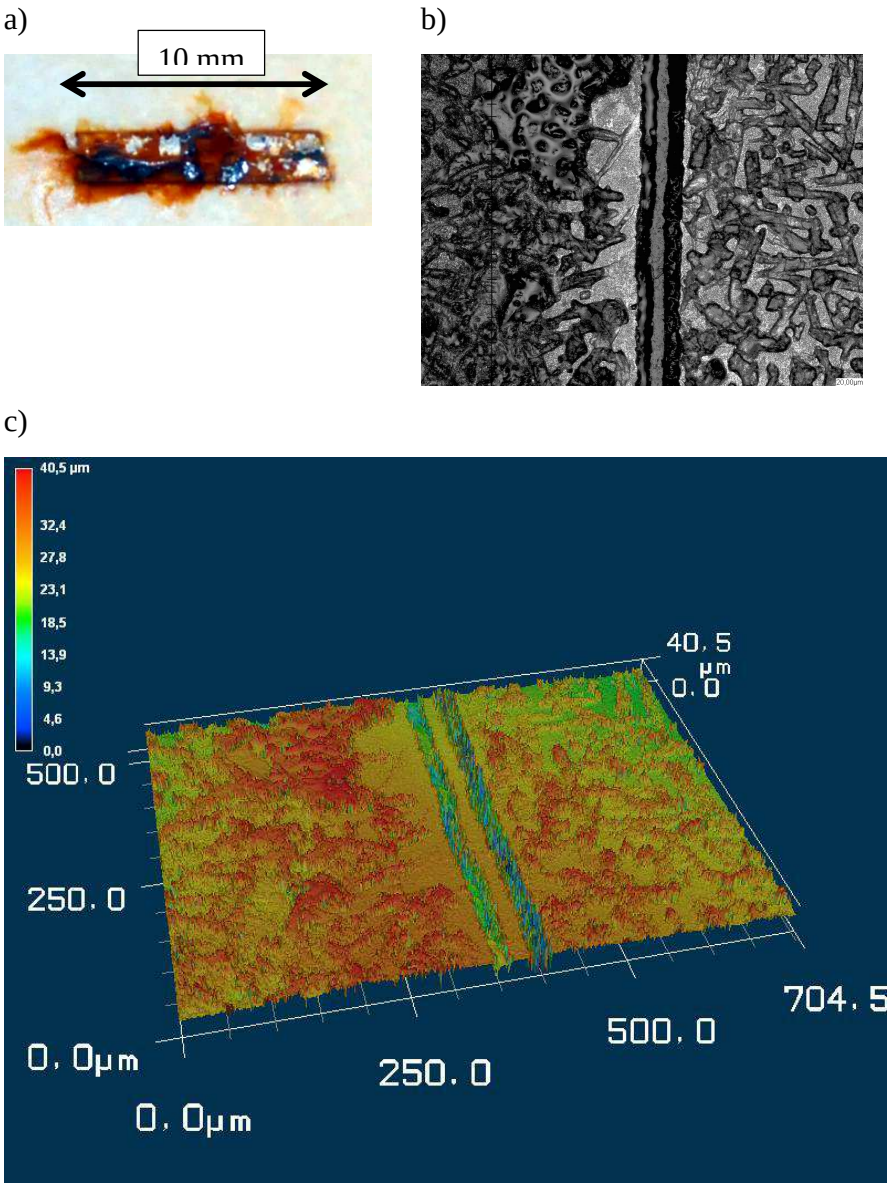

Figure 44: Laser scanning confocal microscopy investigations of embedded cut edges of hot-formed pure zinc alloy coated Z140 sample after process condition II a) photography, b) laser microscopic image and c) 3D topography image

An inhomogeneous rust formation could be seen on the hot-formed pure zinc coated steel sample. After removing the corrosion products in the microscopic image the dissolved zinc coating was marked by parallel black stripes. Between the stripes embedding material could be seen. The 3D topography investigation clearly showed that the zinc coating was dissolved in depth. Furthermore the steel substrate was corroded as well, as the topography was very

rough. These results are in very good agreement with the coulometric ICP-OES measurement in Figure 39 where the cathodic corrosion protection was not efficient as Fe^{3+} species could be detected.

4.2.3. Investigations of the iron containing zinc alloy coating after hot-forming

For the investigation of residual oxide scales and the surface appearance of the shot-blasted samples as well as for the characterization and the distribution of phosphates after phosphating FE-SEM images were performed. In Figure 45 the FE-SEM images of the iron containing zinc alloy coating Zn/Fe after shot-blasting and after phosphating are shown.

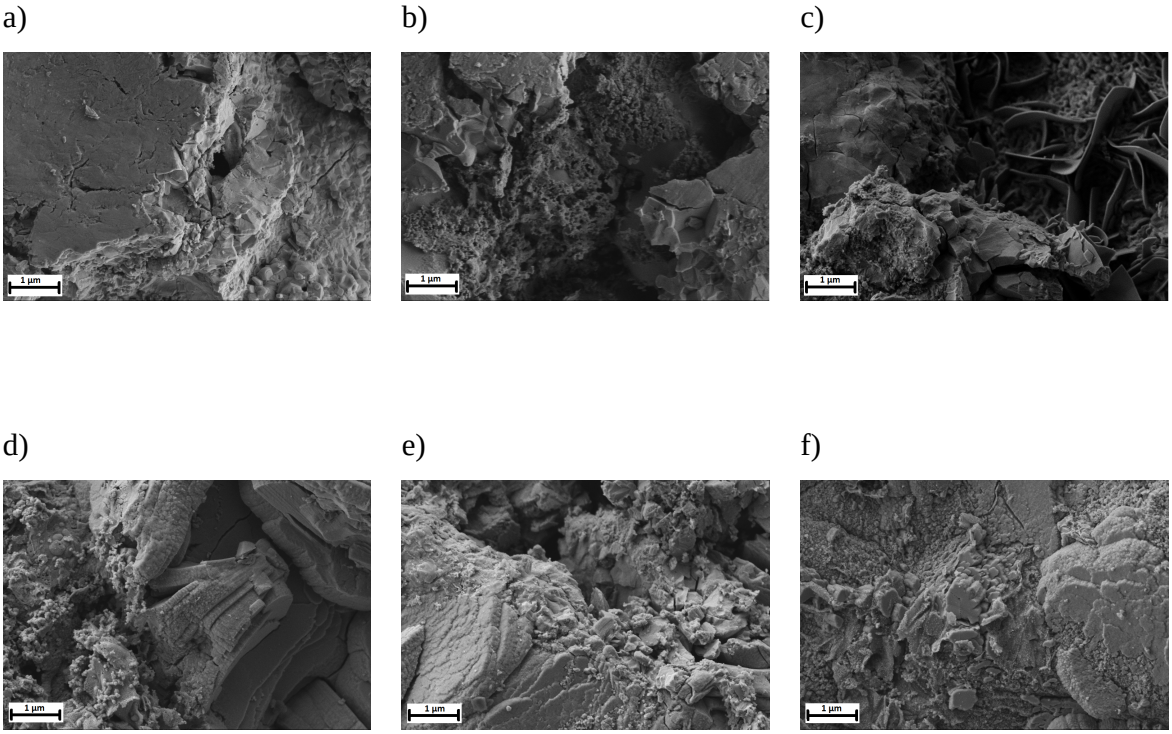

Figure 45: FE-SEM images a) – c) Zn/Fe hot-formed at process conditions I, II & III and d) – f) phosphated Zn/Fe hot-formed at process conditions I, II & III

After process condition III bridges were imaged on the shot-blasted samples. The increasing amount of disc-like formations indicated the formation of oxides. The phosphated samples with plate-like buildups on the zinc alloy coatings showed the typical appearance of porous phosphate layers. The appearance of the phosphate plates did not change by increasing heat-treatment which was done before phosphating, indicating that the heat-treatment did not have any influence on the phosphating.

Additionally to the FE-SEM images EDX mappings had been generated for the characterization of the element distribution on the shot-blasted and the element distribution and the crystal size of the phosphating on the phosphated iron containing zinc alloy coated Zn/Fe samples. Figure 46 – Figure 48 show the mappings of the shot blasted samples and Figure 49 – Figure 51 show the mappings of the phosphated samples.

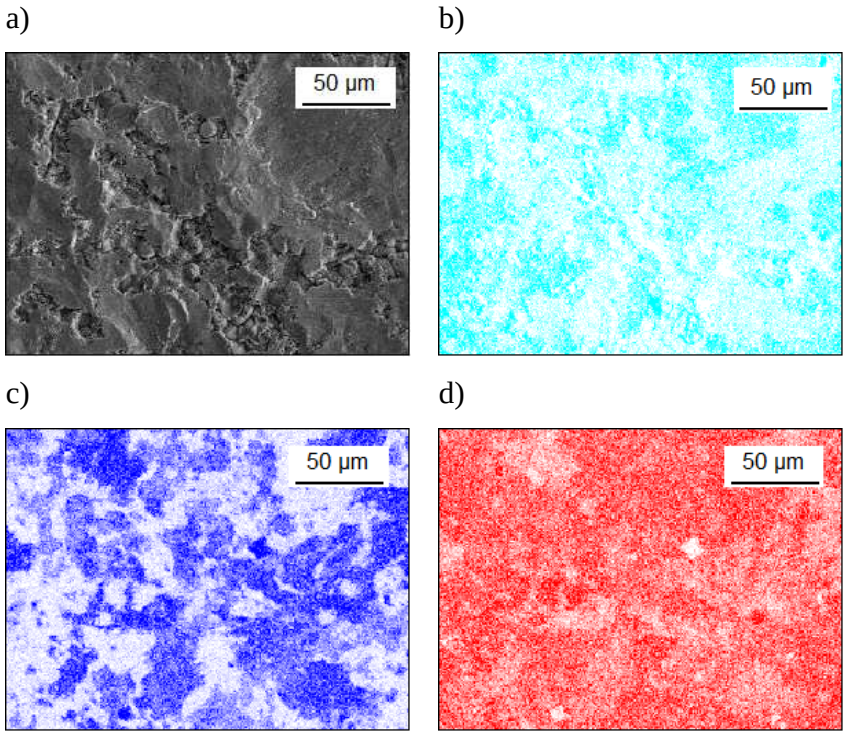

Figure 46: EDX Mappings of Zn/Fe sample after process condition I a) FE-SEM image, b) O distribution, c) Fe distribution and d) Zn distribution

As well as the pure zinc coating the iron containing zinc alloy coating showed a dense distribution of zinc with slightly decreased content where the iron content was increased. Similar to the Z140 sample after process condition II the iron distribution was sharply marked. The oxide content was preferentially increased where the zinc content was significantly higher than the iron content. Therefore the cathodic corrosion protection was provided.

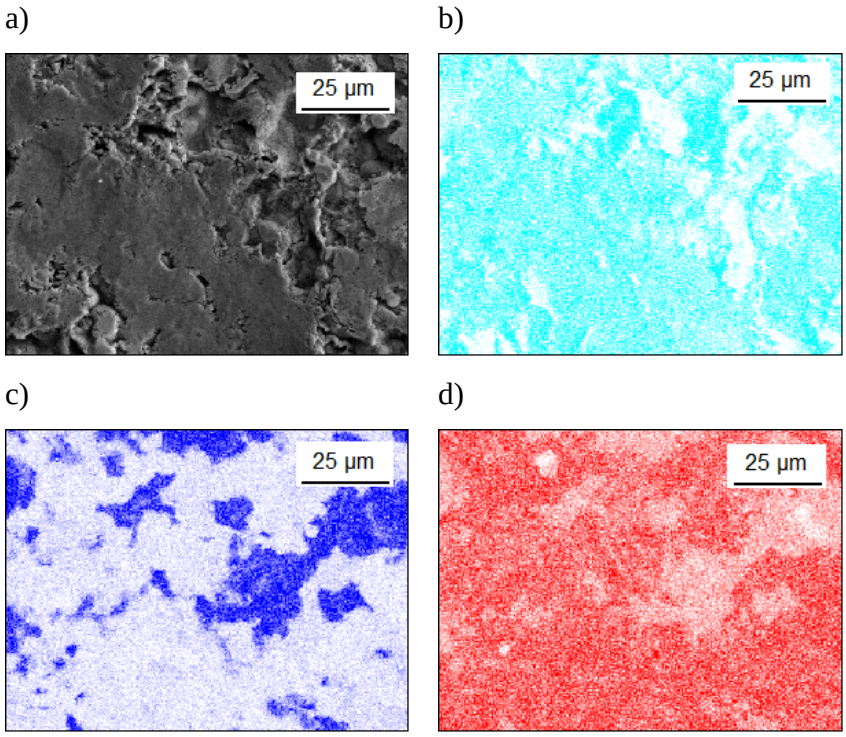

Figure 47: EDX Mappings of Zn/Fe sample after process condition II a) FE-SEM image, b) O distribution, c) Fe distribution and d) Zn distribution

The same distribution behavior for the iron and the zinc content as for process condition I was detected after process condition II. But the distribution of the oxygen content was partially increased for spots where the iron content was increased. This result indicates that the cathodic corrosion protection was still provided but was decreasing after process condition II yet.

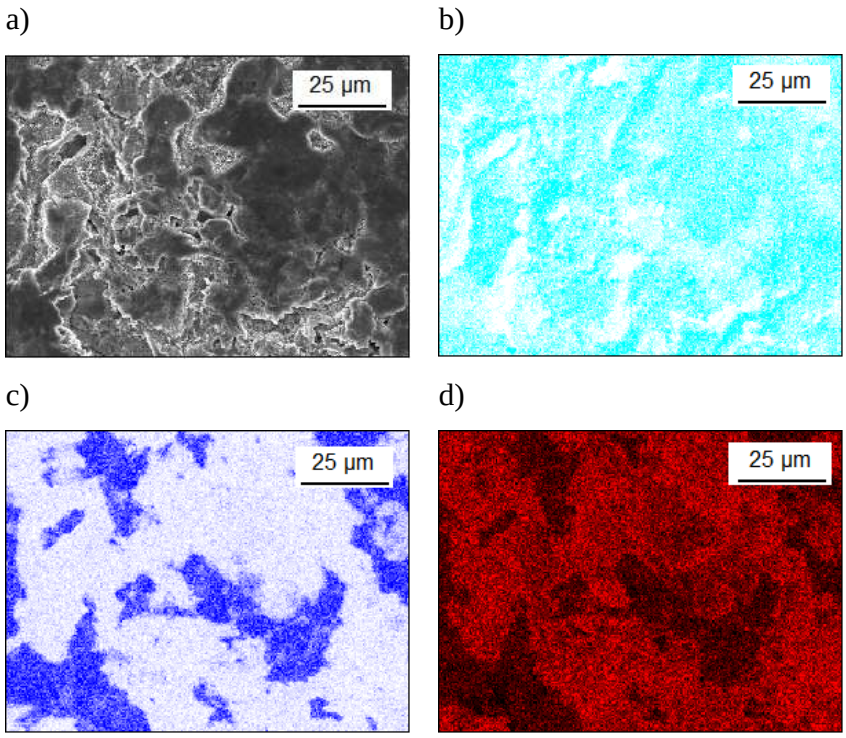

Figure 48: EDX Mappings of Zn/Fe sample after process condition III a) FE-SEM image, b) O distribution, c) Fe distribution and d) Zn distribution

After process condition III the EDX mappings still showed a similar distribution of the elements than for the process conditions of the iron containing zinc alloy coating before. The oxygen content was lower on the spots where the iron content was increased than on the spots where the zinc content was increased but the mappings indicated that iron oxides were formed. Furthermore the distribution of the zinc content was no more that homogenously than after the process conditions before.

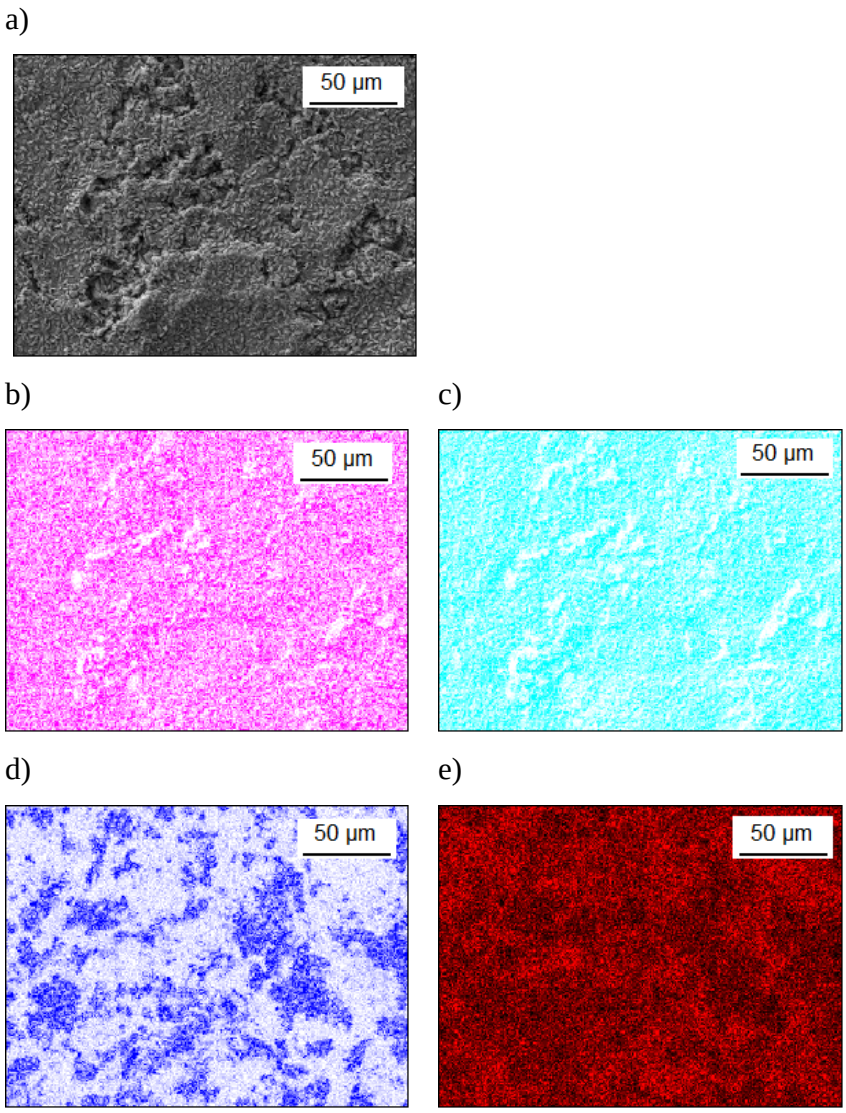

Figure 49: EDX Mappings of phosphated Zn/Fe alloy sample after process condition I a) FE-SEM image, b) P distribution, c) O distribution, d) Fe distribution and e) Zn distribution

For the iron containing zinc alloy coating the surface was homogeneously covered by a phosphate layer, as well as the hot-formed zinc coating Z140. The Zn/Fe alloy and presumable the iron substrate were shining through, indicating a thin phosphate layer. The content of iron was increased where the zinc content was slightly decreased whereas the oxygen distribution was homogeneous, maybe caused by iron isles in the alloy coating due to diffusion of iron from the substrate into the alloy coating.

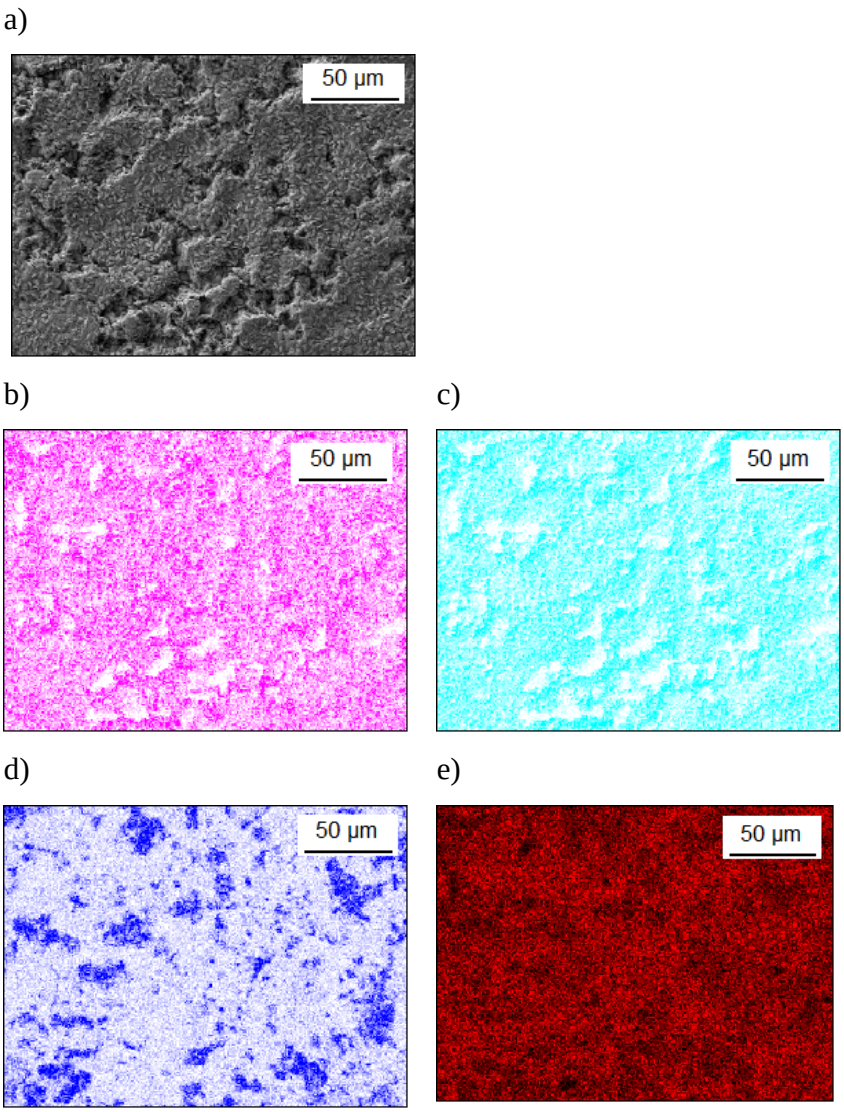

Figure 50: EDX Mappings of phosphated Zn/Fe alloy sample after process condition II a) FE-SEM image, b) P distribution, c) O distribution, d) Fe distribution and e) Zn distribution

A phosphate layer covered the surface, but was not as homogenous as on the systems discussed before. The Zn/Fe alloy content was increased which indicated that the phosphate layer was less dense.

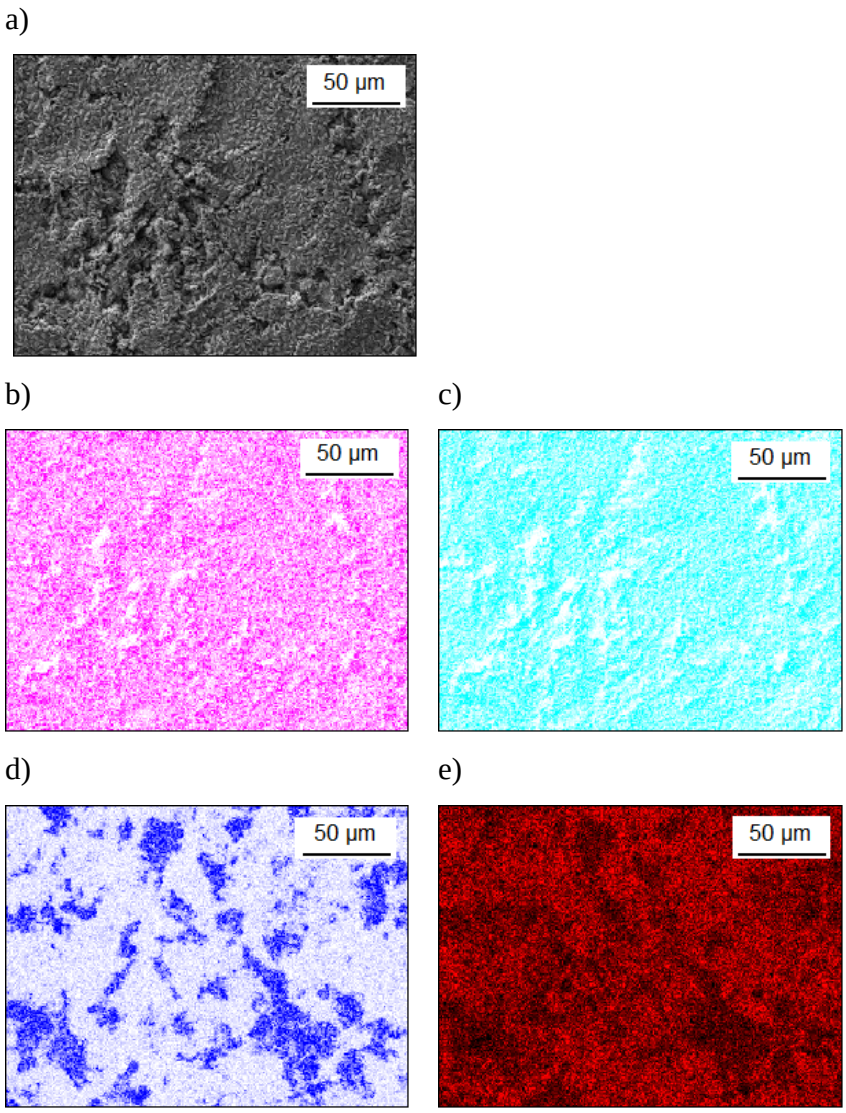

Figure 51: EDX Mappings of phosphated Zn/Fe alloy sample after process condition III a) FE-SEM image, b) P distribution, c) O distribution, d) Fe distribution and e) Zn distribution

After process condition III for the iron containing zinc alloy coating a similar behavior could be detected than after process condition II. The content of the Zn/Fe alloy coating was increased and the phosphate was less homogeneous indicating that the layer was less dense.

To evaluate in how far the hot-forming process changes the alloy coatings composition the coulometric ICP-OES measurements were performed in an aqueous 0.1 mol/L KCl solution. The alloy coating composition and the breakdown of the protecting alloy coating were detected. The results of the coulometry measurements with down-stream ICP-OES for the hot-formed, iron containing zinc alloy coating Zn/Fe at the different process conditions are shown in Figure 52 – Figure 54.

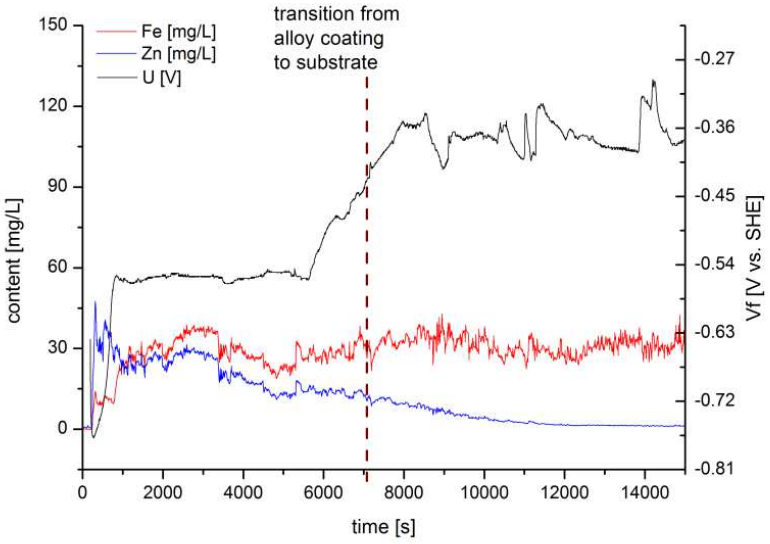

Figure 52: coulometric ICP-OES measurement of the hot-formed iron containing zinc alloy Zn/Fe at process condition I with indicated transition from alloy coating dissolution to the dissolution of the substrate

The iron containing zinc alloy coating showed the same behavior as the hot-formed pure zinc coating. An initial zinc dissolution at the Zn/Zn^{2+} potential was followed by the dissolution of the Zn/Fe alloy at a potential of -0.54 V(SHE) until the alloy broke through and the substrate dissolved at a potential of about -0.4 V(SHE). Therefore the cathodic corrosion protection was provided and a further evidence for the alloying of iron from the substrate into the zinc coating for the Z140 samples was given.

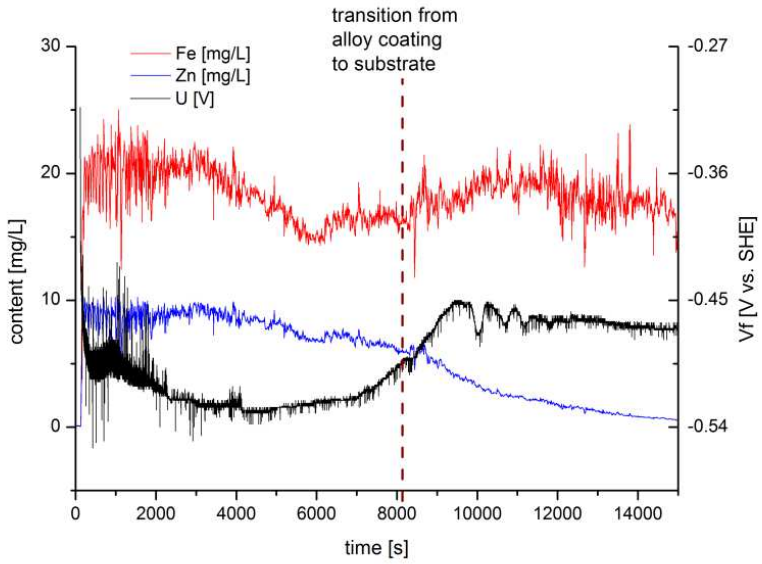

Figure 53: coulometric ICP-OES measurement of the hot-formed iron containing zinc alloy Zn/Fe at process condition II with indicated transition from alloy coating dissolution to the dissolution of the substrate

After process condition II the iron containing zinc alloy coated steel sample showed an immediate dissolution of the alloy at a potential of -0.54 V(SHE) followed by the dissolution of the substrate at a potential of about -0.42 V(SHE). The fluctuations in the potential as well as in the element dissolution indicate that the resistance of the sample changed during the measurement possibly caused by the buildup and dissolution of a passivating hydroxide layer.

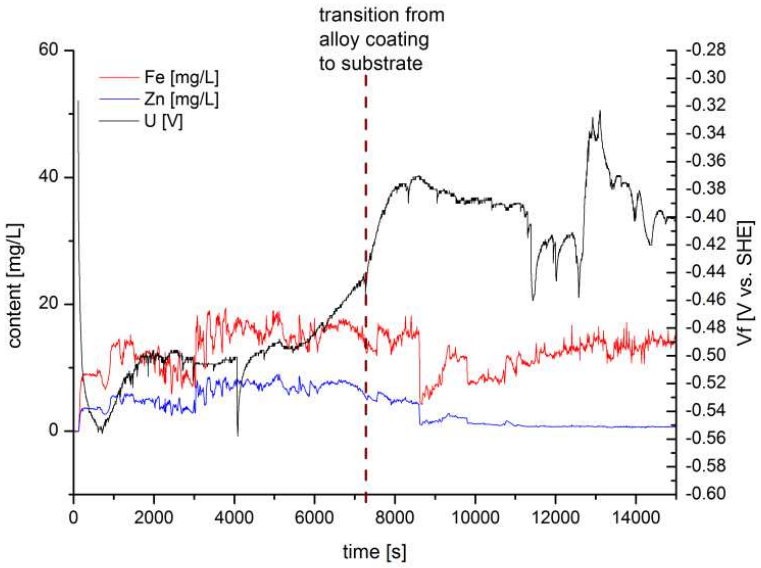

Figure 54: coulometric ICP-OES measurement of the hot-formed iron containing zinc alloy Zn/Fe at process condition III with indicated transition from alloy coating dissolution to the dissolution of the substrate

An immediate dissolution of the alloy at a potential of about -0.5 V(SHE) was followed by the dissolution of the substrate at a potential of about -0.4 V(SHE). The zinc dissolution ended abruptly as the potential increased. These results indicate that the cathodic corrosion protection was provided by the Zn/Fe alloy coating.

To examine the potential distribution in the center, in the weld seam and in the surrounding matrix of a welding point, the OCP in an aqueous 0.05 mol/L NaCl solution was measured as line scan over the welding spot by use of a scanning capillary cell with a local resolution of 1 mm for 5 min at each point. In addition to the potential distributions the distributions of the alloy coating elements were detected by means of EDX measurements.

In Figure 55 – Figure 57 the OCP line scans of the weld seams and photography images with indicated measurement direction of the iron containing Zn/Fe sample for the different process conditions are shown. Accompanying FE-SEM images with indicated spots for EDX

measurements are placed under each line scan. The results of the EDX measurements are shown in Table 9 – Table 11 under Figure 55 – Figure 57, respectively.

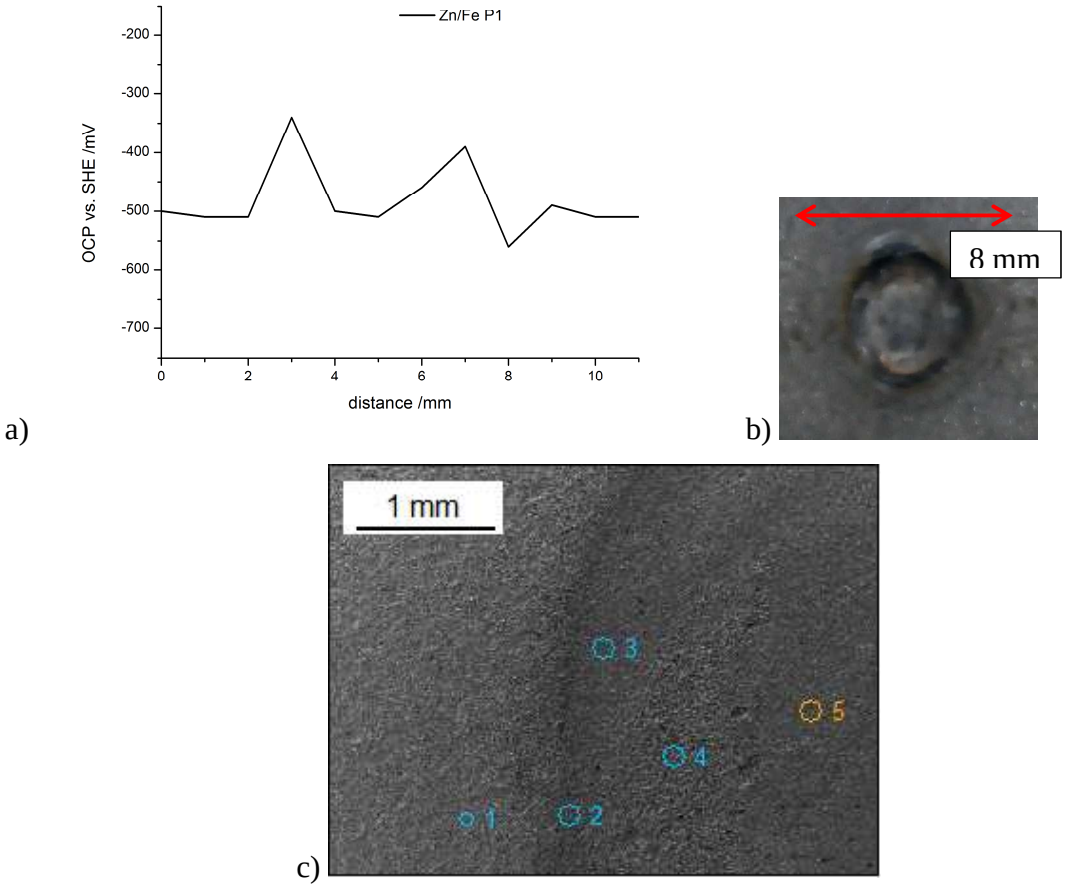

Figure 55: investigations of the welding point on the hot-formed iron containing zinc alloy coating Zn/Fe after process condition I a) OCP line-scan, b) photography of welding point with illustrated line-scan, c) FE-SEM/EDX measurement of an exemplary part of the welding point

Table 9: distribution of the relevant elements of the welding point on the hot-formed iron containing zinc alloy coating Zn/Fe after process condition I in at%

	C-K	***O-K***	***Al-K***	***Fe-K***	***Zn-K***
Zn/Fe-P1-(1)_pt1	6.18	45.93	0.77	7.34	32.46
Zn/Fe-P1-(1)_pt2	12.61	37.22	1.12	21.70	21.90
Zn/Fe-P1-(1)_pt3	12.12	32.81	2.30	8.61	39.77
Zn/Fe-P1-(1)_pt4	9.80	23.60	2.43	34.51	21.63
Zn/Fe-P1-(1)_pt5	9.44	28.79	2.58	13.96	36.30

For the iron containing zinc alloy coating no formation of iron oxides in the center of the welding point could be detected, neither by the photography nor by the EDX measurements. The potential line-scan showed that the center of the welding point was at the same potential than the surrounding matrix. The weld seam was more anodic than the center and the surrounding matrix indicating that the cathodic corrosion protection of the weld seam was provided.

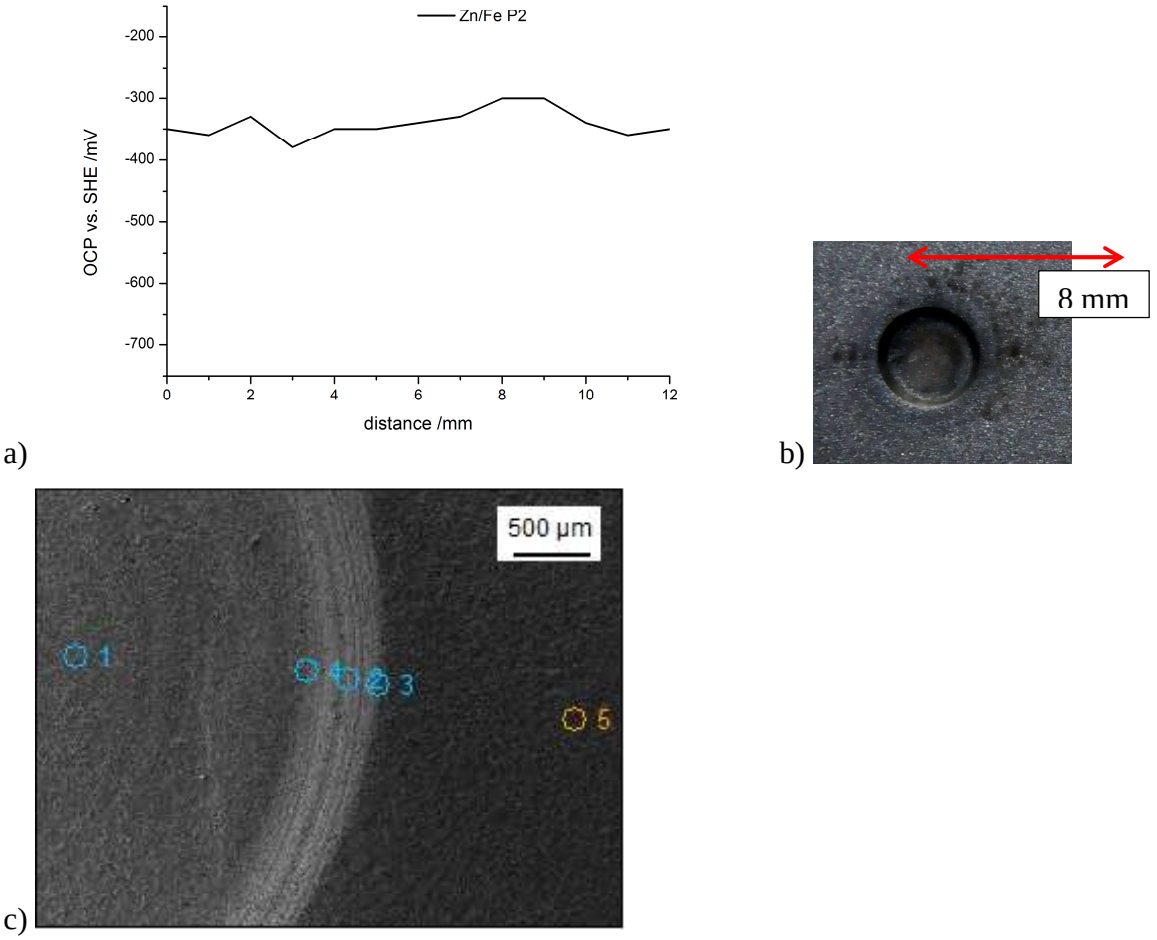

Figure 56: investigations of the welding point on the hot-formed iron containing zinc alloy coating Zn/Fe after process condition II a) OCP line-scan, b) photography of welding point with illustrated line-scan, c) FE-SEM/EDX measurement of an exemplary part of the welding point

Table 10: distribution of the relevant elements of the welding point on the hot-formed iron containing zinc alloy coating Zn/Fe after process condition II in at%

	C-K	***O-K***	***Al-K***	***Fe-K***	***Zn-K***
Zn/Fe-P2-(1)_pt1	7.13	34.62	1.82	22.22	30.09
Zn/Fe-P2-(1)_pt2	11.90	47.95	1.43	14.22	22.57
Zn/Fe-P2-(1)_pt3	10.94	45.79	0.91	11.78	27.62
Zn/Fe-P2-(1)_pt4	7.72	49.22	1.25	12.12	23.84
Zn/Fe-P2-(1)_pt5	7.14	34.63	1.25	16.45	35.51

Although no oxide products could be detected optically, the EDX measurements showed that more oxide species were present in the weld seam than in the center and the surrounding matrix of the welding point. The potential values in the line-scan were always more anodic than the Fe/Fe^{2+} potential and the weld seam was even more anodic than the rest of the sample. These results indicate that a homogeneous corrosion was expectable and the cathodic corrosion protection was reduced.

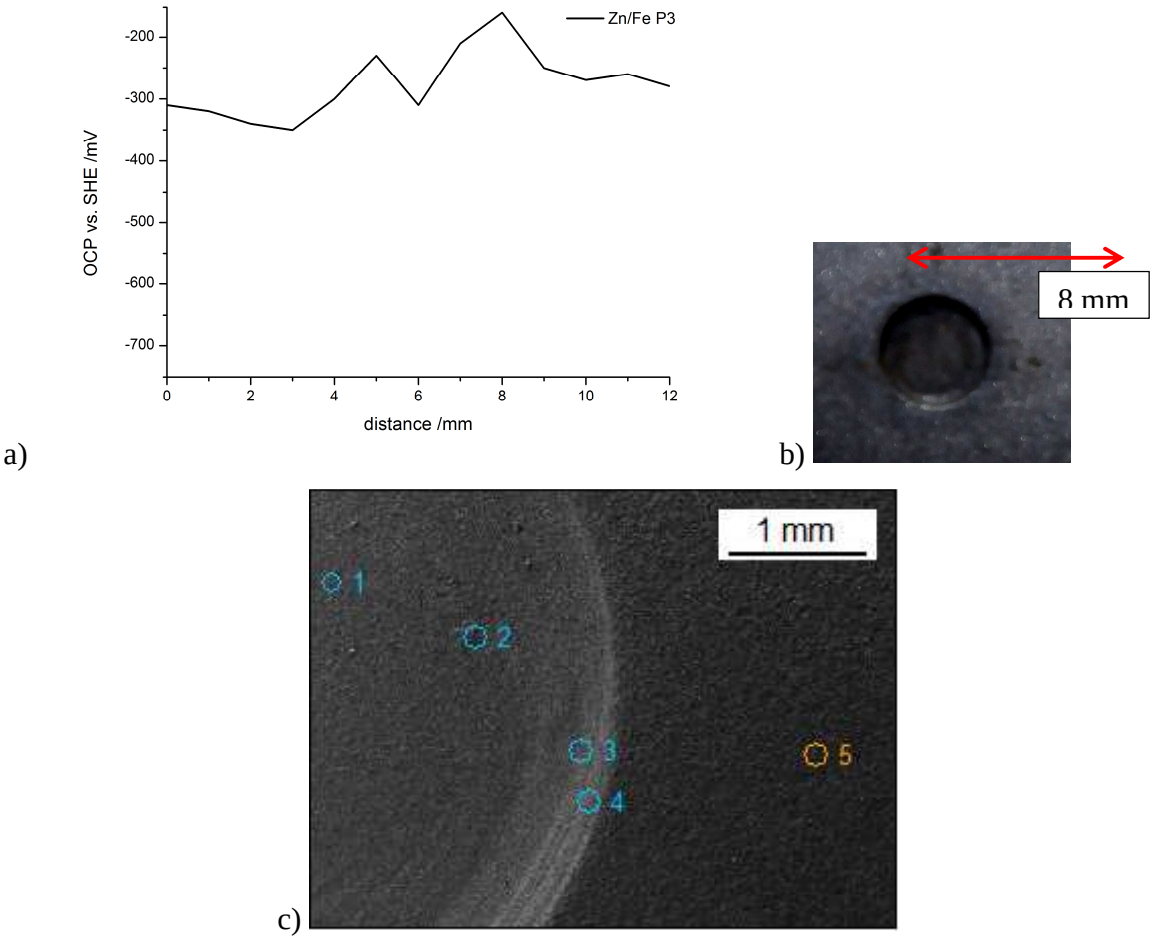

Figure 57: investigations of the welding point on the hot-formed iron containing zinc alloy coating Zn/Fe after process condition III a) OCP line-scan, b) photography of welding point with illustrated line-scan, c) FE-SEM/EDX measurement of an exemplary part of the welding point

Table 11: distribution of the relevant elements of the welding point on the hot-formed iron containing zinc alloy coating Zn/Fe after process condition III in at%

	C-K	***O-K***	***Al-K***	***Fe-K***	***Zn-K***
Zn/Fe-P3-(1)_pt1	6.80	41.25	0.86	13.72	32.85
Zn/Fe-P3-(1)_pt2	5.52	18.28	4.42	53.33	16.85
Zn/Fe-P3-(1)_pt3	8.01	51.95	2.15	10.98	22.06
Zn/Fe-P3-(1)_pt4	9.98	54.24	0.88	8.79	22.51
Zn/Fe-P3-(1)_pt5	6.65	38.84	1.28	13.49	35.05

The EDX measurements showed an increased amount of iron between the center and the weld seam where in the optical image a dark ring could be recognized. In the weld seam, the oxide content was way higher than at the rest of the sample. The potential all over the welding point and the surrounding matrix shifted to a more anodic potential in comparison to the sample after process condition II. Nevertheless, as the welding point was at a more anodic potential than the surrounding matrix it can be assumed that a cathodic corrosion protection was provided.

Cut edges were prepared in an embedding material, aged for one cycle in the climate change test, derusted and investigated via laser scanning confocal microscopy to ensure that the cathodic corrosion protection is provided after cutting the zinc coated steel sheets. Since these parts are used as safety-relevant parts in automotive industry the corrosion protection of cut edges is of high interest as are the surfaces.

The laser scanning confocal microcopy image as well as the topography image in 3D and a photography image of the hot-formed iron containing zinc alloy coating Zn/Fe is shown in Figure 58.

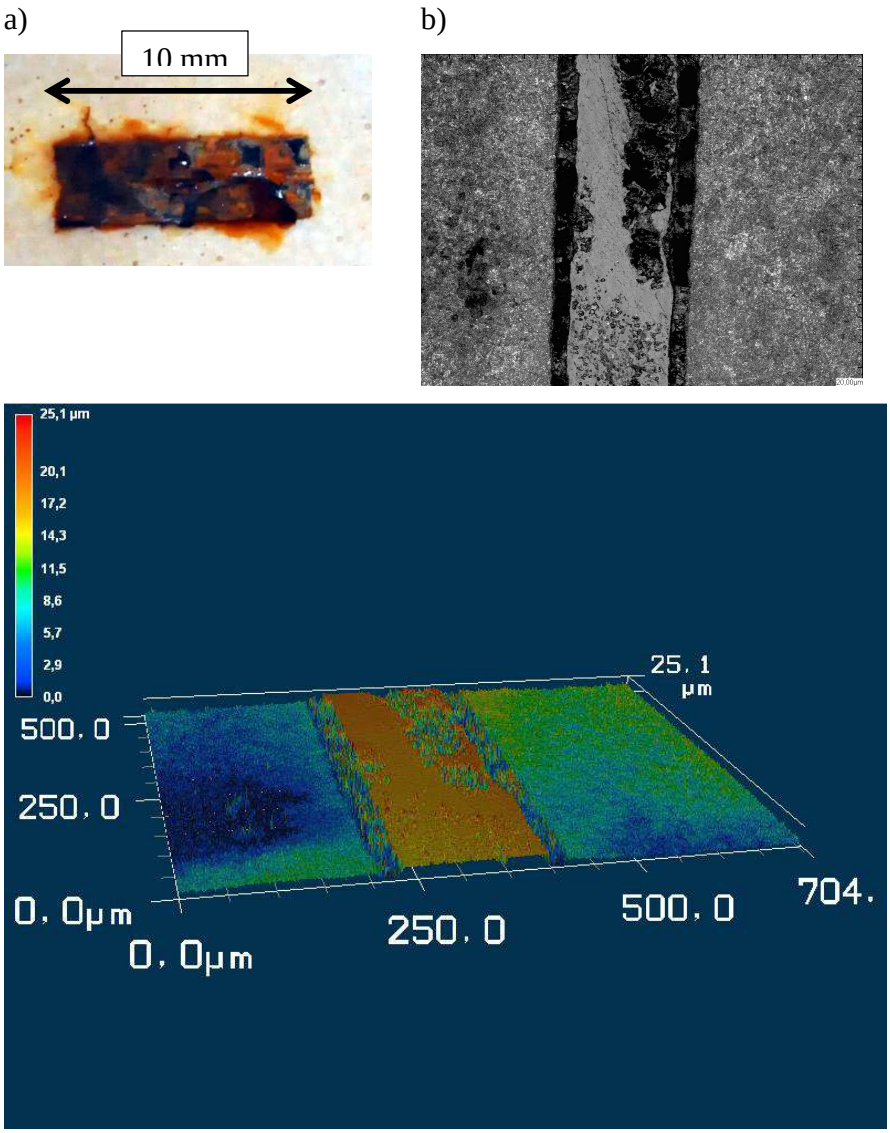

Figure 58: Laser scanning confocal microscopy investigations of embedded cut edges of hot-formed iron containing zinc alloy coated Zn/Fe sample after process condition II a) photography, b) laser microscopic image and c) 3D topography image

The iron containing zinc alloy coated Zn/Fe sample showed complete red rust formation across the whole sample. After removing the corrosion products the microscopic image

showed a strong dissolution of the alloy coating indicated by the black stripes. The 3D topography image showed a partially diminished zinc dissolution indicated by the diffuse topography in the stripes. As the height difference between the steel substrate and the embedding material was about 25 µm, the dissolution of the substrate was significant. These results are in very good agreement with the current density – potential measurement in Figure 74 where the potential of the Zn/Fe sample was more anodic than the Fe/Fe^{2+} potential and with the results of the welding point in Figure 56 where the potential line-scan indicated that a homogeneous corrosion was expectable and the cathodic corrosion protection was reduced.

4.2.4. Investigations of the nickel containing zinc alloy coating after hot-forming

For the investigation of residual oxide scales and the surface appearance of the shot-blasted samples as well as for the characterization and the distribution of phosphates after phosphating FE-SEM analysis were performed. In Figure 59 the FE-SEM images of the nickel containing zinc alloy coating Zn/Ni after shot-blasting and after phosphating are shown.

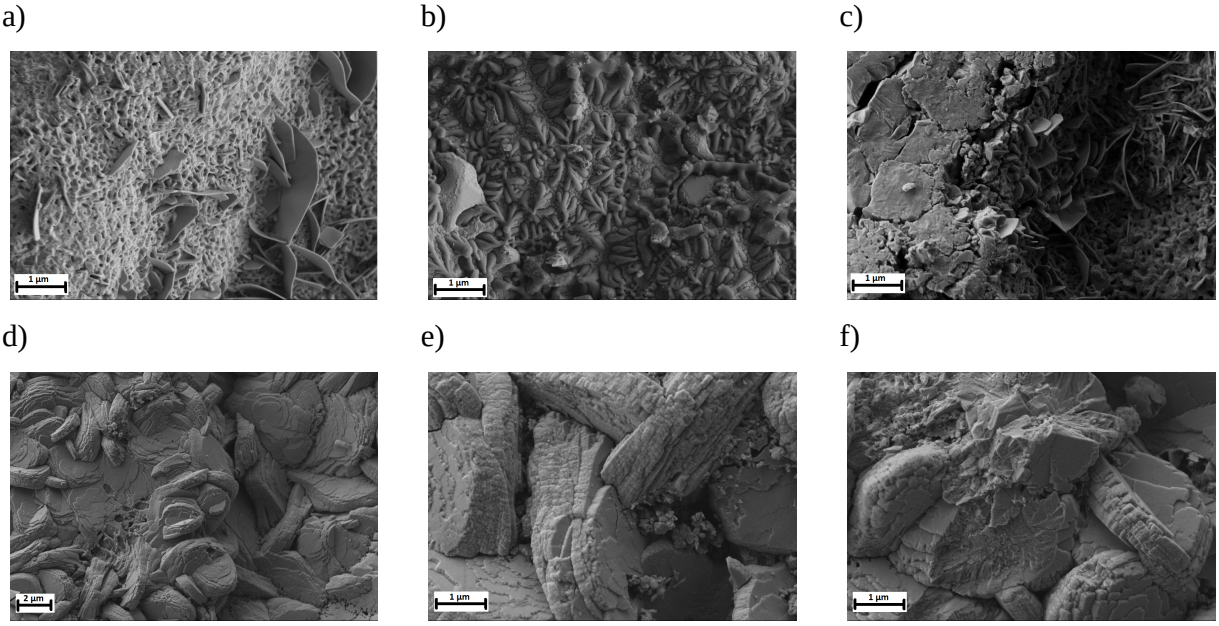

Figure 59: FE-SEM images a) – c) Zn/Ni hot-formed at process conditions I, II & III and d) – f) phosphated Zn/Ni hot-formed at process conditions I, II & III

Disc-like formations propagated with increasing process conditions, indicating the formation of oxides. The nickel containing zinc alloy coating showed these formations even at the shortest process time, which indicated that a passive oxide layer was already present. Like on the other zinc alloy coatings the heat-treatment before phosphating did not influence the appearance of the phosphate plates.

FE-SEM images were supplemented by EDX mappings of the nickel containing zinc alloy coated Zn/Ni samples. Figure 60 – Figure 62 show the mappings of the shot blasted samples and Figure 63 – Figure 65 show the mappings of the phosphated samples.

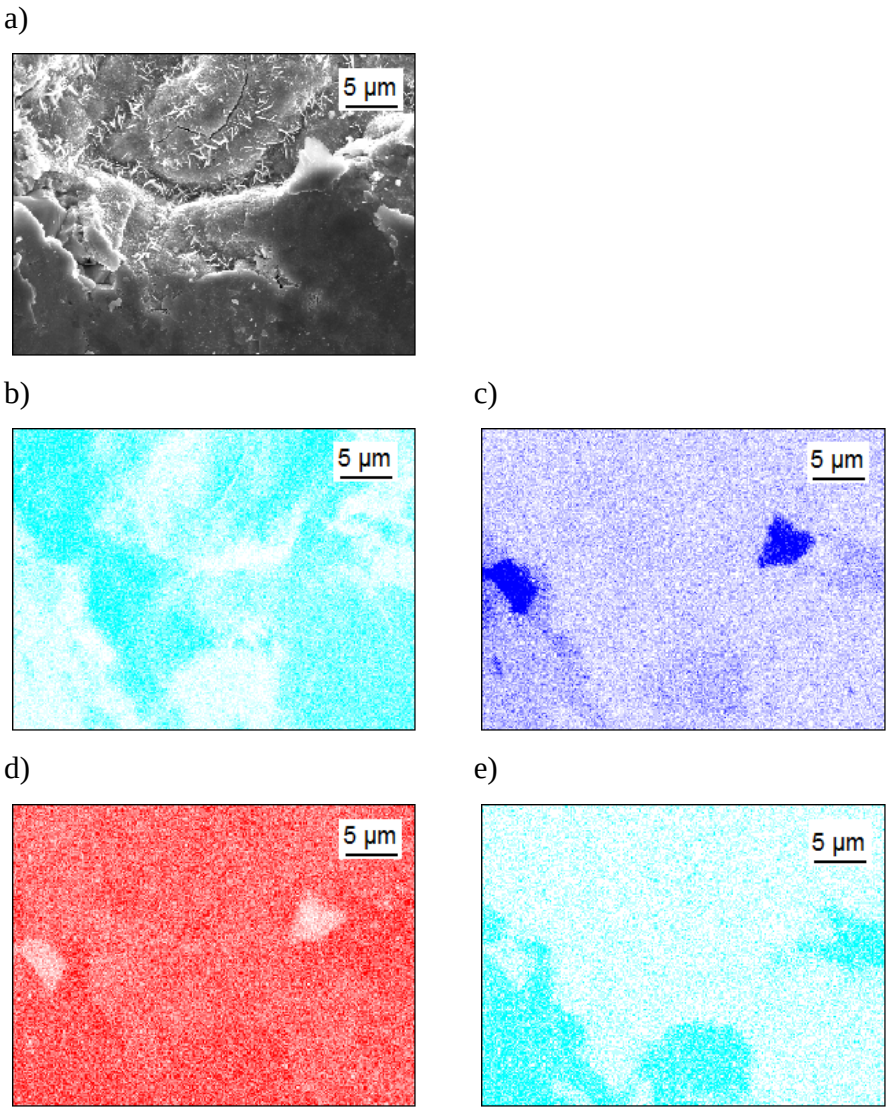

Figure 60: EDX Mappings of Zn/Ni sample after process condition I a) FE-SEM image, b) O distribution, c) Fe distribution, d) Zn distribution and e) Ni distribution

For process condition I the nickel content was not as homogenous as the zinc content. On the spots where the nickel content was increased the zinc and iron contents were slightly increased as well. The oxygen content was decreased on these points but was increased where the zinc and the iron content were increased. This indicates that the nickel reduced the zinc oxidation and therefore reduced the cathodic corrosion protection ability of the zinc.

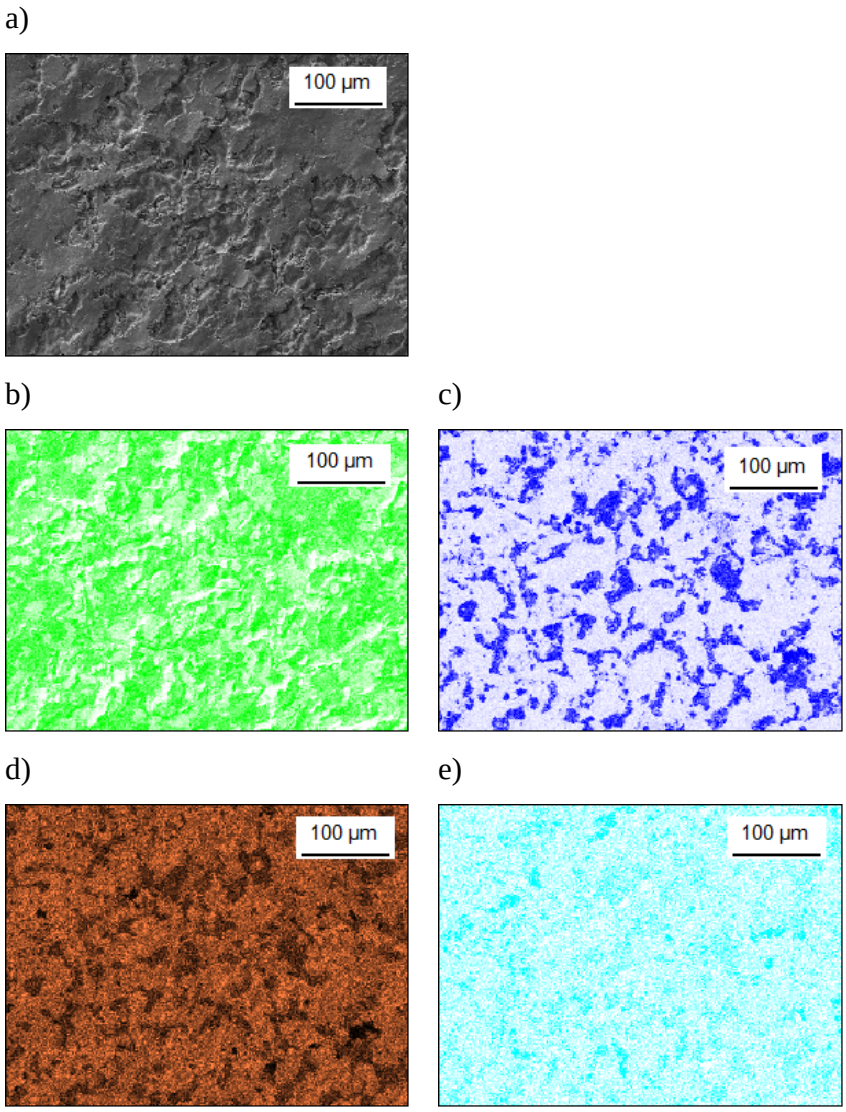

Figure 61: EDX Mappings of Zn/Ni sample after process condition II a) FE-SEM image, b) O distribution, c) Fe distribution, d) Zn distribution and e) Ni distribution

After process condition II zinc and nickel were distributed homogenously over the sample. The oxygen content was significantly decreased where the nickel content was increased and was increased with the zinc content. It seemed that the iron and zinc contents were intensified at the surface with respect to the nickel content. This indicates that the zinc oxidation and therefore the cathodic corrosion protection were provided.

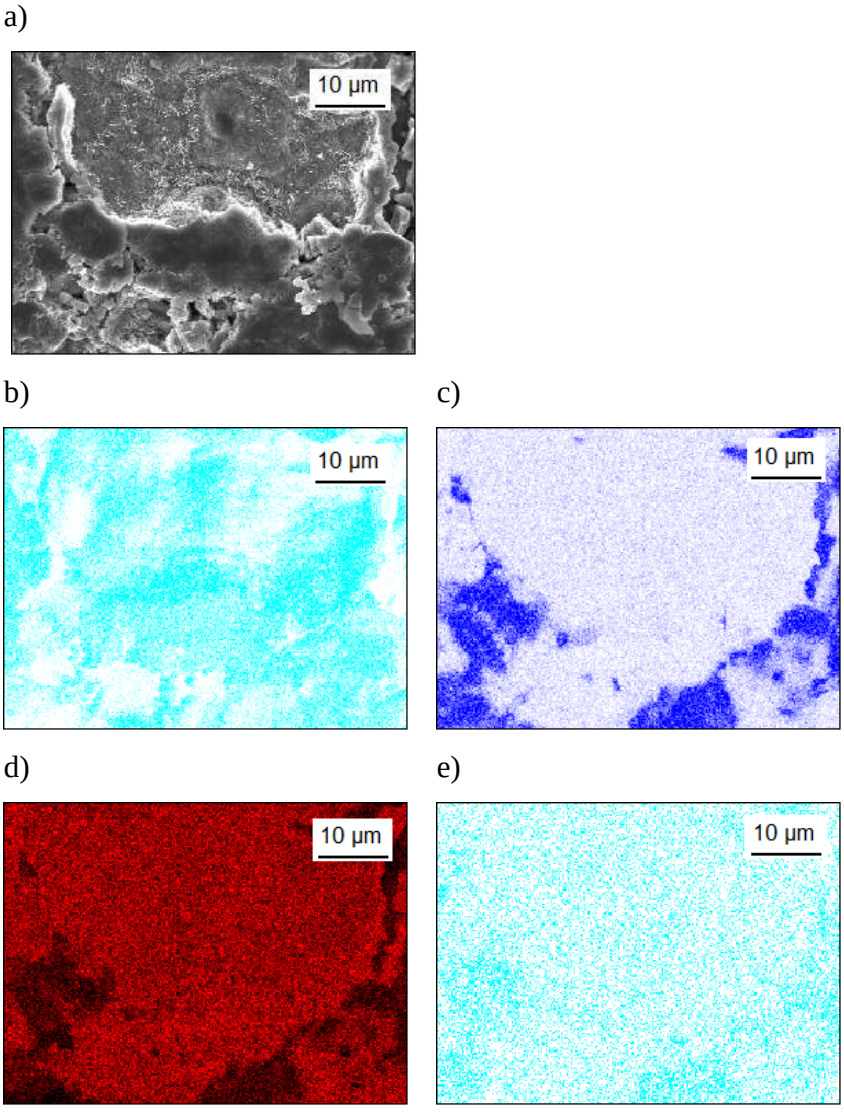

Figure 62: EDX Mappings of Zn/Ni sample after process condition III a) FE-SEM image, b) O distribution, c) Fe distribution, d) Zn distribution and e) Ni distribution

After process condition III it could be seen that the distributions of the nickel content correlated with the iron content. On the spots where nickel and iron were increased zinc was significantly decreased as well as the oxygen content. This result leads to the assumption that nickel was enriched at the surface and reduced the cathodic corrosion protection ability of the zinc.

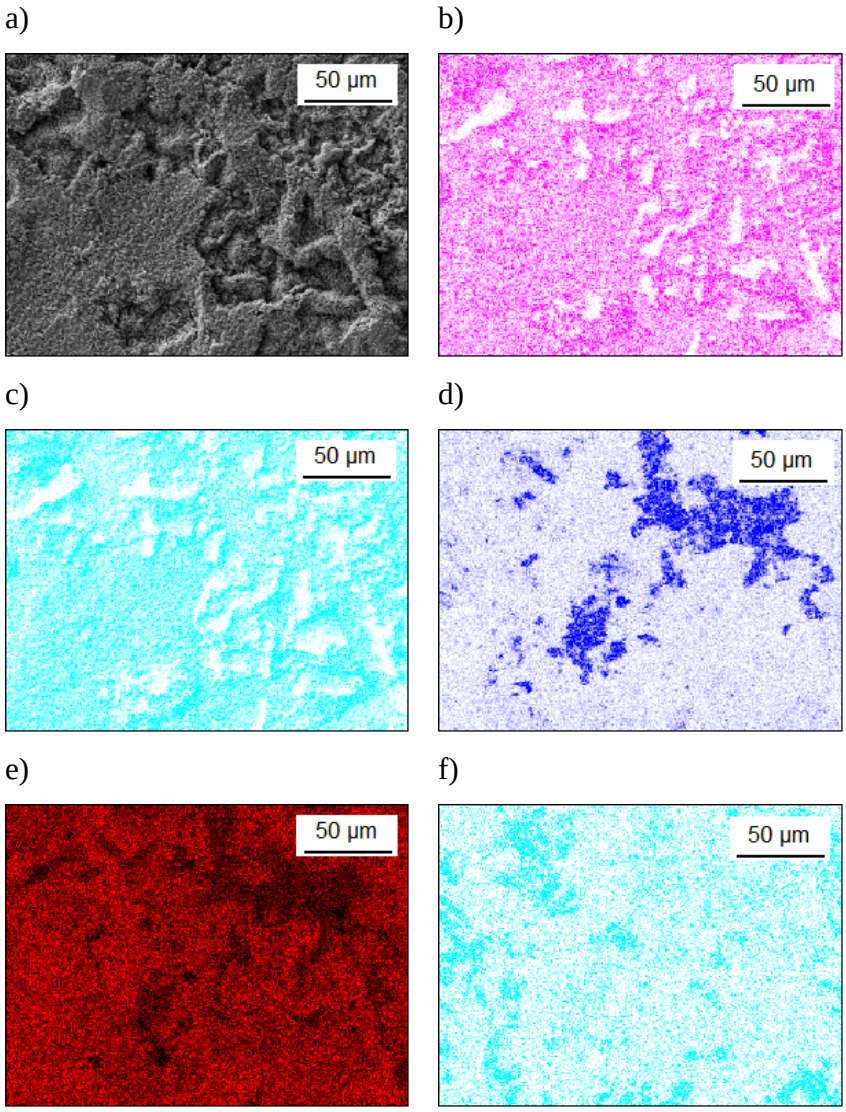

Figure 63: EDX Mappings of phosphated Zn/Ni alloy sample after process condition I a) FE-SEM image, b) P distribution, c) O distribution, d) Fe distribution, e) Zn distribution and f) Ni distribution

The nickel content did not influence the precipitation of the phosphate layer on the sample after process condition I, as no correlation of the nickel and the phosphor distributions could be detected. But in contrast to the pure zinc coating and the Zn/Fe alloy coating the coverage of the phosphate layer was in the case of the Zn/Ni alloy coating less dense even at the lowest process condition.

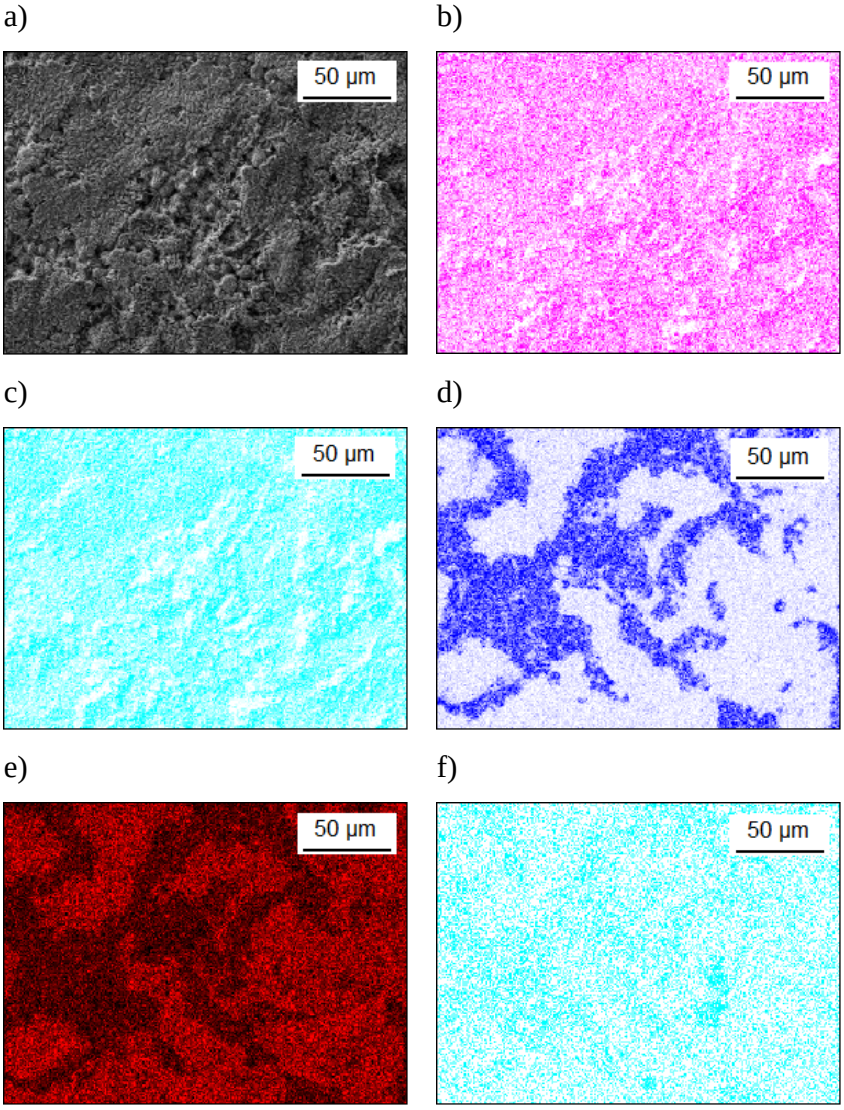

Figure 64: EDX Mappings of phosphated Zn/Ni alloy sample after process condition II a) FE-SEM image, b) P distribution, c) O distribution, d) Fe distribution, e) Zn distribution and f) Ni distribution

After process condition II the phosphate layer was denser again. The content of zinc and iron was significantly higher than the nickel content. These results agreed with the EDX mappings of the Zn/Ni alloy coating after shot blasting in Figure 61 that the iron and zinc contents were intensified at the surface with respect to the nickel content and therefore the precipitation of a phosphate layer was enhanced.

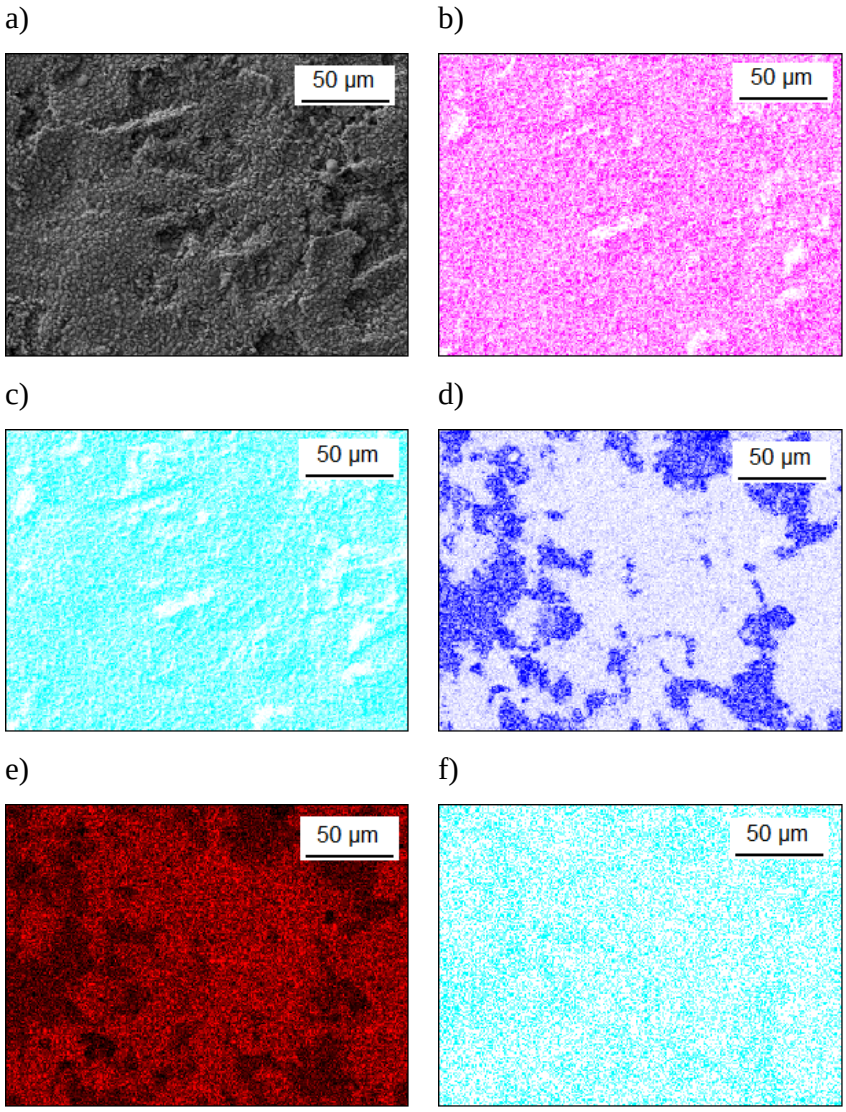

Figure 65: EDX Mappings of phosphated Zn/Ni alloy sample after process condition III a) FE-SEM image, b) P distribution, c) O distribution, d) Fe distribution, e) Zn distribution and f) Ni distribution

With respect to the EDX measurements of the shot blasted Zn/Ni alloy coating after process condition III shown in Figure 62 the increased nickel content on the surface seemed to lead to a decrease of the dense of the phosphate layer, as the content of phosphor and oxygen were partially decreased and the zinc and iron contents were increased.

Coulometric ICP-OES measurements were performed to investigate how far the hot-forming process changes the composition of the alloy coatings. The samples were coulometrically dissolved and the dissolved elements were detected in a down-stream ICP-OES. The results of the coulometry measurements with down-stream ICP-OES for the nickel containing zinc alloy coating at the different process conditions are shown in Figure 66 – Figure 68.

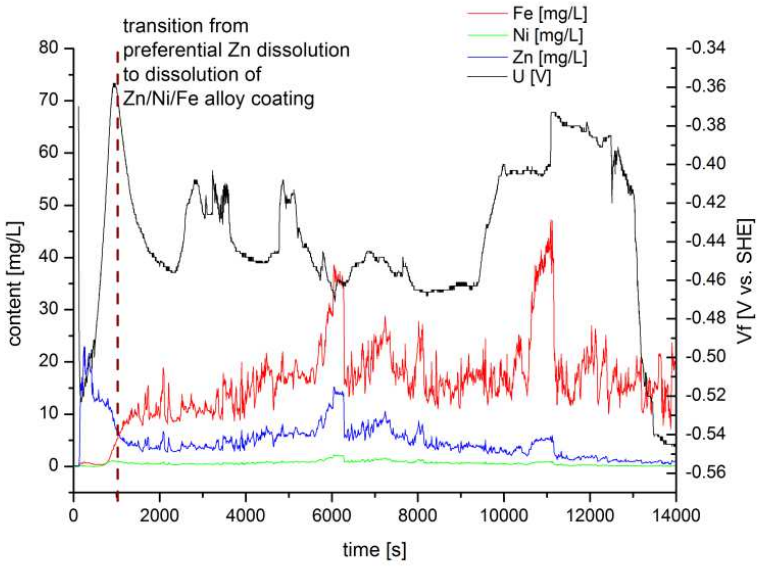

Figure 66: coulometric ICP-OES measurement of the hot-formed nickel containing zinc alloy Zn/Ni at process condition I with indicated transition from alloy coating dissolution to the dissolution of the substrate

The sample after process condition I showed a preferential zinc dissolution at a potential of -0.52 V(SHE), which was followed by a parallel dissolution of iron, zinc and nickel. At the moment the nickel started to dissolve the potential increased significantly to about -0.36 V(SHE). The zinc dissolution was inhibited by the nickel dissolution and a premature

dissolution of the substrate occurred. Only a short-time cathodic corrosion protection was provided before the nickel dissolution inhibited the zinc dissolution.

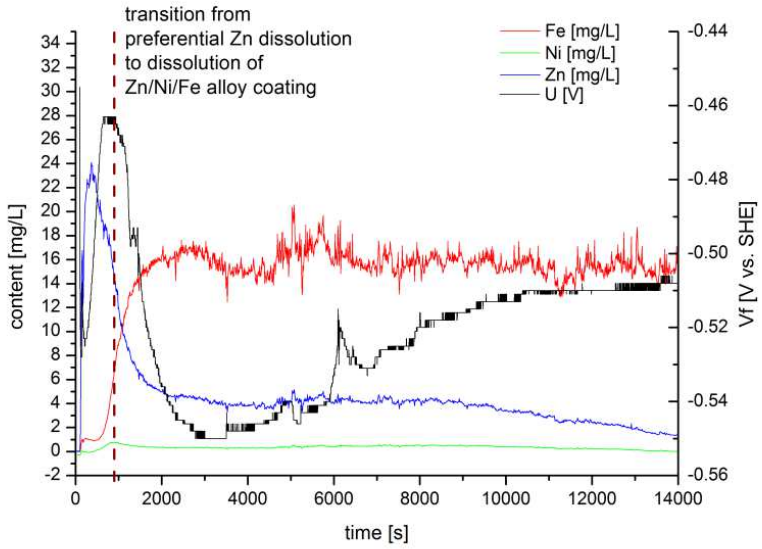

Figure 67: coulometric ICP-OES measurement of the hot-formed nickel containing zinc alloy Zn/Ni at process condition II with indicated transition from alloy coating dissolution to the dissolution of the substrate

After process condition II the preferential zinc dissolution which was followed by the parallel dissolution of zinc, iron and nickel occurred in nearly the same behavior than after process condition I. But the increase of the potential when the nickel started to dissolve was not that large. The potential increased all over the measuring time from about -0.55 V(SHE) to -0.51 V(SHE). This indicates that a stronger alloying of iron into the Zn/Ni alloy coating took place.

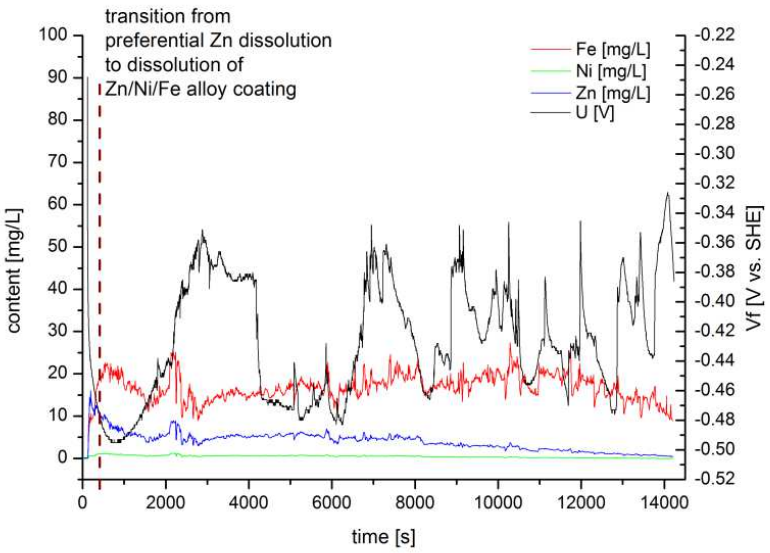

Figure 68: coulometric ICP-OES measurement of the hot-formed nickel containing zinc alloy Zn/Ni at process condition III with indicated transition from alloy coating dissolution to the dissolution of the substrate

The zinc dissolution was inhibited by the nickel dissolution after short preferential zinc dissolution for process condition III. In the moment the nickel started to dissolve the potential fluctuated strongly between the Fe/Fe^{2+} potential and the mixed potential of -0.36 V(SHE), seen in Figure 66 when nickel started to dissolve. A cathodic corrosion protection of the alloy was not provided caused by the fluctuating passivation and dissolution of the nickel which inhibited the zinc dissolution.

To examine the potential distribution in the center, in the weld seam and in the surrounding matrix, the OCP in an aqueous 0.05 mol/L NaCl solution was measured as line scan over the welding spot by use of a scanning capillary cell with a local resolution of 1 mm for 5 min at each point. In addition to the potential distributions the distributions of the alloy coating elements were detected by means of EDX measurements. In Figure 69 – Figure 71 the OCP line scans of the weld seams and photography images with indicated measurement direction of the iron containing Zn/Fe sample for the different process conditions are shown.

Accompanying FE-SEM images with indicated spots for EDX measurements are placed under each line scan. The results of the EDX measurements are shown in Table 12 – Table 14 under Figure 69 – Figure 71, respectively.

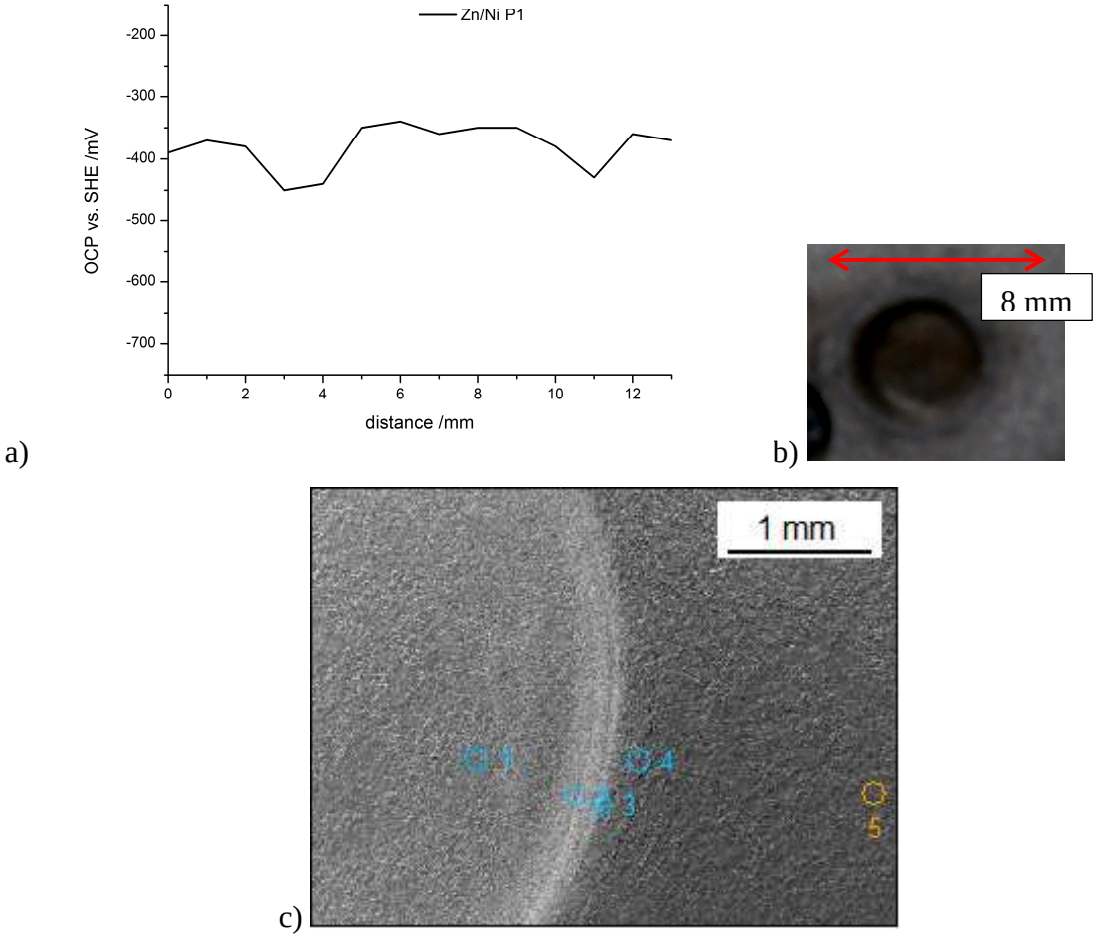

Figure 69: investigations of the welding point on the hot-formed nickel containing zinc alloy coating Zn/Ni after process condition I a) OCP line-scan, b) photography of welding point with illustrated line-scan, c) FE-SEM/EDX measurement of an exemplary part of the welding point

Table 12: distribution of the relevant elements of the welding point on the hot-formed nickel containing zinc alloy coating Zn/Ni after process condition I in at%

	C-K	***O-K***	***Al-K***	***Fe-K***	***Ni-K***	***Zn-K***
Zn/Ni-P1-(1)_pt1	6.12	38.68		14.34	2.35	33.83
Zn/Ni-P1-(1)_pt2	8.78	44.63		8.28	2.24	33.42
Zn/Ni-P1-(1)_pt3	9.84	46.69		6.37	1.71	32.16
Zn/Ni-P1-(1)_pt4	10.49	38.51	5.66	7.02	1.26	34.15
Zn/Ni-P1-(1)_pt5	4.82	32.41		15.73	2.06	39.28

After process condition I optically no iron oxides could be detected but the EDX measurements showed that the oxide content in the weld seam was higher than in the rest of the welding point. In addition to these measurements the potential line-scan showed that the weld seam was more cathodic than the center and the surrounding matrix and was at about the Fe/Fe^{2+} potential. The center and the surrounding matrix were more anodic than the Fe/Fe^{2+} potential and way more anodic than the Zn/Zn^{2+} potential. This indicates that the weld seam may dissolve partially in favor of the center and the surrounding matrix of the welding point. The anodic potentials were in very good agreement with the coulometric ICP-OES measurements in Figure 67 and indicated the alloying of iron into the Zn/Ni alloy coating.

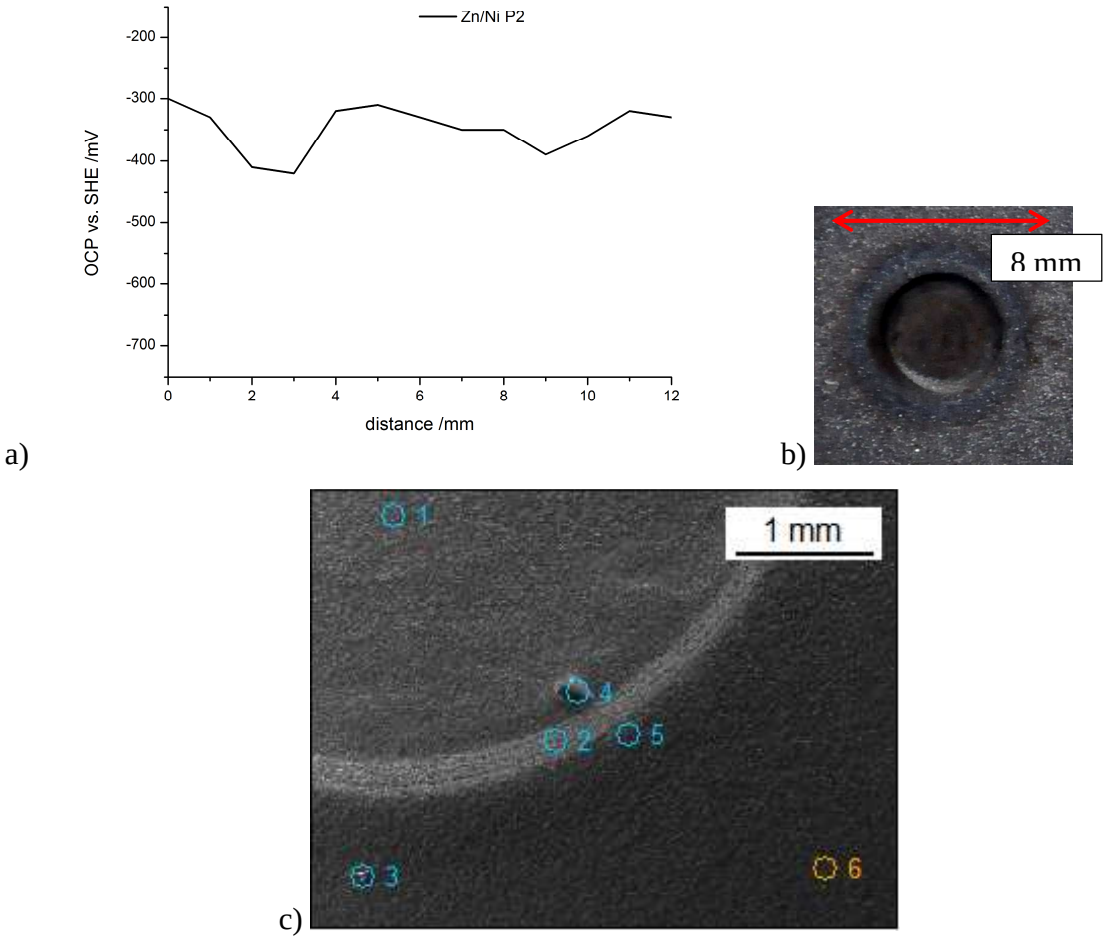

Figure 70: investigations of the welding point on the hot-formed nickel containing zinc alloy coating Zn/Ni after process condition II a) OCP line-scan, b) photography of welding point with illustrated line-scan, c) FE-SEM/EDX measurement of an exemplary part of the welding point

Table 13: distribution of the relevant elements of the welding point on the hot-formed nickel containing zinc alloy coating Zn/Ni after process condition II in at%

	C-K	***O-K***	***Al-K***	***Fe-K***	***Ni-K***	***Zn-K***
Zn/Ni-P2-(1)_pt1	7.16	38.22		14.00	1.14	33.69
Zn/Ni-P2-(1)_pt2	9.64	48.31		8.33	0.79	29.35
Zn/Ni-P2-(1)_pt3	4.77	39.94	0.88	22.09	0.96	27.45
Zn/Ni-P2-(1)_pt4	44.79	27.29		3.68	0.72	10.59
Zn/Ni-P2-(1)_pt5	5.72	44.35		8.69	0.71	35.23
Zn/Ni-P2-(1)_pt6	8.02	38.25		14.05	0.75	32.15

The increased process time at the process condition II led to a stronger effect described at Figure 69 for the nickel containing zinc alloy coating after process condition I. Optically no iron oxides could be seen, indicating that the nickel inhibited the evaporation of the zinc alloy coating. But EDX measurements showed that the oxide content in the weld seam was higher than in the rest of the welding point. In addition to these measurements the potential line-scan showed that the weld seam was more cathodic than the center and the surrounding matrix. Parts of the weld seam may dissolve in favor of the center and the surrounding matrix of the welding point as the potential of the weld seam was at the Fe/Fe^{2+} potential and therefore much more cathodic than the center and the matrix.

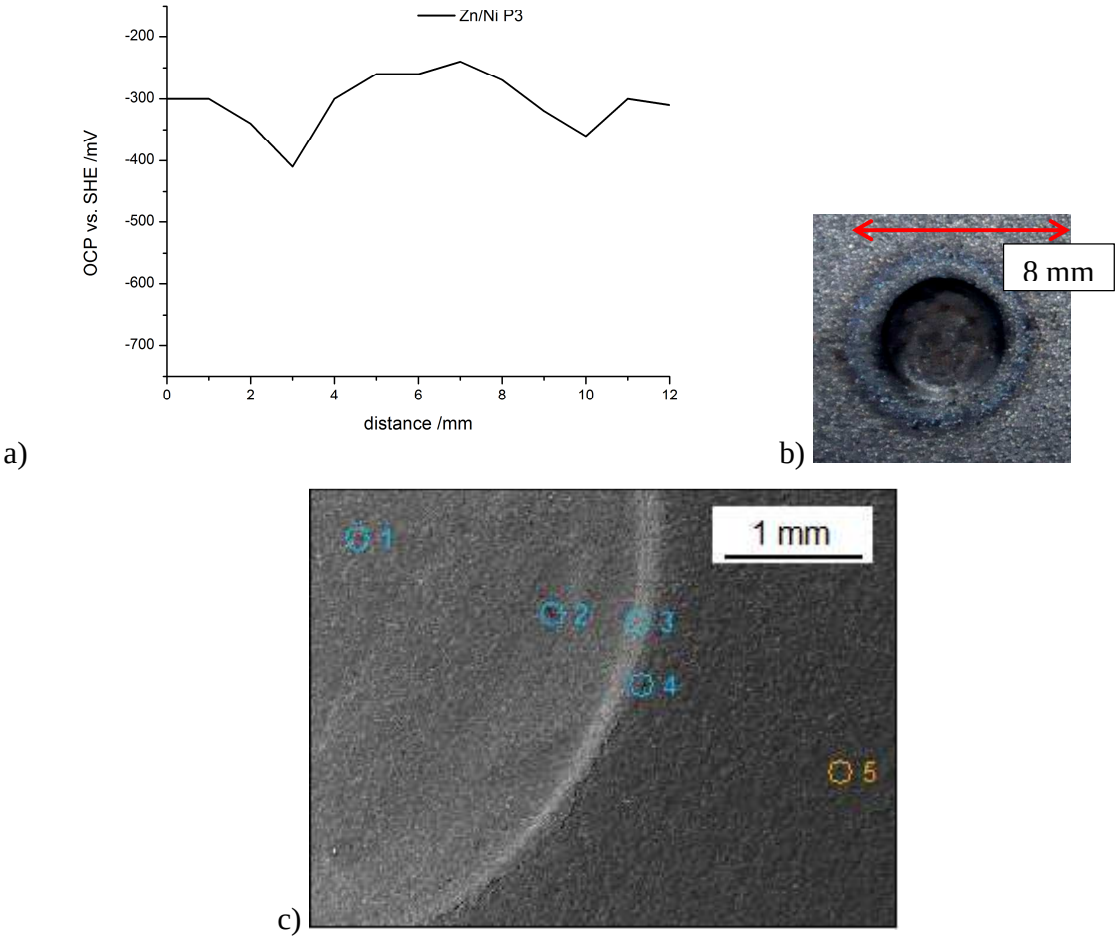

Figure 71: investigations of the welding point on the hot-formed nickel containing zinc alloy coating Zn/Ni after process condition III a) OCP line-scan, b) photography of welding point with illustrated line-scan, c) FE-SEM/EDX measurement of an exemplary part of the welding point

Table 14: distribution of the relevant elements of the welding point on the hot-formed nickel containing zinc alloy coating Zn/Ni after process condition III in at%

	C-K	***O-K***	***Al-K***	***Fe-K***	***Ni-K***	***Zn-K***
Zn/Ni-P3-(1)_pt1	7.91	39.24		13.66	0.85	32.85
Zn/Ni-P3-(1)_pt2	27.12	33.95		6.76	0.64	19.66
Zn/Ni-P3-(1)_pt3	10.37	50.56		8.54	0.39	27.39
Zn/Ni-P3-(1)_pt4	7.68	48.03		14.14	0.39	25.41
Zn/Ni-P3-(1)_pt5	7.07	36.63	0.14	15.87	0.86	33.50

Although optically no iron oxide products were visible after process condition III the EDX measurements showed that in the weld seam the oxygen content was increased in comparison to the rest of the sample. A ring around the welding point indicated thermal stress and the EDX measurements showed an increased amount of nickel as well in the center of the welding point as in the ring, induced by thermal stress. This result was validated by the potential line-scan as the center of the welding point was at the Ni/Ni^{2+} potential, indicating that nickel precipitated. As the weld seam was way more cathodic than the center and the surrounding matrix it can be assumed that the weld seam dissolves partially in favor of the center and the matrix.

In the direct hot-forming process the zinc alloy coated steel parts are cut before they are cleaned and used as safety-relevant parts in the automobile. Hence the cathodic corrosion protection of cut edges is of crucial importance likewise. Therefore cut edges were prepared in an embedding material, aged for one cycle in the climate change test, derusted and investigated via laser scanning confocal microscopy. The laser scanning confocal microcopy image as well as the topography image in 3D and photography image of the nickel containing zinc alloy coating is shown in Figure 72.

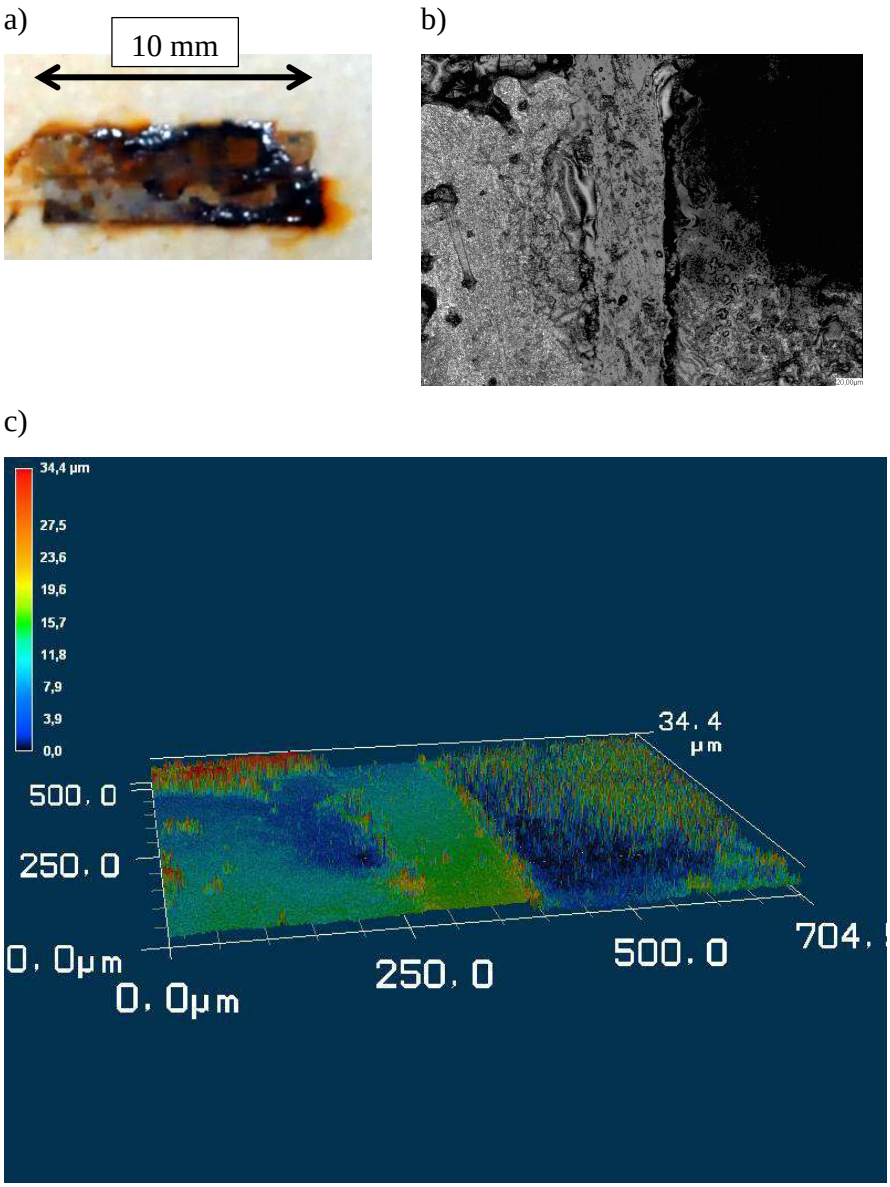

Figure 72: Laser scanning confocal microscopy investigations of embedded cut edges of hot-formed nickel containing zinc alloy coated Zn/Ni sample after process condition II a) photography, b) laser microscopic image and c) 3D topography image

On the nickel containing zinc alloy coated Zn/Ni sample an inhomogeneous corrosion could be seen after the climate change test. After removing the corrosion products, the strong, homogeneous dissolution of the alloy coating as well as a partial dissolution of the steel substrate could be seen in the microscopic image and in the 3D topography image. These results are in very good agreement with the investigations before for the Zn/Ni sample after

process condition II where the potential of the alloy coating was more anodic than the Fe/Fe^{2+} potential. Caused by the nickel dissolution and the resulting inhibition of the zinc dissolution the cathodic corrosion protection was reduced.

4.2.5. Potentiodynamic studies of hot-formed zinc alloy coated steel

A further question of crucial importance was in how far the composition of the alloy coatings influences the cathodic corrosion protection ability. The current density – potential measurement gives a proper assertion about the cathodic corrosion protection ability. Therefore linear sweep voltammetry was used to show the proximity of the corrosion potential to the free corrosion potential of the Fe/Fe^{2+} reaction. The results shown in Figure 73 – Figure 75 show the current density – potential curves for each process condition in comparison to the reference sample Z140 with marked Fe/Fe^{2+} transition potential for the shot-blasted samples and in Figure 76 – Figure 78 for the phosphated samples. In Table 15 and Table 16 the values for the OCP and the corrosion current density are listed for the shot-blasted and the phosphated samples, respectively.

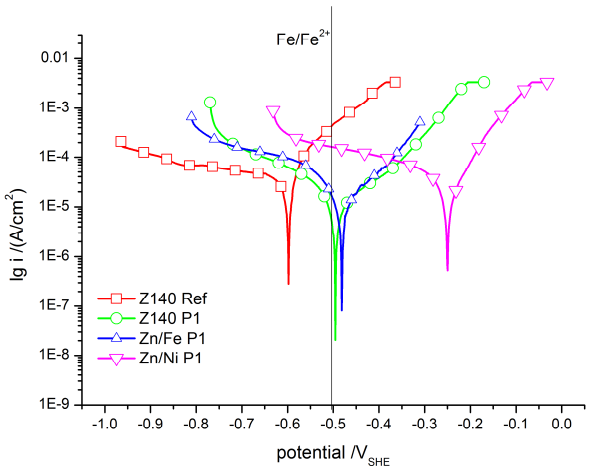

Figure 73: current density - potential curve for process condition I with marked Fe/Fe^{2+} transition potential

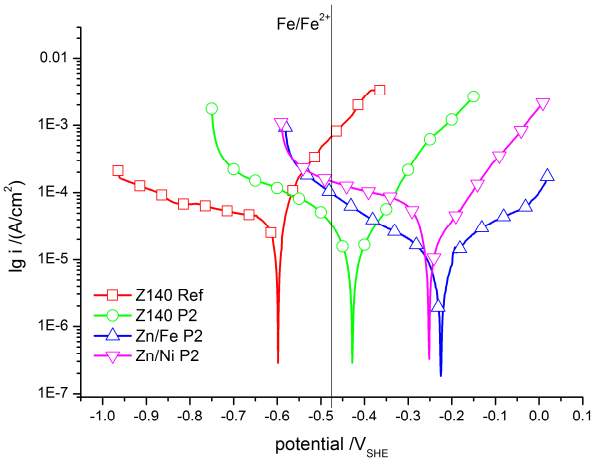

Figure 74: current density - potential curve for process condition II with marked Fe/Fe^{2+} transition potential

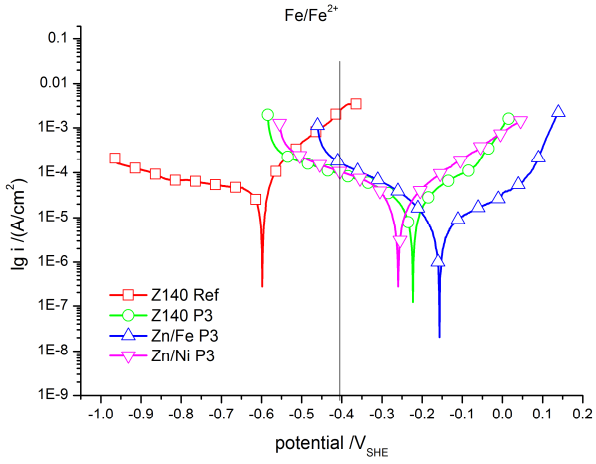

Figure 75: current density - potential curve for process condition III with marked Fe/Fe^{2+} transition potential

Table 15: current densities and corrosion potentials as a function of the different process conditions for the different alloy coatings after shot blasting

	Reference		**process condition I**		**process condition II**		**process condition III**	
	OCP / mV_{SHE}	**i_{corr} / $\mu A/cm^2$**	**OCP / mV_{SHE}**	**i_{corr} / $\mu A/cm^2$**	**OCP / mV_{SHE}**	**i_{corr} / $\mu A/cm^2$**	**OCP / mV_{SHE}**	**i_{corr} / $\mu A/cm^2$**
Z140 reference	-598.2 (+/- 32.7)	16.2 (+/- 5.2)	X	X	X	X	X	X
Z140 hot-formed	X	X	-474.5 (+/- 25.1)	1.2 (+/- 0.1)	-455.4 (+/- 25.4)	1.3 (+/- 0.1)	-245.1 (+/- 24.4)	0.7 (+/- 0.2)
Zn/Fe	X	X	-463.9 (+/- 16.0)	1.1 (+/- 0.5)	-216.5 (+/- 13.9)	0.5 (+/- 0.1)	-173.9 (+/- 14.5)	0.5 (+/- 0.1)
Zn/Ni	X	X	-253.5 (+/- 4.4)	2.8 (+/- 0.5)	-259.1 (+/- 6.8)	2.4 (+/- 0.3)	-248.4 (+/- 22.7)	2.5 (+/- 0.3)

The current density – potential measurements were in very good agreement with the coulometric ICP-OES measurements. On the reference sample the corrosion current density was significantly higher than on the other samples as zinc dissolution took place to cathodically protect the substrate. With increasing process time the potentials shifted to a more anodic potential which indicates the transition to Fe^{3+} species. The nickel containing zinc alloy coating was at a more anodic potential even after process condition I. This validates the reduced cathodic corrosion protection ability of the Zn/Ni alloy coating induced by the nickel dissolution and the hereby caused inhibition of the zinc dissolution.

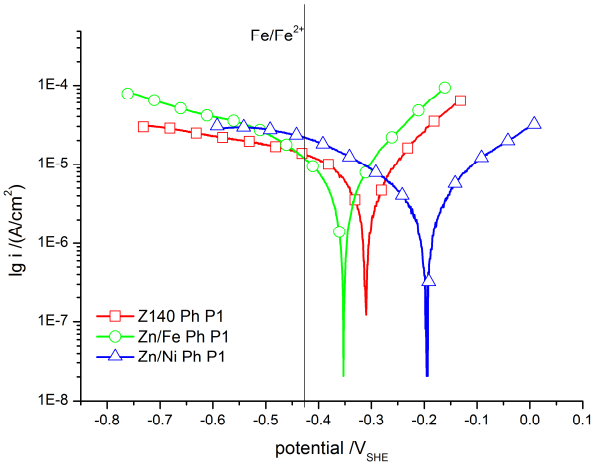

Figure 76: current density - potential curve for the phosphated samples after process condition I with marked Fe/Fe^{2+} transition potential

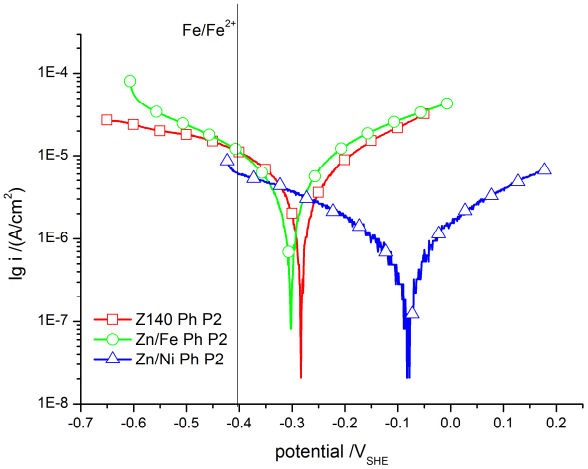

Figure 77: current density - potential curve for the phosphated samples after process condition II with marked Fe/Fe^{2+} transition potential

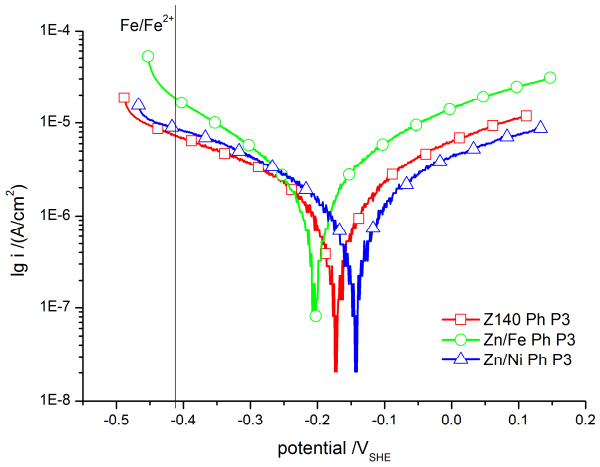

Figure 78: current density - potential curve for the phosphated samples after process condition III with marked Fe/Fe^{2+} transition potential

Table 16: current densities and corrosion potentials as a function of the different process conditions for the different alloy coatings after phosphating

	process condition I		**process condition II**		**process condition III**	
	OCP / mV_{SHE}	**i_{corr} / $\mu A/cm^2$**	**OCP / mV_{SHE}**	**i_{corr} / $\mu A/cm^2$**	**OCP / mV_{SHE}**	**i_{corr} / $\mu A/cm^2$**
Z140 hot-formed Ph	-323.8 (+/- 19.4)	0.5 (+/- 0.1)	-274.8 (+/- 12.2)	0.5 (+/- 0.1)	-167.9 (+/- 6.6)	0.1 (+/- 0.02)
Zn/Fe Ph	-341.9 (+/- 15.2)	0.5 (+/- 0.1)	-207.4 (+/- 133.7)	0.1 (+/- 0.03)	-201.8 (+/- 1.5)	0.1 (+/- 0.03)
Zn/Ni Ph	-179.9 (+/- 19.2)	0.2 (+/- 0.03)	-185.8 (+/- 8.7)	0.1 (+/- 0.02)	-139.8 (+/- 3.5)	0.1 (+/- 0.0001)

After phosphating the potentials were shifted to more anodic values and the corrosion current densities decreased significantly. This indicates that a protecting phosphate layer, deposited on the substrates, as it could be seen in the EDX measurements in Figure 35 – Figure 37, Figure 49 – Figure 51 and Figure 63 – Figure 65, led to an initial inhibition of the cathodic corrosion protection ability of the zinc alloy coatings.

4.2.6. Conclusions

Concluding the results for the investigation of different alloy coatings for the 22MnB5 steel, it could be shown that the coulometric ICP-OES was a suitable method for the well-controlled dissolution of the investigated alloy coatings. The gathered potential curves during the coulometric dissolution were in very good agreement with the dissolution behavior of the alloying elements.

It could be shown that the alloying of nickel led to preferential zinc dissolution, caused nickel enrichment in the alloy coating and resulted in passivation of the surface which reduced the cathodic corrosion protection ability of such an alloy coating.

Caused by the heat treatment, an alloying of iron from the substrate in the alloy coating occurred. This behavior led to an inhibition of the zinc dissolution current density.

By means of current density – potential curves, the results achieved by the coulometric ICP-OES measurements were validated as the increased amount of iron in the alloy coating as well for the hot-formed pure zinc coating Z140, and for the iron containing zinc alloy Zn/Fe, led to a decrease in the corrosion current density. For the nickel containing zinc alloy Zn/Ni it could be shown that the corrosion current density increased which indicated the preferential zinc dissolution, enrichment of nickel, passivation of the surface and hence the inhibition of further zinc dissolution.

Phosphating the samples led to a decrease in the corrosion current density as well as an anodic shift of the corrosion potential of the samples. These results indicated that the phosphate layer inhibited the cathodic corrosion protection ability of the alloy coating initially until the barrier function broke down.

The investigations of the welding points clearly showed that the pure zinc coatings, before and after hot-forming, as well as the iron containing zinc alloy coatings provided a cathodic corrosion protection of the welding point as the potential in the center as well as in the weld seam was increased in comparison to the surrounding matrix. The alloying of nickel led to a significant decrease of the potential in the weld seam and a slight increase of the potential in

the center in comparison to the surrounding matrix. Therefore the possibility is given that the welding point will be partially affected by anodic dissolution.

For the investigation of cut edges the not hot-formed pure zinc coating did not show a corrosive attack to the steel substrate and only white rust formation caused by the slight zinc dissolution. The hot-formed pure zinc coating as well as the nickel containing zinc alloy coating Zn/Ni showed dissolution of the alloy coating with, although a small amount of red rust formation could be seen, acceptable corrosion protection properties for the steel substrate. Hot-forming of the iron containing zinc alloy coating led to a corrosive attack of the substrate. As the alloy coating was dissolved partially it can be assumed that the zinc content in the alloy coating protected the iron content in the alloy coating and not the substrate.

4.3. In-situ contact angle measurements with stretch deformation of self-healing coatings

4.3.1. Scanning electron microscopy

For the evaluation of the functionality of filled capsules in organic coatings a new set-up combining a stretching device with dynamic contact angle measurement was developed. The capsules investigated were filled with MTES for water replacement only or TMODS and TMOS for water replacement and self-healing effect by film formation and dispersed into a polyurethane coating or an epoxy coating like described chapter 3.3.1. In comparison to the capsules containing coatings a coating without capsules was likewise tested. To illustrate the defect formation FE-SEM images were taken before and after stretching with an elongation of 15 % of the pure PU coating and the PU coating containing capsules filled with water displacing alkoxysilanes only. These images are shown in Figure 79.

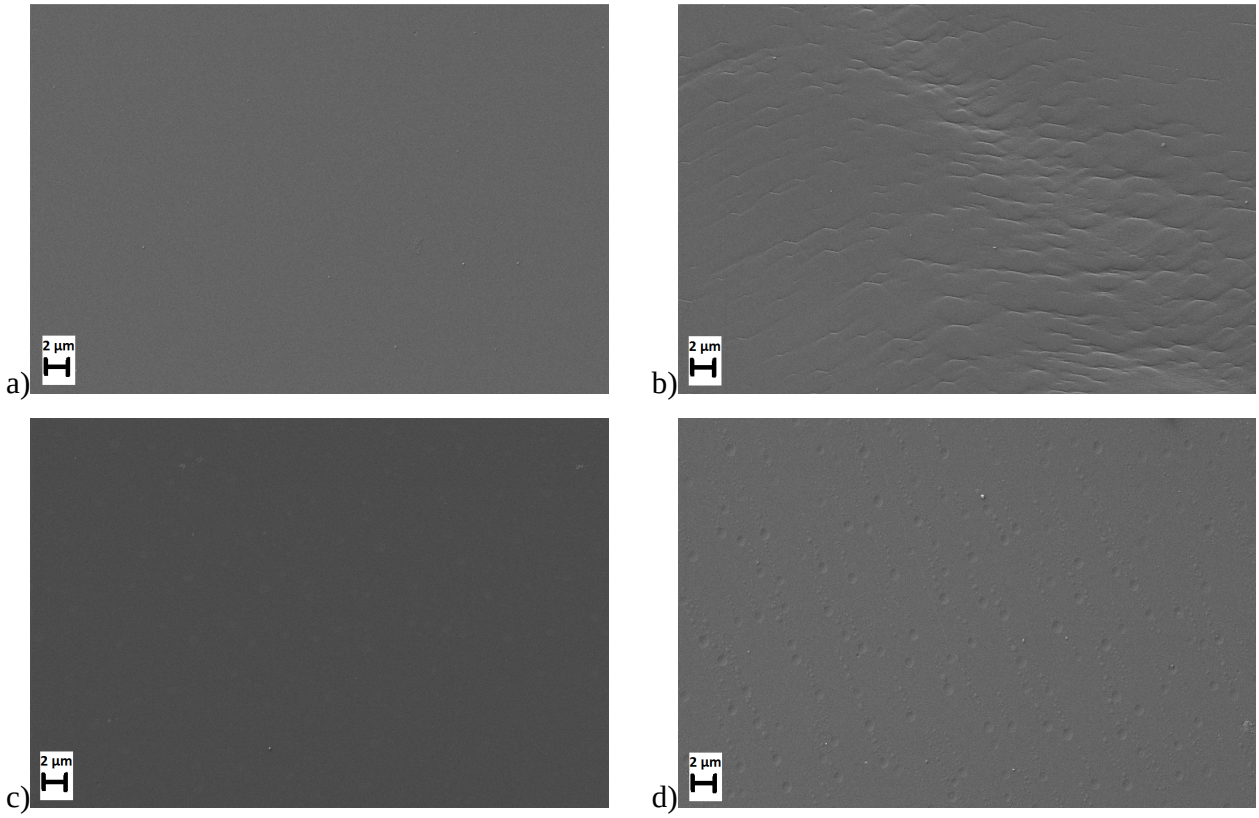

Figure 79: FE-SEM images of polyurethane coating a) without PU capsules before stretching, b) without PU capsules after 15% elongation, c) with filled PU capsules before stretching and d) with filled PU capsules after 15% elongation

The polyurethane coating without capsules had a very smooth surface before the deformation and showed wave like deformations after 15 % elongation. In the FE-SEM image of the PU capsules containing coating the capsules could be seen weakly even before the stretch forming. After 15 % elongation the coatings surface still looked smooth with indentations on the spots where the capsules were before. It seems that the capsules not only led to a hydrophobic surface, which will be demonstrated with the next measurement, but increased the mechanical properties of the coating as well.

4.3.2. Dynamic contact angle measurements

To show that the capsules broke and released the alkoxysilanes to form a water repellent surface, the left and right contact angles of a water droplet were dynamically measured during the stretch forming. As only the surface of the coating had to crack, the deformation had to be in a controlled manner. If the coating was completely damaged, the water droplet would immediately disappear to the interface between the coating and the substrate. The plot of the dynamic contact angles is given in Figure 80.

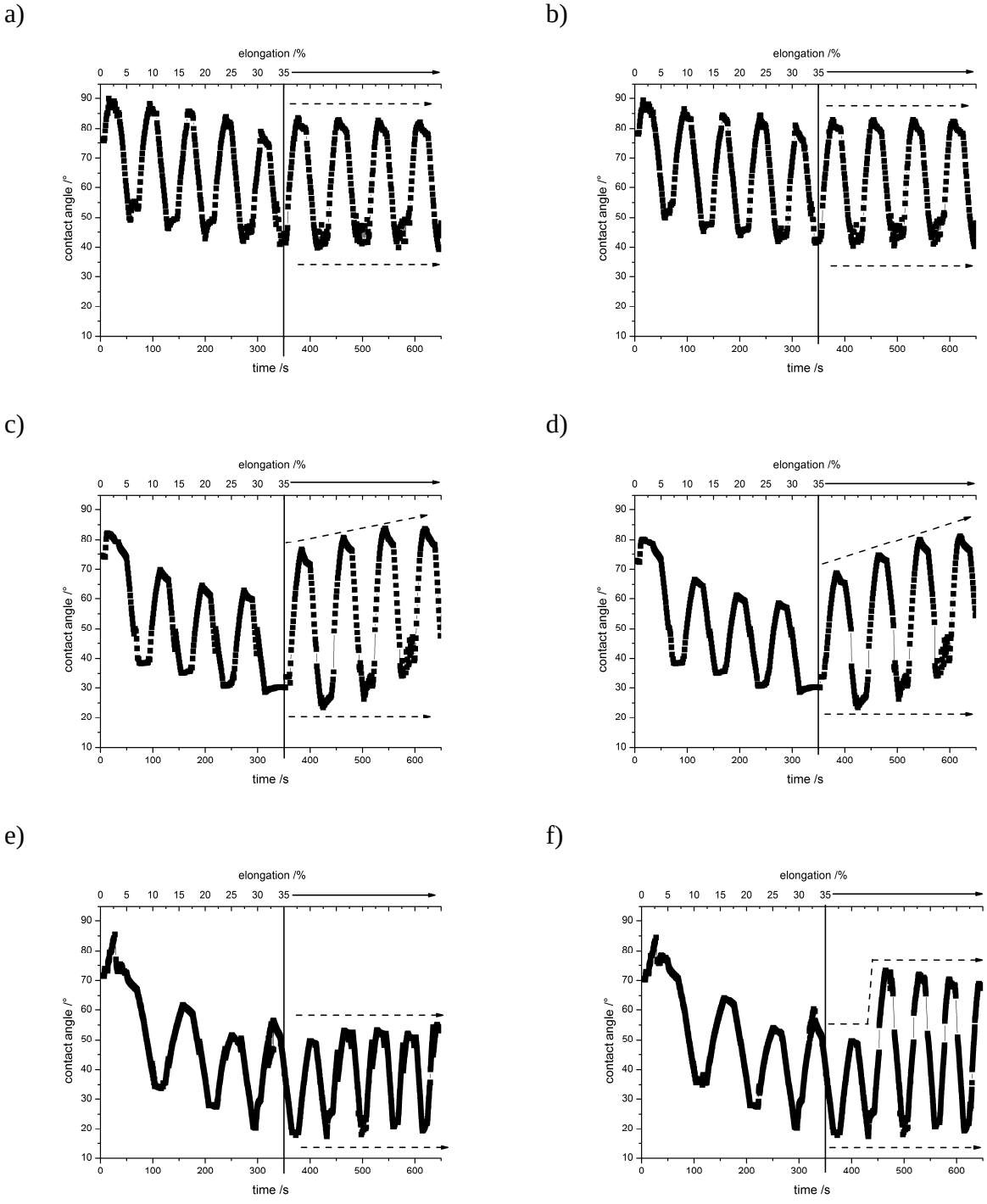

Figure 80: dynamic contact angle measurements during the deformation until 35 % and beyond a) left contact angle hysteresis of PU coating without PU capsules, b) right contact angle hysteresis of PU coating without PU capsules, c) left contact angle hysteresis of PU coating with MTES filled PU capsules, d) right contact angle hysteresis of PU coating with MTES filled PU capsules, e) left contact angle hysteresis of epoxy coating with TMODS and TMOS filled PU capsules and f) right contact angle hysteresis of epoxy coating with TMODS and TMOS filled PU capsules

It could be clearly demonstrated that the hydrophobic effect was caused by the release of the alkoxysilanes from the broken capsules as the pure coating showed no increase of the contact angle but was constant when the elongation was kept at 35 % when the surface of the coating was damaged. The capsules filled only with MTES led to an increase of the contact angle on both sides of the droplet. MTES seemed to have dissolved in the water droplet and built a hydrophobic monolayer on the wetted surface before cross-linking took place. Adding TMODS and TMOS filled capsules led to a spontaneous water repelling effect on the sides where the surface was damaged and the inhibitors were set free as it could be seen in the right contact angle hysteresis in Figure 80f. As described by Latnikova et al. [81] the mixture of alkoxysilanes with varying hydrocarbon tails led to an immediate hydrophobization of the defected surface and a subsequent cross-linking. The left contact angle hysteresis in Figure 80e showed a constant trend that indicates that the surface was not broken at this point and therefore no inhibitor was set free to build up a water repellent surface.

4.3.3. Images of droplets contour change during ARCA measurements

To emphasize the contact angle measurements shown in Figure 80 images of the droplets at the beginning, during and at the end of the measurements are shown in Figure 81.

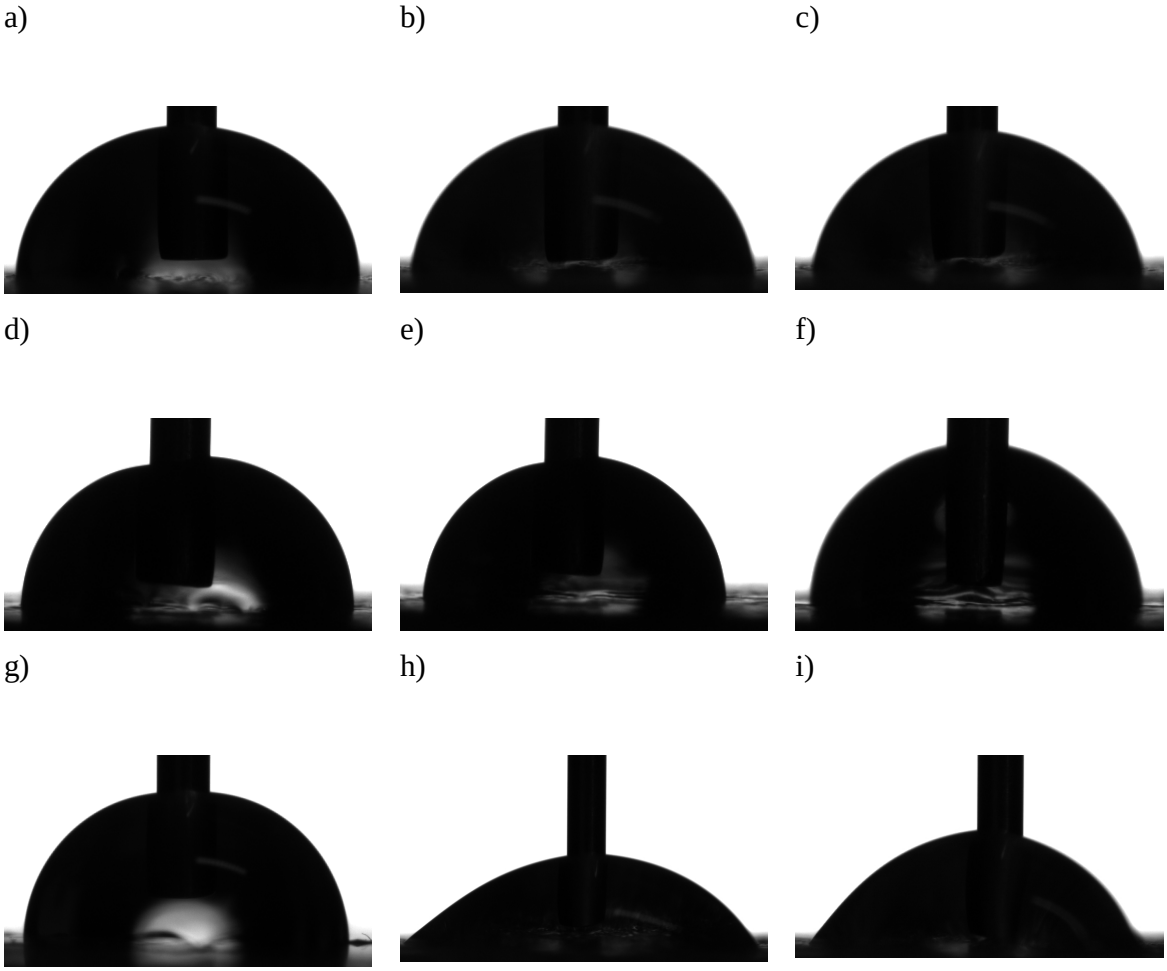

Figure 81: images of the dynamic contact angle measurements a)-c) PU coating without PU capsules at the beginning, during and at the end of the dynamic measurement, d)-f) PU coating with MTES filled PU capsules at the beginning, during and at the end of the dynamic measurement, g)-i) epoxy coating with TMODS and TMOS filled PU capsules at the beginning, during and at the end of the dynamic measurement

The effect of the single side water repellence can be seen clearly in Figure 81i). On the left side of the water droplet the water spread caused by the stretch deformation and a non-hydrophobic surface. The contact angle on the right side of the droplet was much higher showing a de-wetting caused by the hydrophobization of the surface by the silanes.

4.3.4. Conclusions

Concluding the results of the combination of dynamic contact angle measurement with a stretching device it could be shown that the method is very suitable for the detection of the self-healing and self-sealing properties of organic coatings containing inhibitor filled capsules. The investigations on these samples present a promising strategy to build self-healing coatings which will increase the corrosion protecting properties of coated materials as long as there are still unbroken capsules present in the coating.

The effect of the hydrophobization and self-healing of the different capsules is summarized in Figure 82.

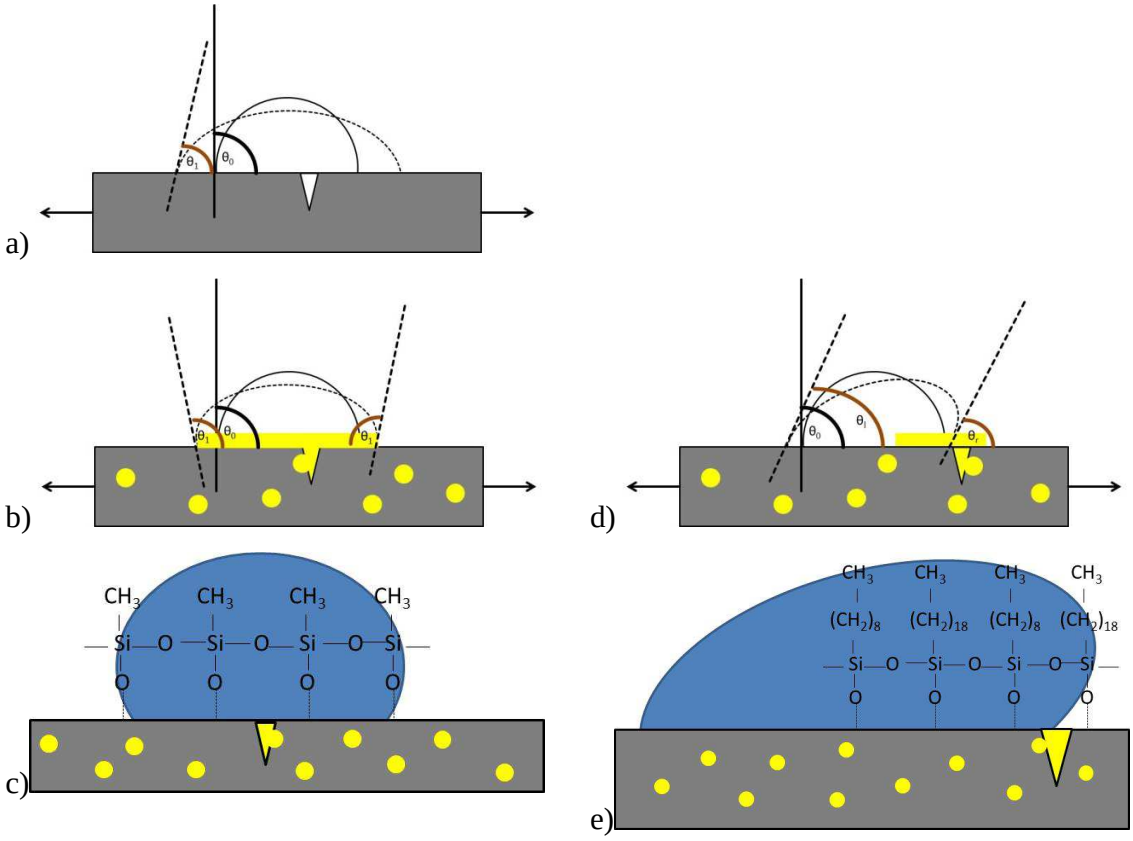

Figure 82: model illustration of the hydrophobization and the self-healing effect of the different corrosion inhibitors a) without inhibitor, b) & c) with MTES and d) & e) with TMOS and TMODS

For the coating without capsules the left and right contact angles decreased as a function of the stretch deformation. In presence of MTES filled capsules, the MTES dissolved in the water droplet, built a hydrophobic monolayer on the wetted surface and cross-linked. Filling

the capsules with a mixture of TMOS and TMODS led to an immediate hydrophobization of the surface at the cracked area followed by the cross-linking of the different alkoxysilanes.

Further studies on the capsules containing coatings should enhance the long time corrosion protection and have to focus on ensuring that the distribution of the capsules is sufficient so that adequate protection is provided, wherever a defect may form on the coating surface.

Investigations according to the test set-up should aim at further combinations of the dynamic contact angle measurement with electrochemical investigations. Within this combination the possibility would be given to analyze the change of the surface energy while detecting the change of the barrier properties (by means of EIS measurements), corrosion current density (by means of LSV and CV) or the change of the corrosion potential (by means of OCP measurement and CV). Finally the combination of all techniques, the contact angle measurement and electrochemical investigations with a stretching device could make it possible to predict application-oriented corrosion and corrosion protection processes of coatings used for industrial purposes.

5. Overall conclusions and outlook

Different light weight construction materials used in automotive industry, consumer goods, renewable energy industry and others were investigated for their environment dependent corrosion behavior and the possibilities of corrosion protection and self-healing. New methods were set up and successfully applied to get new insights, which go far beyond the conventionally used techniques in industry.

By use of directed ultrasonic treatment in an aqueous cerium nitrate solution it was possible to create a protective cerium oxide layer on the magnesium alloy AZ31. Although the layer was traversed by cracks with micrometers in diameter, neutral salt spray test (not shown here) showed very positive results. Electrochemical investigations by means of current density – potential measurements showed a promising decrease in the corrosion current density, even though the electrochemical impedance measurements indicated low impedance values, comparable to those of a pure magnesium oxide layer, which could be explained with the presence of cracks. The most powerful advantage up to now was the significant increase in the adhesion forces to an organic coating. An interaction of both, mechanical interlocking and the built-up of covalent bonds would explain this significant increase.

Avoiding the crack formation and making this technique economically more feasible must be a point of further investigations. Therefore, the understanding of the mechanisms leading to crack formation is of crucial importance.

In the investigations of different alloy coatings for the hot-forming of 22MnB5 steel it could be demonstrated that the combination of coulometric dissolution with downstream analysis of the dissolved elements by means of ICP-OES is a very useful tool for the exploration of corrosion stability and the cathodic corrosion protection ability of such alloy coatings.

The not hot-formed pure zinc coating Z140 showed as “good-reference” a longtime corrosion protective effect. As described by Karbasian and Tekkaya [54] this coating was not resistant against welding, as it evaporated under the high thermal stress.

Hot-forming of the pure zinc coating Z140 led to an alloying of iron from the substrate into the coating. Consequently the protective effect was only short time with selective, initial zinc dissolution. Caused by the alloying of iron into the zinc coating the evaporation of the coating during welding was reduced.

A similar behavior to the hot-formed pure zinc coating was observed with the iron containing zinc alloy coating Zn/Fe. In the beginning of the coulometric ICP-OES measurements, selective zinc dissolution could be observed leading to a short time cathodic corrosion protection. The evaporation of the alloy coating during welding was reduced as in the case of Z140 coatings.

Alloying of nickel to the zinc alloy coating Zn/Ni showed a cathodic corrosion protection ability only for a very short time when the initial, preferential zinc dissolution took place. This dissolution was followed by a very fast enrichment of nickel in the alloy coating, resulting in a passivation of the surface and hence an inhibited dissolution possibility of the zinc. Therefore a cathodic corrosion protection ability coating was not provided with this alloy. According to Karbasian and Tekkaya [54] no evaporation of the alloy coating took place during welding.

By phosphating the alloy coatings, the free corrosion potential, measured in the current density – potential curves, was shifted to values equal to or even more anodic than the Fe/Fe^{2+} potential. This indicates that the phosphating led to an inhibition of the cathodic corrosion protection until the passivating phosphate layer broke down.

With increasing process conditions, meaning increasing heat treatment, the cathodic corrosion protection ability of the pure zinc coating Z140 and the iron containing zinc alloy coating Zn/Fe was inhibited. As a consequence an anodic potential shift in the current density – potential curves and earlier dissolution of the steel substrate in the coulometric ICP-OES measurements took place. Furthermore the potential values during the coulometric ICP-OES measurements indicated that Fe was partially oxidized to Fe^{3+}. The nickel containing zinc alloy coating Zn/Ni showed a potential more anodic than the Fe/Fe^{2+} potential even after process condition I. Neither the corrosion potential nor the corrosion current density did change with increasing process conditions, indicating that the nickel was enriched at the surface, which led to a passive layer inhibiting the zinc dissolution. This enrichment of nickel at the surface could be validated by EDX measurements where amounts of zinc oxide and iron oxide increased after process

condition III when, caused by the heat induced diffusion of iron into the zinc alloy coating, the passive nickel layer was partially malfunctioning.

For the investigations of self-healing and self-sealing coatings a new test set-up was developed. The combination of dynamic contact angle measurement with stretch deformation to induce micro cracks in the examined coating led to a very suitable technique for the observation of the mentioned effects. It could be shown that alkoxysilanes, as water replacing inhibitors, filled capsules embedded in an organic coating broke up due to the crack formation in the surrounding organic coating induced by stretch deformation. The leaking compounds built up a hydrophobic protection layer and due to hydrolysis and polycondensation a polysiloxane film was built, closing the defects. By use of dynamic contact angle measurements and differencing the right and left contact angles it could be shown that the hydrophobization took only place where crack formation occurred.

New combinations of a stretching device for micro-crack formation, contact angle measurements for the evaluation of the surface tension and electrochemical investigations for the detection of corrosion protection and barrier properties of protective coatings could lead to a fundamental understanding of self-healing and self-sealing mechanisms for the development of forward-looking long-time corrosion protection technologies.

References

1 Friedrich, H.E. (2013) *Leichtbau in der Fahrzeugtechnik*, Imprint: Springer Vieweg, Wiesbaden.

2 Hodkinson, R. and Fenton, J. (2001) *Lightweight electric/hybrid vehicle design*, Butterworth-Heinemann, Oxford, Woburn, MA.

3 Friedrich, H.E. and Mordike, B.L. (2006) *Magnesium technology: Metallurgy, design data, applications*, Springer, Berlin, New York.

4 Holleman, A.F., und Nils Wiberg, E., Fischer, G. (2007) *Lehrbuch der Anorganischen Chemie*, Walter de Gruyter, Berlin • New York.

5 Mordike, B. and Ebert, T. (2001) Magnesium. *Materials Science and Engineering: A*, **302** (1), 37–45.

6 Eliezer, D., Aghion, E., Froes, F.H. (1998) Magnesium Science, Technology and Applications. *Advanced Performance Materials*, **5** (3), 201–212.

7 Alvarez-Lopez, M., Pereda, M.D., del Valle, J A, Fernandez-Lorenzo, M., Garcia-Alonso, M.C., Ruano, O.A., Escudero, M.L. (2010) Corrosion behaviour of AZ31 magnesium alloy with different grain sizes in simulated biological fluids. *Acta biomaterialia*, **6** (5), 1763–1771.

8 Song, G. (2005) Recent Progress in Corrosion and Protection of Magnesium Alloys. *Adv. Eng. Mater.*, **7** (7), 563–586.

9 Song, G. and Atrens, A. (1999) Corrosion Mechanisms of Magnesium Alloys. *Adv. Eng. Mater.*, **1** (1), 11–33.

10 Grundmeier, G., Schmidt, W., Stratmann, M. (2000) Corrosion protection by organic coatings: electrochemical mechanism and novel methods of investigation. *Electrochimica Acta*, **45** (15-16), 2515–2533.

11 Hu, R.-G., Zhang, S., Bu, J.-F., Lin, C.-J., Song, G.-L. (2012) Recent progress in corrosion protection of magnesium alloys by organic coatings. *Progress in Organic Coatings*, **73** (2-3), 129–141.

12 Fukumoto, S., Sugahara, K., Yamamoto, A., Tsubakino, H. (2003) Improvement of Corrosion Resistance and Adhesion of Coating Layer for Magnesium Alloy Coated with High Purity Magnesium. *Materials Trancsactions*, **44** (4), 518–523.

13 Hornberger, H., Virtanen, S., Boccaccini, A.R. (2012) Biomedical coatings on magnesium alloys - a review. *Acta biomaterialia*, **8** (7), 2442–2455.

14 Jin, J., Liu, C., Fu, S., Gao, Y., Shu, X. (2011) Electroless Ni-P plating on Mg-10Gd-4.8Y-0.6Zr magnesium alloy with a new pretreatment process. *Surface and Coatings Technology*, **206** (2-3), 348–353.

15 Sankara Narayanan, T. (2005) Surface pretreatment by phosphate conversion coatings - a review. *Rev.Adv.Mater.Sci.*, **9** (2), 130–177.

16 Aung, N.N. and Zhou, W. (2010) Effect of grain size and twins on corrosion behaviour of AZ31B magnesium alloy. *Corrosion Science*, **52** (2), 589–594.

17 Gray, J.E. and Luan, B. (2002) Protective coatings on magnesium and its alloys — a critical review. *Journal of Alloys and Compounds*, **336** (1-2), 88–113.

18 Arnott, D.R., Ryan, N.E., Hinton, B., Sexton, B.A., Hughes, A.E. (1985) Auger and XPS studies of cerium corrosion inhibition on 7075 aluminum alloy. *Applications of Surface Science*, **22-23**, 236–251.

19 Rudd, A.L., Breslin, C.B., Mansfeld, F. (2000) The corrosion protection afforded by rare earth conversion coatings applied to magnesium. *Corrosion Science*, **42** (2), 275–288.

20 Azimi, G., Dhiman, R., Kwon, H.-M., Paxson, A.T., Varanasi, K.K. (2013) Hydrophobicity of rare-earth oxide ceramics. *Nature materials*, **12** (4), 315–320.

21 Li, Y., Tan, C., Qi, G., Guo, J., Wang, X., Zhang, S. (2013) Decanoate conversion layer with improved corrosion protection for magnesium alloy. *Corrosion Science*, **70**, 229–234.

22 Blawert, C., Dietzel, W., Ghali, E., Song, G. (2006) Anodizing Treatments for Magnesium Alloys and Their Effect on Corrosion Resistance in Various Environments. *Adv. Eng. Mater.*, **8** (6), 511–533.

23 Ryu, H.S., Park, D.-S., Hong, S.-H. (2013) Improved corrosion protection of AZ31 magnesium alloy through plasma electrolytic oxidation and aerosol deposition duplex treatment. *Surface and Coatings Technology*, **219**, 82–87.

24 Choi, Y.-I., Salman, S., Kuroda, K., Okido, M. (2013) Synergistic corrosion protection for AZ31 Mg alloy by anodizing and stannate post-sealing treatments. *Electrochimica Acta*, **97**, 313–319.

25 Mahallawy, N. A. El, Shoeib, M.A., Abouelenain, M.H. (2011) AZ91 Magnesium Alloys: Anodizing of Using Environmental Friendly Electrolytes. *JSEMAT*, **01** (02), 62–72.

26 Xia, L., Akiyama, E., Frankel, G., McCreery, R. (2000) Storage and Release of Soluble Hexavalent Chromium from Chromate Conversion Coatings Equilibrium Aspects of Cr[sup VI] Concentration. *J. Electrochem. Soc.*, **147** (7), 2556.

27 Suda, A. and Shinohara, T. (2002) Effects of Colloidal Silica Addition on the Self-healing Function of Chromate Coatings. *ISIJ International*, **42** (5), 540–544.

28 Kendig, M.W. and Buchheit, R.G. (2003) Corrosion Inhibition of Aluminum and Aluminum Alloys by Soluble Chromates, Chromate Coatings, and Chromate-Free Coatings. *Corrosion*, **59** (5), 379–400.

29 Pretty, J.R., Blubaugh, E.A., Caruso, J.A., Davidson, T.M. (1994) Determination of Chromium(VI) and Vanadium(V) Using an Online Anodic Stripping Voltammetry Flow Cell with Detection by Inductively Coupled Plasma Mass Spectrometry. *Anal. Chem.*, **66** (9), 1540–1547.

30 Mancuso T. F. (1997) Chromium as an industrial carcinogen: Part I. *American Journal of Industrial Medicine* (31), 129–139.

31 Mancuso T. F. (1997) Chromium as an industrial carcinogen: Part II. Chromium in human tissues. *American Journal of Industrial Medicine* (31), 140–147.

32 Browning, E. (1969) *Toxicity of industrial metals*, 2nd edn, Butterworths, London.

33 Ghosh, S.K. (2009) *Self-healing materials: Fundamentals, design strategies, and applications*, Wiley-VCH; [John Wiley, distributor], Weinheim, [Chichester].

34 van der Zwaag, S, van Dijk, N H, Jonkers, H.M., Mookhoek, S.D., Sloof, W.G. (2009) Self-healing behaviour in man-made engineering materials: bioinspired but taking into account their intrinsic character. *Philosophical transactions. Series A, Mathematical, physical, and engineering sciences*, **367** (1894), 1689–1704.

35 Hager, M.D., Greil, P., Leyens, C., van der Zwaag, Sybrand, Schubert, U.S. (2010) Self-healing materials. *Advanced materials (Deerfield Beach, Fla.)*, **22** (47), 5424–5430.

36 Shinya, N., Kyono, J., Laha, K. (2006) Self-healing Effect of Boron Nitride Precipitation on Creep Cavitation in Austenitic Stainless Steel. *Journal of Intelligent Material Systems and Structures*, **17** (12), 1127–1133.

37 Laha, K., Kyono, J., Shinya, N. (2007) An advanced creep cavitation resistance Cu-containing 18Cr–12Ni–Nb austenitic stainless steel. *Scripta Materialia*, **56** (10), 915–918.

38 Song, G.M., Pei, Y.T., Sloof, W.G., Li, S.B., Hosson, J. de, van der Zwaag, S. (2008) Oxidation-induced crack healing in Ti3AlC2 ceramics. *Scripta Materialia*, **58** (1), 13–16.

39 Zwaag, S. van der, Schmets, Alexander J. M, Zaken, Geeta van der (2007) *Self healing materials: An alternative approach to 20 centuries of materials science*, Springer, Dordrecht, the Netherlands.

40 Skorb, E., Shchukin, D., Möhwald, H., Andreeva, D. (2010) Sonochemical design of cerium-rich anticorrosion nanonetwork on metal surface. *Langmuir : the ACS journal of surfaces and colloids*, **26** (22), 16973–16979.

41 Skorb, E.V., Shchukin, D.G., Möhwald, H., Andreeva, D.V. (2010) Ultrasound-driven design of metal surface nanofoams. *Nanoscale*, **2** (5), 722–727.

42 Skorb, E.V., Fix, D., Shchukin, D.G., Möhwald, H., Sviridov, D.V., Mousa, R., Wanderka, N., Schäferhans, J., Pazos-Pérez, N., Fery, A., Andreeva, D.V. (2011) Sonochemical formation of metal sponges. *Nanoscale*, **3** (3), 985–993.

43 Belova, V., Gorin, D.A., Shchukin, D.G., Möhwald, H. (2011) Controlled effect of ultrasonic cavitation on hydrophobic/hydrophilic surfaces. *ACS applied materials & interfaces*, **3** (2), 417–425.

44 Gensel, J., Borke, T., Pérez, N.P., Fery, A., Andreeva, D.V., Betthausen, E., Müller, Axel H E, Möhwald, H., Skorb, E.V. (2012) Cavitation engineered 3D sponge networks and their application in active surface construction. *Advanced materials (Deerfield Beach, Fla.)*, **24** (7), 985–989.

45 Skorb, E.V., Baidukova, O., Goyal, A., Brotchie, A., Andreeva, D.V., Möhwald, H. (2012) Sononanoengineered magnesium–polypyrrole hybrid capsules with synergetic trigger release. *J. Mater. Chem.*, **22** (27), 13841.

46 Andreeva, D.V., Sviridov, D.V., Masic, A., Möhwald, H., Skorb, E.V. (2012) Nanoengineered metal surface capsules: construction of a metal-protection system. *Small (Weinheim an der Bergstrasse, Germany)*, **8** (6), 820-5, 819.

47 Shchukin, D.G., Skorb, E., Belova, V., Möhwald, H. (2011) Ultrasonic cavitation at solid surfaces. *Advanced materials (Deerfield Beach, Fla.)*, **23** (17), 1922–1934.

48 Kaş, R., Ertaş, F.S., Birer, Ö. (2012) Ultrasound assisted deposition of silica coatings on titanium. *Applied Surface Science*, **259**, 501–507.

49 Geiger, M., Merklein, M., Hoff, C. (2005) Basic Investigations on the Hot Stamping Steel 22MnB5. *AMR*, **6-8**, 795–804.

50 Merklein, M. and Lechler, J. (2006) Investigation of the thermo-mechanical properties of hot stamping steels. *Journal of Materials Processing Technology*, **177** (1-3), 452–455.

51 Merklein, M., Lechler, J., Geiger, M. (2006) Characterisation of the Flow Properties of the Quenchenable Ultra High Strength Steel 22MnB5. *CIRP Annals - Manufacturing Technology*, **55** (1), 229–232.

52 Turetta, A., Bruschi, S., Ghiotti, A. (2006) Investigation of 22MnB5 formability in hot stamping operations. *Journal of Materials Processing Technology*, **177** (1-3), 396–400.

53 Lee, M.-G., Kim, S.-J., Han, H.N., Jeong, W.C. (2009) Application of hot press forming process to manufacture an automotive part and its finite element analysis considering phase transformation plasticity. *International Journal of Mechanical Sciences*, **51** (11-12), 888–898.

54 Karbasian, H. and Tekkaya, A.E. (2010) A review on hot stamping. *Journal of Materials Processing Technology*, **210** (15), 2103–2118.

55 Lee, C.W., Fan, D.W., Sohn, I.R., Lee, S.-J., De Cooman, Bruno C. (2012) Liquid-Metal-Induced Embrittlement of Zn-Coated Hot Stamping Steel. *Metall and Mat Trans A*, **43** (13), 5122–5127.

56 Kondratiuk, J., Kuhn, P., Labrenz, E., Bischoff, C. (2011) Zinc coatings for hot sheet metal forming: Comparison of phase evolution and microstructure during heat treatment. *Surface and Coatings Technology*, **205** (17-18), 4141–4153.

57 Mendala, J. (2012) Liquid metal embrittlement of steel with galvanized coatings. *IOP Conf. Ser.: Mater. Sci. Eng.*, **35**, 012002.

58 Zheludkevich, M.L., Poznyak, S.K., Rodrigues, L.M., Raps, D., Hack, T., Dick, L.F., Nunes, T., Ferreira, M. (2010) Active protection coatings with layered double hydroxide nanocontainers of corrosion inhibitor. *Corrosion Science*, **52** (2), 602–611.

59 Yuan, Y.C. (2008) Self healing in polymers and polymer composites. Concepts, realization and outlook: A review. *expresspolymlett*, **2** (4), 238–250.

60 Wool, R.P. (1981) A theory of crack healing in polymers. *J. Appl. Phys.*, **52** (10), 5953.

61 Wool, R.P., Yuan, B.-L., McGarel, O.J. (1989) Welding of polymer interfaces. *Polymer Engineering and Science*, **29** (19), 1340–1367.

62 Kim, Y.H. and Wool, R.P. (1983) A Theory of Healing at a Polymer-Polymer Interface. *Macromolecules*, **16** (7), 1115–1120.

63 Jud, K. and Kausch, H.H. (1979) Load transfer through chain molecules after interpenetration at interfaces. *Polymer Bulletin*, **1** (10), 697–707.

64 Jud, K., Kausch, H.H., Williams, J.G. (1981) Fracture mechanics studies of crack healing and welding of polymers. *Journal of Materials Science & Technology*, **16**, 204–210.

65 Lin, C.B., Lee, S., Liu, K.S. (1990) Methanol-Induced crack healing in poly(methyl methacrylate). *Polymer Engineering and Science*, **30** (21), 1399–1406.

66 Wang, P.-P., Lee, S., Harmon, J.P. (1994) Ethanol-induced crack healing in poly(methyl methacrylate). *Journal of polymer science. Part B, Polymer physics*, **32** (7), 1217–1227.

67 Kalista, S.J. and Ward, T.C. (2007) Thermal characteristics of the self-healing response in poly(ethylene-co-methacrylic acid) copolymers. *Journal of the Royal Society, Interface / the Royal Society*, **4** (13), 405–411.

68 Takeda, K., Unno, H., Zhang, M. (2004) Polymer reaction in polycarbonate with Na2CO3. *J. Appl. Polym. Sci.*, **93** (2), 920–926.

69 Imaizumi, K., Ohba, T., Ikeda, Y., Takeda, K. (2001) Self-repairing mechanism of polymer composite. *Materials Science Research International*, **7** (4), 249–253.

70 Chen, X., Dam, M.A., Ono, K., Mal, A., Shen, H., Nutt, S.R., Sheran, K., Wudl, F. (2002) A thermally re-mendable cross-linked polymeric material. *Science*, **295** (5560), 1698–1702.

71 Liu, Y.-L. and Hsieh, C.-Y. (2006) Crosslinked epoxy materials exhibiting thermal remendablility and removability from multifunctional maleimide and furan compounds. *J. Polym. Sci. A Polym. Chem.*, **44** (2), 905–913.

72 Liu, Y.-L. and Chen, Y.-W. (2007) Thermally Reversible Cross-Linked Polyamides with High Toughness and Self-Repairing Ability from Maleimide- and Furan-Functionalized Aromatic Polyamides. *Macromol. Chem. Phys.*, **208** (2), 224–232.

73 Nesterova, T., Dam-Johansen, K., Kiil, S. (2011) Synthesis of durable microcapsules for self-healing anticorrosive coatings: A comparison of selected methods. *Progress in Organic Coatings*, **70** (4), 342–352.

74 Reichle, W. (1986) Synthesis of anionic clay minerals (mixed metal hydroxides, hydrotalcite). *Solid State Ionics*, **22** (1), 135–141.

75 Patricio Cardoso, L. and Valim, J.B. (2004) Competition between three organic anions during regeneration process of calcined LDH. *Journal of Physics and Chemistry of Solids*, **65** (2-3), 481–485.

76 Wranglén, G. (1985) *Korrosion und Korrosionsschutz: Grundlagen, Vorgänge, Schutzmassnahmen, Prüfung*, Springer, Berlin [etc.].

77 Zhang, J., Zhang, Q., Ren, H., Zhao, W., Zhang, H. (2007) Inhibition performance of 2-mercaptobenzothiazole derivatives in CO2 saturated solution and its adsorption behavior at Fe surface. *Applied Surface Science*, **253** (18), 7416–7422.

78 Huang, M. and Yang, J. (2011) Facile microencapsulation of HDI for self-healing anticorrosion coatings. *J. Mater. Chem.*, **21** (30), 11123.

79 García, S.J., Fischer, H.R., White, P.A., Mardel, J., González-García, Y., Mol, J., Hughes, A.E. (2011) Self-healing anticorrosive organic coating based on an encapsulated water reactive silyl ester: Synthesis and proof of concept. *Progress in Organic Coatings*, **70** (2-3), 142–149.

80 Brown, E.N., Kessler, M.R., Sottos, N.R., White, S.R. (2003) In situ poly(urea-formaldehyde) microencapsulation of dicyclopentadiene. *Journal of microencapsulation*, **20** (6), 719–730.

81 Latnikova, A., Grigoriev, D.O., Hartmann, J., Möhwald, H., Shchukin, D.G. (2011) Polyfunctional active coatings with damage-triggered water-repelling effect. *Soft Matter*, **7** (2), 369–372.

82 van Ooij, W. J., Zhu, D., Stacy, M., Seth, A., Mugada, T., Gandhi, J., Puomi, P. (2005) Corrosion Protection Properties of Organofunctional Silanes—An Overview. *Tsinghua Science & Technology*, **10** (6), 639–664.

83 Posner, R., Santa, M., Grundmeier, G. (2011) Wet- and Corrosive De-Adhesion Processes of Water-Borne Epoxy Film Coated Steel. *J. Electrochem. Soc.*, **158** (3), C29.

84 Santa, M., Posner, R., Grundmeier, G. (2011) Wet- and Corrosive De-Adhesion Processes of Water-Borne Epoxy Film Coated Steel. *J. Electrochem. Soc.*, **158** (3), C36.

85 Grundmeier, G. and Stratmann, M. (2005) ADHESION AND DE-ADHESION MECHANISMS AT POLYMER/METAL INTERFACES: Mechanistic Understanding Based on In Situ Studies of Buried Interfaces. *Annu. Rev. Mater. Res.*, **35** (1), 571–615.

86 Wapner, K. and Grundmeier, G. (2004) Scanning Kelvin Probe Measurements of the Stability of Adhesive/Metal Interfaces in Corrosive Environments. *Adv. Eng. Mater.*, **6** (3), 163–167.

87 White, S.R., Sottos, N.R., Geubelle, P.H., Moore, J.S., Kessler, M.R., Sriram, S.R., Brown, E.N., Viswanathan, S. (2001) Autonomic healing of polymer composites. *Nature*, **409** (15), 794–817.

88 Rule, J.D., Sottos, N.R., White, S.R. (2007) Effect of microcapsule size on the performance of self-healing polymers. *Polymer*, **48** (12), 3520–3529.

89 Blaiszik, B.J., Sottos, N.R., White, S.R. (2008) Nanocapsules for self-healing materials. *Composites science and technology*, **68** (3-4), 978–986.

90 Dry, C. (1994) Matrix cracking repair and filling using active and passive modes for smart timed release of chemicals from fibers into cement matrices. *Smart Materials and Structures*, **3** (2), 118–123.

91 Bleay, S., Loader, C., Hawyes, V., Humberstone, L., Curtis, P. (2001) A smart repair system for polymer matrix composites. *Composites Part A: Applied Science and Manufacturing*, **32** (12), 1767–1776.

92 Toohey, K.S., Sottos, N.R., Lewis, J.A., Moore, J.S., White, S.R. (2007) Self-healing materials with microvascular networks. *Nature materials*, **6** (8), 581–585.

93 Therriault, D., Shepherd, R.F., White, S.R., Lewis, J.A. (2005) Fugitive Inks for Direct-Write Assembly of Three-Dimensional Microvascular Networks. *Adv. Mater.*, **17** (4), 395–399.

94 Bejan, A., Lorente, S., Wang, K.-M. (2006) Networks of channels for self-healing composite materials. *J. Appl. Phys.*, **100** (3), 033528.

95 Hawkes, P.W. and Spence, John C. H (2008) *Science of microscopy*, Springer, New York, NY.

96 Yao, N. and Wang, Z.L. (2005) *Handbook of microscopy for nanotechnology*, Kluwer Academic Publishers, Boston.

97 Egerton, R.F. (ed) (2005) *Physical Principles of Electron Microscopy*, Springer US, Boston, MA.

98 Echlin, P. (2009) *Handbook of sample preparation for scanning electron microscopy and x-ray microanalysis*, Springer, New York, London.

99 Menzies, A.C. (1953) Raman effect in solids. *Rep. Prog. Phys.*, **16** (1), 83–107.

100 Baia, M., Astilean, S., Iliescu, T. (eds) (2008) *Raman and SERS Investigations of Pharmaceuticals*, Springer Berlin Heidelberg, Berlin, Heidelberg.

101 Kellner, R.A., Widmer, H.M., Mermet, J.-M., Otto, M., Valcarcel Cases, M. (2004 [1461]) *Analytical chemistry: A modern approach to analytical science*, 2nd edn, Wiley-VCH, Weinheim, Germany.

102 Hamann, C.H. and Vielstich, W. (2005) *Elektrochemie*, 4th edn, Wiley-VCH, Weinheim.

103 Lefrou, C., Fabry, P., Poignet, J.-C. (2012) *Electrochemistry: The basics, with examples*, Springer, Berlin, New York.

104 Yuan, X.-Z. (2010) *Electrochemical impedance spectroscopy in PEM fuel cells: Fundamentals and applications*, Springer, London.

105 McCafferty, E. (2010) *Introduction to corrosion science*, Springer, New York.

106 Wang, X., Somsen, C., Grundmeier, G. (2008) Ageing of thin Ag/fluorocarbon plasma polymer nanocomposite films exposed to water-based electrolytes. *Acta Materialia*, **56** (4), 762–773.

107 Olesik, J.W. (1991) Elemental Analysis Using ICP-OES and ICP/MS. *Anal. Chem.*, **63** (1), 12A.

108 Sapkota, A., Krachler, M., Scholz, C., Cheburkin, A.K., Shotyk, W. (2005) Analytical procedures for the determination of selected major (Al, Ca, Fe, K, Mg, Na, and Ti) and trace (Li, Mn, Sr, and Zn) elements in peat and plant samples using inductively coupled plasma-optical emission spectrometry. *Analytica Chimica Acta*, **540** (2), 247–256.

109 Butt, H.-J., Graf, K., Kappl, M. (2003) *Physics and chemistry of interfaces*, Wiley-VCH, Weinheim.

110 Kinloch, A.J., Lau, C.C., Williams, J.G. (1994) The peeling of flexible laminates. *International Journal of Fracture*, **66** (1), 45–70.

111 Williams, J.A. and Kauzlarich, J.J. (2005) The influence of peel angle on the mechanics of peeling flexible adherends with arbitrary load–extension characteristics. *Tribology International*, **38** (11-12), 951–958.

112 Meka, P. and Stehling, F.C. (1994) Heat sealing of semicrystalline polymer films. I. Calculation and measurement of interfacial temperatures: Effect of process variables on seal properties. *Journal of Applied Polymer Science*, **51** (1), 89–103.

113 Qu, L., Li, M., Liu, M., Zhang, E., Ma, C. (2013) Microstructure and corrosion resistance of ultrasonic micro-arc oxidation biocoatings on magnesium alloy. *J Adv Ceram*, **2** (3), 227–234.

114 Godinho, M.J., Gonçalves, R.F., S Santos, L.P., Varela, J.A., Longo, E., Leite, E.R. (2007) Room temperature co-precipitation of nanocrystalline CeO2 and Ce0.8Gd0.2O1.9−δ powder. *Materials Letters*, **61** (8-9), 1904–1907.

115 Kim, J.H. and Hwang, I.S. (2005) Development of an in situ Raman spectroscopic system for surface oxide films on metals and alloys in high temperature water. *Nuclear Engineering and Design*, **235** (9), 1029–1040.

116 Yang, Y., Yang, Y., Fu, T., Zhu, J., Fan, J., Zhang, Z., Zhang, J. (2014) Influence of ethanol content in the precursor solution on anodic electrodeposited CeO2 thin films. *Thin Solid Films*, **556**, 128–136.

117 Nelson, D.L. and Irish, D.E. (1973) Interactions in lanthanide systems. Part 2.—Raman study of aqueous cerium(III) nitrate. *J. Chem. Soc., Faraday Trans. 1*, **69** (0), 156.

118 Thissen, P., Thissen, V., Wippermann, S., Chabal, Y.J., Grundmeier, G., Schmidt, W.G. (2012) pH-dependent structure and energetics of H2O/MgO(100). *Surface Science*, **606** (11-12), 902–907.

Abbreviations

$(Mg,Fe)_2[SiO_4]$	olivine
µm	micrometer
8-HQ	*8*-hydroxyquinoline
a	activity
A	surface area
AC	alternating current
Ag	silver
AgCl	silver chloride
A_H	Hamaker constant
AiF	Arbeitsgemeinschaft industrieller Forschungsvereinigungen
Al	aluminum
$Al(OH)_3$	aluminum hydroxide
Ar	argon
ARCA	advancing and receding contact angle
ATR-FTIR	attenuated total reflection - fourier transformed infrared spectroscopy
BIW	body in white
BN	boron nitride
BO_3	borate
BSE	backscattered electrons
c	speed of light
C	carbon, capacitance
C_{AB}	dipole-dipole interaction
$CaMg(CO_3)_2$	dolomite
CCD	charged-coupled devices
Ce	cerium
$Ce(NO)_3$	cerium nitrate
$CeCl_3$	cerium chloride
Cl	chlorine
CL	cathodoluminescence
cm^3	cubic centimeter
CO_2	carbon dioxide
Cr	chromium
Cr(OH)	chromium hydroxide
Cs	cesium
CTD	charge-transfer device
$CuBr_2(2\text{-MeIm})_4$	2-methylimidazole/CuBr2 complex
d	distance
DCPD	dicyclopentadiene
DIN	German standards institute
DOW-17	anodization process by DOW Chemicals
E	potential
EDX	energy dispersive x-ray spectroscopy
E_h	half-cell potential
E_i^0	standard potential
EIS	electrochemical impedance spectroscopy
EMAA	poly(ethylene-co-methacrylic acid)
EU	european union
eV	electron volt
F	Faraday constant
Fe	iron
FE-SEM	field emission - scanning electron microscopy
FTP75	EPA Federal Test Procedure - city driving cycle
g	gram
Ga	gallium
h	Planck constant
H	hydrogen
H_2F_2	hydrofluoric acid
H_2O	water
H_2O_2	hydrogen peroxide
H_3BO_3	boric acid
H_3PO_4	phosphoric acid
HAE	anodizing process by Pitman-Dunn Laboratories
HCl	hydrochloric acid
HDG	hot-dip galvanized
HDI	hexamethylene diisocyanate
hf	high-frequency
HF	hydrofloric acid
HNO_3	nitric acid
Hz	Hertz
I	current
ICP-OES	inductively coupled plasma - optical emission spectroscopy
IGF	industrielle Gemeinschaftsforschung
JP10-15	japanese driving cycle
K	potassium, Kelvin
K_2MnO_4	potassium manganate
k_B	Boltzmann constant
KF	potassium fluoride

Abbreviations

km	kilometer
$KMgCl_3 * 6H_2O$	carnallite
$KMnO_4$	potassium permanganate
KOH	potassium hydroxide
L	liter
$La(NO)_3$	lanthanum nitrate
LDH	layered double hydroxides
LMIE	liquid metal induced embrittlement
m^2	square meter
MAGOXID-COAT	plasma-chemical anodizing process for magnesium
MBT	*2*-mercaptobenzothiazole
MDI	methylene diphenyl diisocyanate
MEA	methyl ethylacrylate
Mg	magnesium
$Mg_3(OH)_4[Si_2O_5]$	serpentine
$Mg_3(OH_2)[Si_4O_{10}]$	talc
$MgCl_2 * 6H_2O$	bischofite
$MgCO_3$	magnesite
$MgSO_4 * H_2O$	kieserite
min	minute
mL	milliliter
MMA	methyl methacrylate
MNEFZ	modified new european driving cycle
MPa	megapascal
MTODS	trimethoxy(octadecyl)silane
MTOS	trimethoxy(octyl)silane
Na	sodium
$Na_2B_4O_7$	sodium tetraborate
Na_2CO_3	sodium carbonate, sodium carbonate
$Na_2Cr_2O_7$	sodium dichromate
Na_2SiO_2	sodium silicate
Na_2SnO_3	sodium stannate
Na_3PO_4	sodium phosphate
$NaAlO_2$	sodium aluminate
NaCl	sodium chloride
NaOH	sodium hydroxide
ng	nanogram
NH_4HF_2	ammonium fluoride
NHE	normal hydrogen electrode
Ni	nickel
nm	nanometer
NO_3	nitrate
O	oxygen
OCP	open circuit potential
P	phosphorus
p.a.	pro analysi
PC	polycarbonate
PMMA	poly(methyl methacrylate)
PMT	photomultiplier tube
PPE	poly(phenylene ether)
$Pr(NO)_3$	praseodymium nitrate
PU	polyurethane
q	amount of charge
R	radius, resistor, universal gas constant
rms	root mean square
rpm	rounds per minute
s	second
S	sulfur
SCE	saturated calomel electrode
Se	selenium
SE	secondary electrons
SEM	scanning electron microscopy
SHE	standard hydrogen electrode
Si	silicon
SiO_2	silicon dioxide
SO_4	sulfate
STEM	scanning transmission electron microscope
SVET	Scanning Vibrating Electrode Technique
T	absolute temperature
TAGNITE	anodizing process by Technology Applications Group
US	ultrasonic
V	voltage, volt
W	watt
XPS	X-ray photon spectroscopy
XRD	X-ray diffraction
z	valence
Z	impedance
Zn	zinc
γ	surface tension
$\Delta\varphi$	potential difference
ε	dielectric constant
ε_0	dielectric constant in vacuum

θ	contact angle, phase shift	ν	frequency
θ_{adv}	advancing contact angle	ρ	density
θ_{rec}	receding contact angle	φ	potential
λ	wavelength	ϕ	phase shift
μ	electrochemical potential	ω	radial frequency

Table of figures and tables